NASA

Tech Briefs

National Aeronautics and Space Administration

Electronic Components and Circuits

Electronic Systems

Physical Sciences

Materials

Computer Programs

Mechanics

Machinery

Fabrication Technology

Mathematics and Information Sciences

Life Sciences

97-05

May 1997

INTRODUCTION

Tech Briefs are short announcements of new technology derived from the research and development activities of the National Aeronautics and Space Administration. These Briefs emphasize information considered likely to be transferable across industrial, regional, or disciplinary lines and are issued to encourage commercial application.

Availability of NASA Tech Briefs and TSP's

Distribution of NASA Tech Briefs, a monthly periodical publication, is limited to engineers in U.S. Industry and to other domestic technology transfer agents. Requests for individual Tech Briefs or for Technical Support Packages (TSP's) announced herein should be addressed to

NASA Center for AeroSpace Information
Technology Transfer Office
800 Elkridge Landing Rd.
Linthicum Heights, MD 21090-2934
Telephone No. (301) 621-0245

Please reference the three-letter, five-digit control number located at the end of each Tech Brief. Information on NASA's Technology Utilization Program, its documents, and services is also available at the same facility.

Technology Utilization Officers and Patent Counsels are located at NASA field installations to provide technology-transfer access to industrial users. Inquiries can be made by writing to NASA field installations listed below.

Technology Utilization Officers and Patent Counsels

Ames Research Center
Technology Utilization Officer
Mail Code 223-3
Moffett Field, CA 94035

Patent Counsel
Mail Code 200-11
Moffett Field, CA 94035

Goddard Space Flight Center
Technology Utilization Officer
Mail Code 702-1
Greenbelt, MD 20771

Patent Counsel
Mail Code 204
Greenbelt, MD 20771

Lyndon B. Johnson Space Center
Technology Utilization Officer
Mail Code IC-4
Houston, TX 77058

Patent Counsel
Mail Code AL3
Houston, TX 77058

John F. Kennedy Space Center
Technology Utilization Officer
Mail Stop PT-PMO-A
Kennedy Space Center, FL 32899

Patent Counsel
Mail Code PT-PAT
Kennedy Space Center, FL 32899

Langley Research Center
Technology Utilization Officer
Mail Stop 143
Hampton, VA 23665

Patent Counsel
Mail Code 279
Hampton, VA 23665

Lewis Research Center
Technology Utilization Officer
Mail Stop 7-3
21000 Brookpark Road
Cleveland, OH 44135

Patent Counsel
Mail Code LE-LAW
21000 Brookpark Road
Cleveland, OH 44135

Jet Propulsion Laboratory
Technology Utilization Officer
Mail Stop 156-211
4800 Oak Grove Drive
Pasadena, CA 91109

NASA Resident Office-JPL
Technology Utilization Officer
Mail Stop 180-801
4800 Oak Grove Drive
Pasadena, CA 91109

Patent Counsel
Mail Code 180-801
4800 Oak Grove Drive
Pasadena, CA 91109

George C. Marshall Space Flight Center
Technology Utilization Officer
Code AT01
Marshall Space Flight Center, AL 35812

Patent Counsel
Mail Code CC01
Marshall Space Flight Center, AL 35812

John C. Stennis Space Center
Technology Utilization Officer
Code HA-30
Stennis Space Center, MS 39529

NASA Headquarters
Technology Utilization Officer
Code CU
Washington, DC 20546

Assistant General Counsel for Patent Matters
Code GP
Washington, DC 20546

Dryden Flight Research Center
Technology Utilization Officer
M/S D21-31
Bldg. 4832 Whse 7
Lilly Dr.
Edwards, CA 93523

BLANK PAGE

NASA TechBriefs

National Aeronautics and
Space Administration

May 1997
97-05

BLANK PAGE

Electronic Components and Circuits

Hardware, Techniques, and Processes

BLANK PAGE

Noise and Impedance Generator for Cryogenic Testing of HEMTs

Spurious effects from room-temperature test circuits would be reduced.

NASA's Jet Propulsion Laboratory, Pasadena, California

A monolithic, integrated, coolable probe is being developed for use in measuring the cryogenic noise parameters of high-electron-mobility transistors (HEMTs) at the wafer-processing stage of production. The integrated circuitry in the probe would include a noise source and impedance generator integrated with a coplanar-waveguide probe circuit.

This development is prompted by a fundamental physical limitation on the accuracy and repeatability of low-temperature HEMT noise-parameter measurements performed with commercial noise sources and impedance generators, which operate at room temperature: In preparation for such a measurement, one attaches a room-temperature noise source and impedance generator to the room-temperature ports of cryogenic, coplanar on-wafer probes. The probes are lossy and introduce noise temperatures comparable to or greater than the noise temperature of the device under test (DUT). For example, in a typical test in the frequency range of 2 to 18 GHz, the noise-temperature measurement error can go beyond ±25 K, while the noise temperature of the DUT is <10 K.

To obtain the most accurate and repeatable measurements of noise parameters at low temperatures, one should place the impedance generator within a waveguide wavelength (at the test-signal frequency) of the DUT and should use a noise source with a noise temperature comparable to that of the DUT. The developmental probe would be designed to satisfy these requirements. The probe would be compatible with other cryogenic probes designed for measuring scattering (S) parameters over a frequency range of 1 to 40 GHz. The integration and use of probes of both types would enable the efficient, accurate, and nondestructive characterization of HEMTs and of circuits that contain them. The use of these probes in characterizing HEMTs under cryogenic conditions at the wafer level would eliminate the need for the expense and labor of dicing, mounting, and wire bonding needed to characterize HEMTs by present techniques.

The figure illustrates some aspects of alternative proposed designs. Calibrated noise diodes would be inserted in a coplanar-waveguide circuit that would be coupled to the impedance generator. The topology of the impedance generator would have to be chosen to enable integration into the coplanar-waveguide format and to reduce resonant modes. One of two proposed alternative design concepts, following a narrow-band approach, calls for all passive components to minimize insertion loss and added noise. A hybrid coupler would be used to provide isolation and to pad the noise signal, and a series tapered coplanar transmission line would be used to provide up to eight predetermined impedance states.

The other alternative design concept, following a broader-band approach, would entail the development of a low-loss active impedance generator. An optimal tuner topology could be derived for a tunable impedance network consisting of various transmission lines connected through positive/intrinsic/negative (PIN) diodes to form open shunt stubs or matched transmission lines.

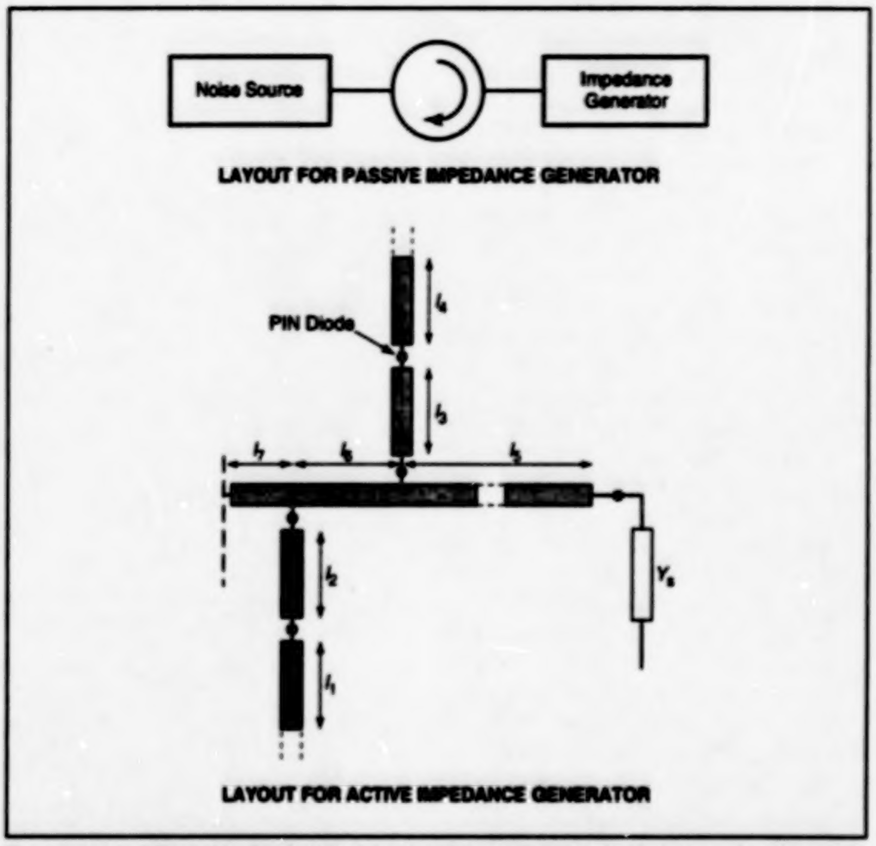

The Layout Is Affected by the design of the impedance generator. Active and passive alternative design concepts are under consideration.

The design would have to provide a proper interface between the probe and the input terminals of the DUT. The interface could be analyzed and designed by use of finite-element techniques. Among other things, the interface would have to be analyzed for propagation in higher resonant modes to enable accurate noise characterization. Gum ferrite sheet would be used as an electromagnetic absorber to suppress spurious modes. Finally, the complete three-dimensional mathematical model of the integrated active probe would be studied to insure proper signal propagation and compatibility with currently available network-analyzer facilities.

This work was done by Joy Laskar of Georgia Tech and J. Javier Bautista of Caltech for **NASA's Jet Propulsion Laboratory.** *Further information is contained in a TSP [see page 1].*
NPO-19577

A Planar Separate-Bias Scheme for SHP Two-Diode Waveguide Mixers

Bias connections are made via a compact trilayer metal/insulator/metal planar filter structure that functions as a single-layer filter and yet provides separate dc path for each diode.

NASA's Jet Propulsion Laboratory, Pasadena, California

A very compact arrangement for the individual biasing of two antiparallel planar Schottky diodes in a waveguide-based subharmonically-pumped (SHP) mixer has been proposed and tested. SHP mixers require a local oscillator (LO) at half the signal frequency (RF) to produce intermediate-frequency (IF) output and are often preferred at very high frequencies where the LO power for fundamentally-pumped mixers is unavailable, and yet, SHP mixers without individual bias require 2 to 4 times more LO power, albeit at a lower frequency, than fundamental mixers. To reduce the LO power requirements for SHP mixers, separately-biased diodes have been used in prior circuit implementations. However, these implementations have needed extra ports and fairly large bypass capacitors for dc isolating the devices. The concomitant increase in the size and complexity of the circuitry makes such implementations unattractive for high-frequency waveguide mixers. The present scheme utilizes the vertical space in a waveguide channel resulting in a compact, stripline-coupled biasing circuit.

A separate-bias concept has been implemented in both a 200- and a 640-GHz SHP mixer that includes a split waveguide block and a quartz-substrate stripline circuit (see figure). The block is based on a prior SHP mixer design, requiring only minor modifications for adding the separate-bias capability. The stripline circuit consists of an LO bandpass filter/transmission line, two antiparallel diodes, and a novel metal/insulator/metal trilayer IF low-pass filter/transmission line. The dc connection to each diode is made via the two identically-patterned metal conductors of the IF circuit, each of which can be a stand-alone filter. They are stacked over the same circuit area and separated by an 8,000-Å layer of silicon nitride. The thin nitride film ensures that these conductors are capacitively coupled so that they function together as a single IF filter but are dc isolated.

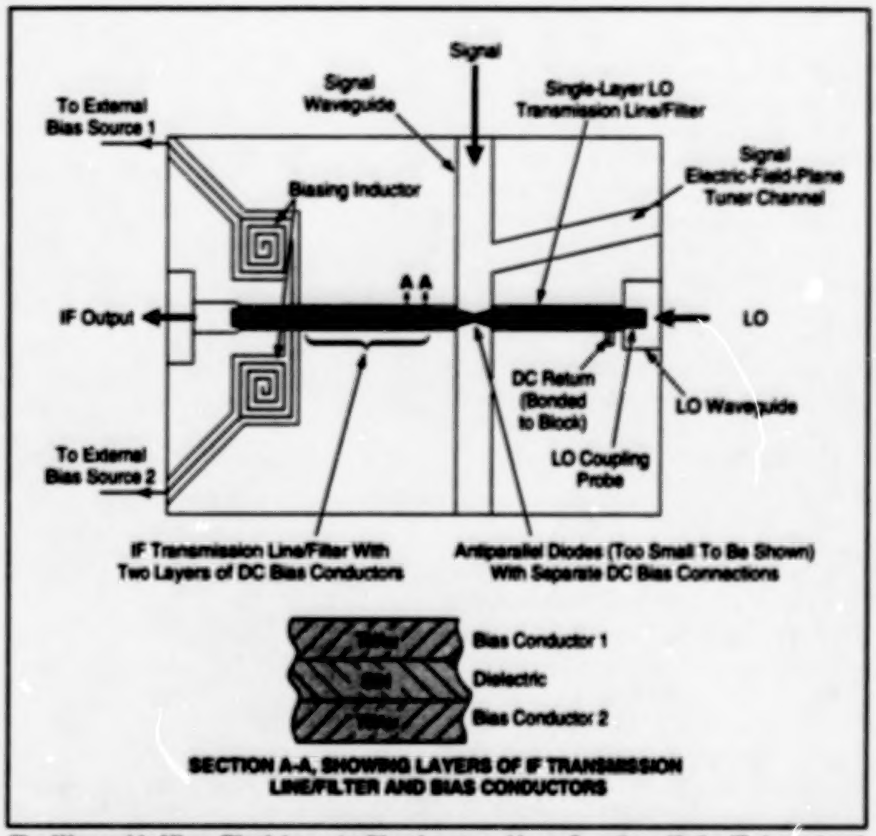

The Waveguide Mixer Block has a traditional cross-guide configuration with the IF channel and LO waveguide perpendicular to the received-signal waveguide. The separate-bias two-conductive-layer IF transmission line/filter is housed in the IF channel; a similar transmission line/filter that provides electrical coupling between the diodes and the LO waveguide is housed in the LO channel.

Preliminary characterization of the prototype circuits in waveguide SHP mixers at 200 and 640 GHz have been completed. At 200 GHz, the application of appropriate bias can reduce the LO power requirement by 3 dB with only a 10 to 15 percent degradation in mixer performance. These results clearly indicate that this scheme is viable, and work is presently underway to optimize this design for a NASA spaceborne Earth remote-sensing instrument Microwave Limb Sounder.

This work was done by Trong-Huang Lee, Imran Mehdi, and Peter H. Siegel of Caltech for **NASA's Jet Propulsion Laboratory**. *Further information is contained in a TSP [see page 1].*
NPO-19832

Improved Capacitive Gap Sensors for Micromachined Devices

Shielding electrodes would suppress capacitive coupling with the micromachined semiconductor material.

NASA's Jet Propulsion Laboratory, Pasadena, California

An improvement has been proposed for the capacitive sensors that are used to measure displacements between structural members in micromachined electromechanical sensors and actuators. These micromachined devices are made largely of semiconducting materials (usually silicon), the electromagnetic properties of which vary with temperature and with electric fields, including the electric fields of the capacitive sensors. In a typical device of this type, the capacitive coupling with the semiconducting material therefore introduces spurious temperature- and electric-field-dependent signal components that degrade the accuracy of the capacitive measurement of displacement (see

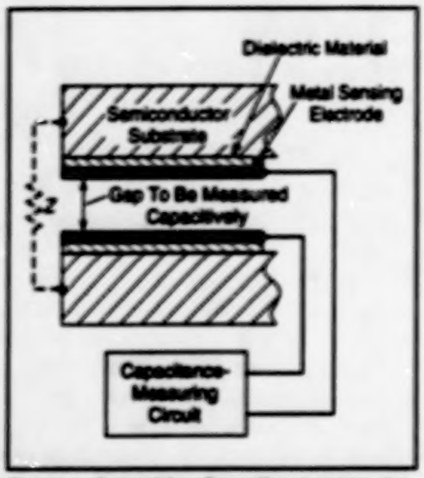

Figure 1. Capacitive Coupling between the sensing electrodes and the semiconductor substrates introduces spurious temperature- and electric-field dependent signal components (represented here as originating in the additional series impedance Z).

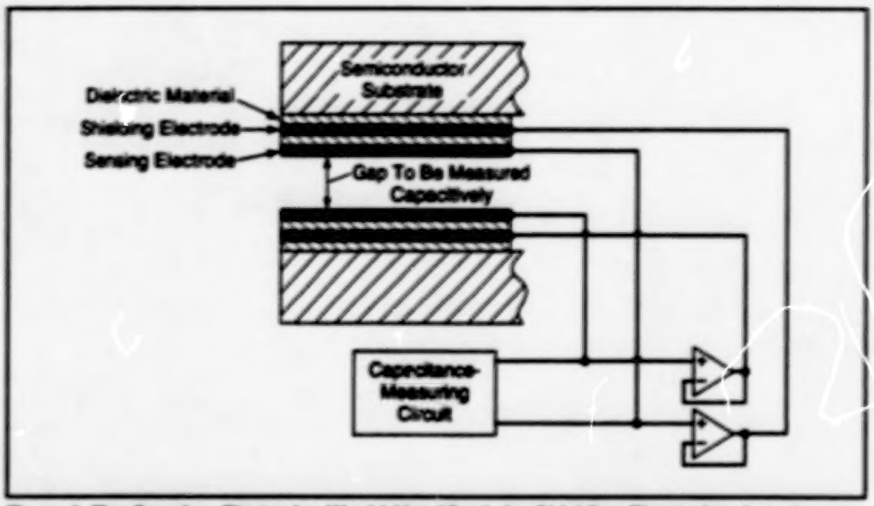

Figure 2. The Sensing Electrodes Would Not "See" the Shielding Electrodes, from the perspective of capacitive coupling, because the shielding electrodes would be driven at the same potentials. Because of the shielding effect, the sensing electrodes would also not "see" the semiconductor substrates. However, the sensing electrodes would "see" each other, as desired.

Figure 1). The proposed improvement would eliminate these spurious signal components.

The proposed improvement is based on the shielding-electrode concept, (shielding electrodes have also been called "guard" electrodes), which has been used for many years and in many different applications to suppress spurious capacitive coupling. Instead of mounting the sensing electrodes in nearly direct contact and in close capacitive coupling with the micromachined semiconductor substrates, the sensing electrodes would be incorporated into sandwich structures that would include shielding electrodes interposed between the sensing electrodes and the semiconductor substrates (see Figure 2). A layer of dielectric material (which would be relatively insensitive to temperature and electric field) would separate each sensing electrode from its shielding electrode, and another layer of the dielectric material would separate the shielding electrode from the substrate.

Of the circuit configurations that could be used to implement the shielding electrode principle, the one shown in Figure 2 is conceptually the most straightforward (though not necessarily the most practical). By use of a high input-impedance, unity-gain buffer amplifier, each shielding electrode would be driven at the same voltage as that applied to the associated sensing electrode. This arrangement would effectively eliminate capacitive coupling between the sensing electrode and the semiconductor substrate; each sensing electrode would be capacitively coupled only to the other sensing electrode and other nearby objects on the side facing away from the shielding electrode.

This work was done by Benjamin P. Dolgin, Frank T. Hartley, and Paul M. Zavracky of Caltech for **NASA's Jet Propulsion Laboratory.** *Further information is contained in a TSP [see page 1].*
NPO-19739

Successive-Approximation ADCs With Capacitive Coupling

These circuits could be incorporated into focal-plane arrays of photodetectors.

NASA's Jet Propulsion Laboratory, Pasadena, California

Two closely related types of ultra-low-power, successive-approximation analog-to-digital converter (ADC) circuits with capacitive coupling are undergoing development. These are prototypes of ADC circuits that are to be incorporated into integrated-circuit focal-plane arrays of photodetectors in advanced video cameras. The incorporation of these ADCs would contribute to miniaturization and to reduction in the number of integrated circuits and would provide digital output without need for separate ADC circuits, while maintaining high speed and low power dissipation.

The basic concept of a successive-approximation ADC has long been known and can be summarized as follows: An

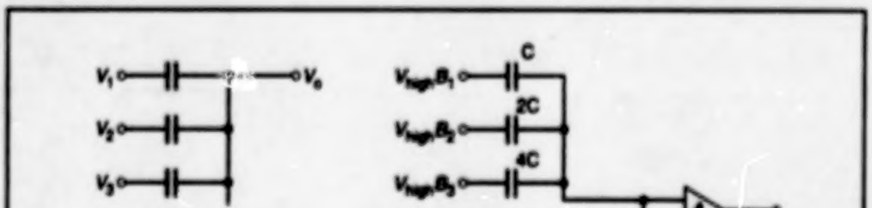

Figure 1. A CC-MDAC is based on the relationship among changes in voltages in a simple capacitor network.

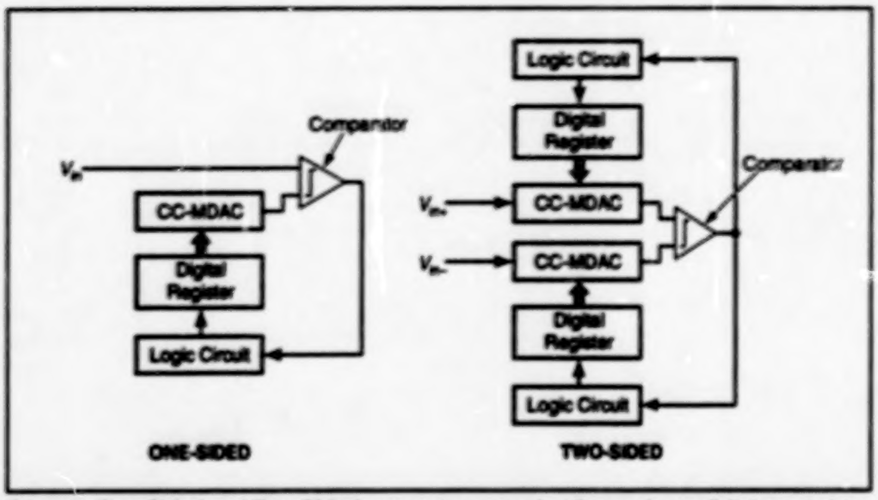

Figure 2. One-Sided and Two-Sided successive-approximation analog-to-digital converters (ADCs) with capacitive coupling are undergoing development. Functional units of both types have been constructed.

input voltage (v_{in}) that one seeks to represent digitally is compared with a known voltage (v_{out}) that has been generated by a digital-to-analog converter. A succession of such comparisons is made, starting with the most significant bit and proceeding toward the least significant bit. At each comparison, the next, less significant bit for next comparison is adjusted according to whether v_{in} is greater or less than v_{out}. Thus, v_{out} is made to converge toward v_{in} in steps and, equivalently, the precision of the digital representation increases in steps. A succession of n such comparisons yields a digital representation of v_{in} with a precision of n bits. In cases in which precision no greater than 10 bits is needed, the small number of comparisons offers an advantage of high speed and low power dissipation.

For generating known voltages to be compared with input voltages, the developmental ADCs utilize capacitively coupled multiplying digital-to-analog converters (CC-MDACs). A CC-MDAC is based on the relationship between the change (Δ) in each of the input voltages V_j (j = 1 to m) and the change in the output voltage V_0 of the simple capacitor network shown in the left part of Figure 1. It can easily be shown that

$$\Delta V_0 = \frac{\sum_{j=1}^{m} C_j \Delta V_j}{\sum_{j=1}^{m} C_j}$$

In a CC-MDAC, shown on the right, the bit lines are coupled via capacitors to the input node of a high-input-impedance amplifier. The capacitor for the second bit has twice the capacitance of that for the first bit, the capacitor for the third bit has four times that for the first bit, and so forth.

Initially, all bits are set to zero (represented by zero voltage) and the clamping switch is turned on momentarily to set the amplifier input node at an initial potential of V_{clamp}. Next, each bit is set to its assigned value of zero or one, a one being represented by a voltage V_{high} on the bit line. Using the equation shown above, it can be shown that the resulting output potential of the CC-MDAC is given by

$$v_{out} = A[V_{high}(B_1 + 2B_2 + 4B_3 + \ldots 2^{m-1}B_m) + V_{clamp}]$$

where A is the voltage gain of the amplifier and B_j denotes the value (0 or 1) of the jth bit.

Figure 2 illustrates the two types of developmental successive-approximation ADCs containing CC-MDACs. The one-sided version could be used for nondifferential or differential input; the two-sided circuit is better suited to differential input. In the case of differential input in the one-sided version, one side of the input could be used to establish V_{clamp}. Any error associated with the clamping voltage and/or caused by voltage offset in the comparator can be corrected digitally, either by incorporating a corrective offset into the digital input to the CC-MDAC, or by similarly offsetting the digital output. The two-sided version may prove to be inherently less affected by comparator offset and clamping errors.

This work was done by Eric Fossum and Zhimin Zhou of Caltech for **NASA's Jet Propulsion Laboratory**. *Further information is contained in a TSP [see page 1].*

In accordance with Public Law 96-517, the contractor has elected to retain title to this invention. Inquiries concerning rights for its commercial use should be addressed to

Larry Gilbert, Director
Technology Transfer
California Institute of Technology
Mail Code 315 - 6
Pasadena, CA 91125
(818) 395-3288

Refer to NPO-19783, volume and number of this NASA Tech Briefs *issue, and the page number.*

Successive-Approximation ADCs With Charge Balancing

These circuits implement an alternative approach to successive approximation.

NASA's Jet Propulsion Laboratory, Pasadena, California

The figure illustrates a complementary metal oxide/semiconductor (CMOS) analog-to-digital converter (ADC) of a type that is undergoing development for eventual incorporation into focal-plane arrays of photodetectors. This circuit can be used as an alternative to the circuits described in the preceding article, "Successive-Approximation ADCs With Capacitive Coupling" (NPO-19783). A functional 10-bit prototype of this circuit fits within an area 24 μm wide and 3.8 mm long.

This circuit offers the same advantages as do those described in the preceding article, and like those circuits, this one is based on the concept of successive approximation. However, this circuit differs from those of the preceding article in that it implements successive approximation according to a charge-balancing approach, in which two branches of the circuit successively accumulate successively halved increments of charge in an attempt to balance the charges in the two branches.

This circuit includes two equal sample-and-hold capacitors ($C_1 = C_2$), two charge-integrating amplifiers (A) with feedback capacitors ($C_R = C_S$), a comparator, flip-flops for buffering the digital output feedback to the input terminals of the

charge-integrating amplifiers, and a shift register. Initially, the charges in both branches of the circuit are set to zero. Next, the signal voltage (V_S) that one seeks to digitize is converted to the charge domain by use of the sample-and-hold capacitors. Then by use of other electronic switches, the resulting charge is transferred to the charge-integrating amplifier in the "S" branch of the circuit. (If the signal voltage is differential instead of one-sided as shown in the figure, then the voltage from the second signal line is similarly converted to charge and put onto the "R" branch of the circuit.) Next, the reference voltage (V_R) is similarly converted to a reference charge, which is then split in half by use of C_1, C_2, and the electronic switches between them.

A sequence of comparisons of charges in the "R" and "S" branches then begins. After the first comparison, the 1/2 reference charge is transferred from C_2 to whichever branch contains less charge (as indicated by the output of the comparator). The 1/2 reference charge that remains on C_1 is then split into two 1/4 reference charges. The charges on the two branches are again compared, and the 1/4 reference charge on C_2 is transferred to the branch that contains less charge. This process is repeated to obtain an n-bit digital representation of the signal voltage: The first comparison represents the most significant bit and each successive comparison represents the next less significant bit. Each time the "R" branch is selected to receive half of the remaining fraction of reference charge, the corresponding bit is set to "1"; otherwise, it is set to zero.

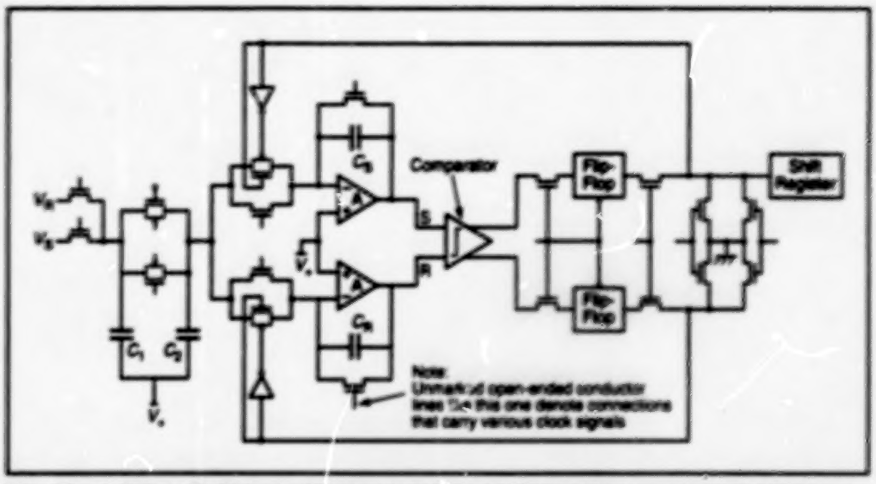

This Circuit Strives To Balance Charges in its "R" and "S" branches, successively adding successively halved fractions of a reference charge to whichever branch contains less charge. By going through n cycles of comparison and increment of charge, the circuit achieves an n-bit digital representation of V_S.

This work was done by Eric Fossum, Bedabrata Pain, and Zhimin Zhou of Caltech for **NASA's Jet Propulsion Laboratory**. *Further information is contained in a TSP [see page 1].*

In accordance with Public Law 96-517, the contractor has elected to retain title to this invention. Inquiries concerning rights for its commercial use should be addressed to

Larry Gilbert, Director
Technology Transfer
California Institute of Technology
Mail Code 315 - 6
Pasadena, CA 91125
(818) 395-3288

Refer to NPO-19784, volume and number of this NASA Tech Briefs *issue, and the page number.*

Selectable PCM Format Generator

The Selectable Pulse-Code-Modulation (PCM) Format Generator ("SPF Generator," for short) is a portable, lightweight test apparatus used to verify the capability of ground support equipment (GSE) prior to connecting the GSE to telemetric flight electronic equipment, and to verify the proper operation and configuration of demultiplexers. The SPF Generator was developed to replace a PCM Simulator that had to be programmed anew, by use of push-button panel switches, for each new telemetry-data format. By means of a switch, the SPF Generator can be made to use either a clock signal generated externally or a clock signal generated internally by a crystal oscillator, counters, and comparators. The clock signal is used to control address counters in an Erasable Programmable Read-Only Memory (EPROM). There are six EPROMs, one of which is selected via a rotary switch to select the required data format. At each address, a byte of information is read from the chosen EPROM and sent to a parallel-in/serial-out shift register. The data are then transformed into emitter-coupled-logic-level signals for an interface with the GSE. A computer program written to facilitate the use of the SPF Generator prompts the user for input parameters needed to construct a telemetry file, then programs the file into the EPROMs.

The hardware was designed by Diana Manent and the software was written by Torrey Maggard, and José J. Amador of **Kennedy Space Center**. *Further information is contained in a TSP [see page 1].*

Inquiries concerning rights for the commercial use of this invention should be addressed to the Patent Counsel, Kennedy Space Center [see page 1]. Refer to KSC-11842.

BLANK PAGE

12

Electronic Systems

Hardware, Techniques, and Processes

BLANK PAGE

Beacon Monitoring Would Reduce Interactions With Remote Systems

Communications and operations costs would be significantly reduced.

NASA's Jet Propulsion Laboratory, Pasadena, California

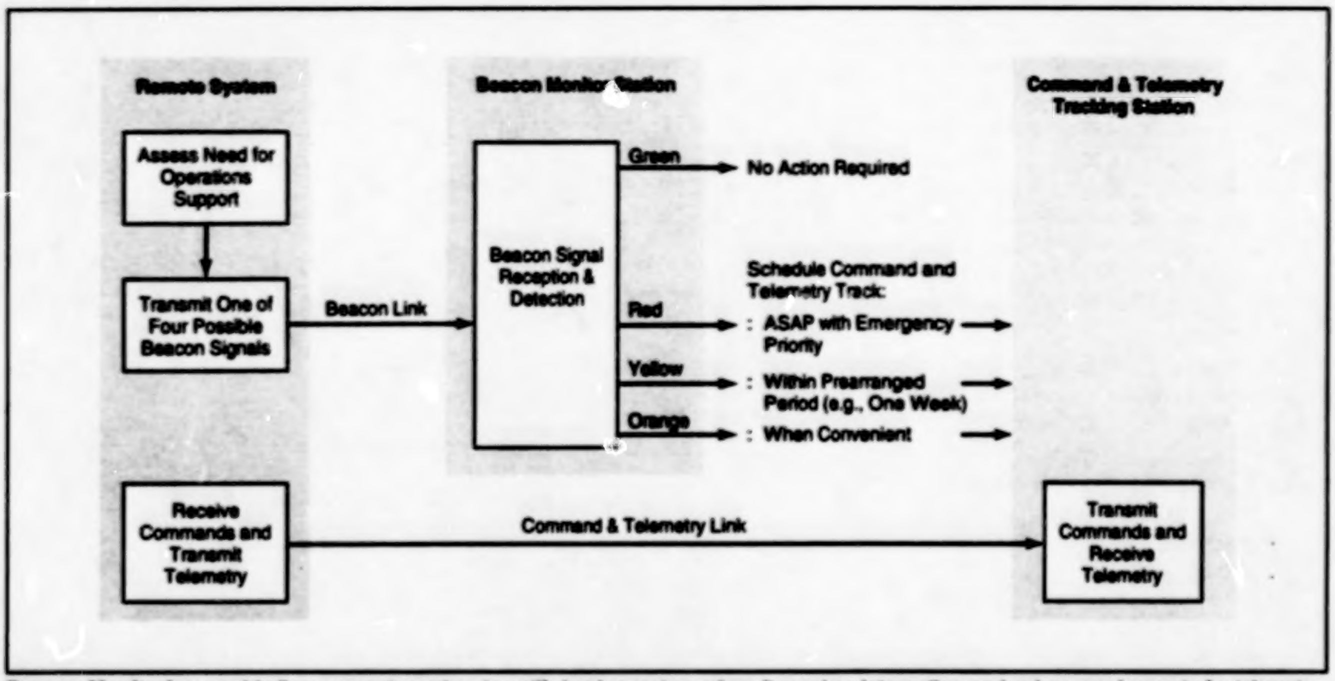

Beacon Monitoring would allow a remote system to notify local operators when it requires interaction and reduce requirements for telemetry communications and human operator interaction.

"Beacon monitoring" denotes a concept for allowing a remote system to notify local operators when it requires interaction. Historically, remote systems with little or no intelligence have had to transmit large amounts of system status data to operators, requiring reliable communications links, lengthy transmission times, and complex data reception and detection equipment. Human operator experts must monitor and analyze these data and decide when further interaction with the remote system is required.

In the future, many remote systems will have the intelligence to analyze their status data on their own. The responsibility for deciding when interaction is required between the remote system and local operators will transfer to the remote system. The beacon-monitoring concept reduces the need for the remote system to transmit routine telemetry data and for routine operator interaction. Instead, it provides the ability for the remote system to transmit a simple message that requests one of four actions from operations:

(1) Green: Leave me alone. I am functioning normally and no interaction by operations experts is required.
(2) Red: Contact me as soon as possible. I require operations support on an emergency priority basis.
(3) Yellow: Contact me within a certain prearranged amount of time or I will start performing in a degraded mode (e.g., losing or overwriting data, running out of commands, and the like).
(4) Orange: Contact me at your convenience. An event has occurred that may be of interest to operations and that operations may want to collect information sooner than the next scheduled telemetry contact.

The first intended applications for this technology are for JPL spacecraft that are equipped with appropriate onboard monitor and decision-making intelligence (specifically, New Millennium and Pluto Express). These spacecraft will have the capability of requesting ground action by transmitting one of four beacon signals implemented as one of four possible subcarrier tone pairs or some other radio signaling scheme that is simple to generate and detect. The simplicity of the beacon signals allows detection at lower signal-to-noise ratios, with smaller receiving antennas, and with significantly less complex and expensive receiving and detection equipment than that required for traditional telemetry.

The JPL operational concept for using the beacon is that the spacecraft will point at Earth and continuously transmit one of the four beacon tones. Once a day, whenever it is convenient, the ground will monitor the beacon. If it is green, it will be logged in and the spacecraft will be ignored until the next day. If the beacon is found to be red, yellow, or orange, the ground will schedule a traditional telemetry track and command the spacecraft when to begin downlinking telemetry. The procedures for scheduling these tracks will vary as a function of the difference in urgency among the red, yellow, and orange beacons.

This new beacon-monitoring technology is projected to provide significant flight operations cost savings by:

- reducing the need to routinely downlink large amounts of status telemetry,
- reducing the human tasks associated with the capture and analysis of routine status telemetry, and
- reducing the loading on large-aperture DSN (Deep Space Network) antennas and complex telemetry reception and detection equipment.

Beacon monitor technology may be the key to enabling low cost operational support of fleets of spacecraft that may be flying simultaneously in the near future.

This work was done by John Carraway, E. Jay Wyatt, Richard Doyle, and Bruce Crow of Caltech for **NASA's Jet Propulsion Laboratory.** *Further information is contained in a TSP [see page 1].*

NPO-19706

Time-Interval Unit Achieves Picosecond Resolution

An improved interpolation technique involves sampling the phase of a clock signal.

Goddard Space Flight Center, Greenbelt, Maryland

An electronic circuit measures the time between "start" and "stop" pulses to a resolution of the order of a picosecond. Like other electronic time-interval units, this one includes a coarse-resolution time counter (which counts the number of clock periods) and measures time to a resolution finer than one clock period by use of start-time and stop-time interpolators. The interpolators used in other time-interval units contain various sources of error that degrade the achievable accuracy and resolution.

The present time-interval unit features an improved interpolation scheme based on sampling of the phase of the clock signal. This scheme involves sampling of the clock signal, using GaAs or other high-speed, low-jitter semiconductor integrated sampling circuitry for increased accuracy.

This time-interval unit includes a clock-signal generator, which provides a sinusoidal clock waveform at a frequency nominally between 2 and 5 GHz. The "start" and "stop" pulses typically originate as optical (laser) pulses and are converted to electrical form by photodetectors followed by fast threshold comparators. The "start" and "stop" pulses are fed to the coarse-resolution time counter, which measures the integer part, n, of the number of clock cycles between the pulses and thus indicates time to a resolution of one clock period, T.

The pulses are also fed to the start-time and stop-time sampling interpolators, which are identical. The clock signal entering each interpolator is fed directly to one of the input terminals of a dual-channel sampling head. A 90°-phase-shifted (quadrature) version of the clock signal is fed to the other input terminal of the sampling head. When triggered by a "start" or "stop" pulse, the sampling head acquires the instantaneous values x and y of the in-phase and quadrature versions, respectively (see figure).

These values are fed to a circuit that computes the smaller of $|y/x|$ or $|x/y|$, as part of computing the clock phase angle at the trigger time, $\theta = \tan^{-1}(y/x)$ or $\theta = \cot^{-1}(x/y)$. The time elapsed from the beginning of the present clock period to the "start" or "stop" pulse is computed from $t_i = T\theta/2\pi$, where $i = 1$ for start, 2 for stop. Finally, the outputs of the interpolators are used to compute the unknown time interval Δt between the "start" and "stop" pulses from $\Delta t = nT + t_2 - t_1$.

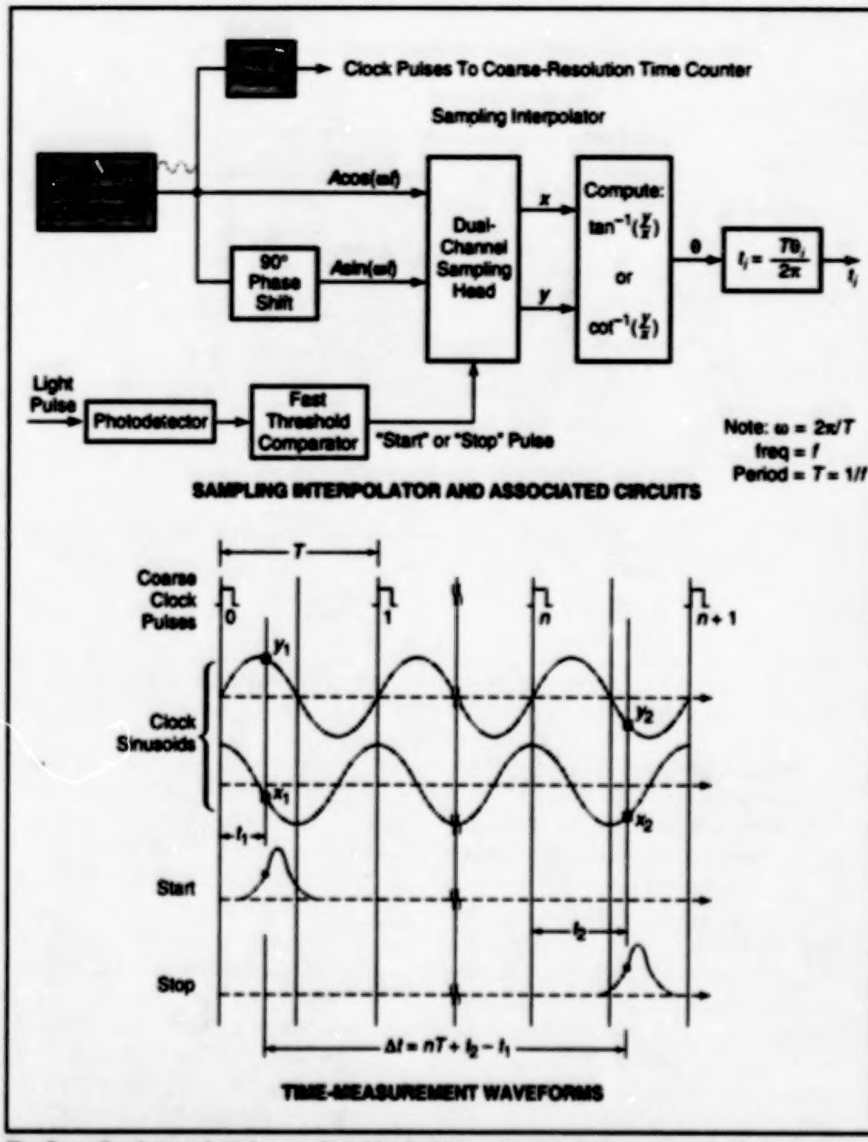

The Sampling Interpolator is one of two identical interpolators in the time-interval unit. It measures the phase angle of the clock signal at an instant associated with a "start" or "stop" pulse. This phase angle is directly proportional to the time elapsed between the beginning of the clock period and the "start" or "stop" pulse.

This work was done by James B. Abshire of **Goddard Space Flight Center**. *Further information is contained in a TSP [see page 1].*

This invention has been patented by NASA (U.S. Patent No. 5,566,139). Inquiries concerning nonexclusive or exclusive license for its commercial development should be addressed to the Patent Counsel, Goddard Space Flight Center [see page 1]. Refer to GSC-13505.

Computing Supportable Bit Rates in Radio Communications

Designs and performances can be analyzed quickly.

NASA's Jet Propulsion Laboratory, Pasadena, California

A computer program quickly estimates parameters that characterize the performance of a free-space radio-communication system in which a carrier signal is modulated with binary phase-shift keying to transmit digital signals. One important performance parameter is the maximum supportable bit rate, which is the bit rate above which the system is expected to incur a bit-error rate (BER) above some specified allowable value. The program calculates maximum supportable bit rates as functions of various design parameters and operating conditions, plus other quantities that are useful in designing the system.

To determine the maximum supportable bit rate, one must create a systematic table of gains and losses of the link; such a table is called the "link budget." The ultimate outputs of any link budget are the link data margin, the link carrier margin, and, if the link uses a ranging signal, then the ranging margin. The various link margins are logarithmic (decibel) measures of the signal power beyond that needed to ensure performance at a specified level. For a fixed power, performance can be improved (in the sense that the bit-error rate can be decreased) by decreasing the data rate. In other words, one can trade the data rate against the link margins.

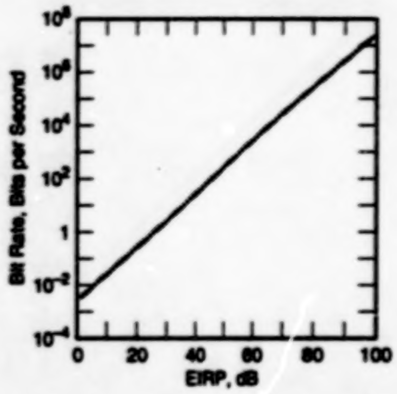

This is a Typical Example of the Output of the Program. It can be used to find the maximum bit rate supported by a given effective isotropically radiated power (EIRP) or the EIRP needed to support a given bit rate.

In a typical link budget, the largest gains are attributable to the directional patterns of the transmitting and receiving antennas, while greatest losses are attributable to (1) the dispersion of power in the expansion of wavefronts during propagation and (2) the equivalent noise temperature of the receiver. Smaller losses are attributable to the transmitting and receiving equipment and to atmospheric and ionospheric dispersive effects.

The computer program is based on established equations for the various gains and losses and for the relationship among the various gains, losses, and margins. The inputs to the program represent the applicable design parameters and operating conditions. These inputs include the frequency band, the distance between the transmitter and the receiver, the power radiated by the transmitting antenna, the total of all the losses mentioned above, the maximum allowable BER, the diameters of the transmitting and receiving antennas, the desired data margin, and the choice of transmitting the data either uncoded or in one of nine error-correcting codes. Given these inputs, the program computes the maximum supportable data rate.

The program is written in the Excel 5.0 software system, which was chosen because it offers excellent number-handling and charting capabilities. For example, the program can generate a plot of the maximum supportable bit rate as a function of the radiated power, as illustrated in the figure.

This work was done by Anil Kantak and Faiza Lansing of Caltech for **NASA's Jet Propulsion Laboratory**. *Further information is contained in a TSP [see page 1].* *NPO-20039*

BLANK PAGE

18

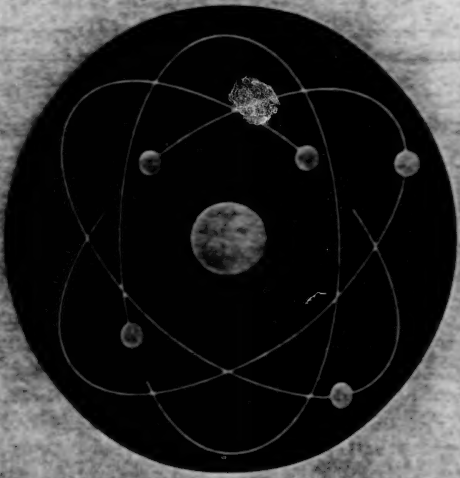

Physical Sciences

Hardware, Techniques, and Processes

BLANK PAGE

Miniature Boundary-Layer Airfoil With Embedded Hot Wires

Flow could be measured on and very close to surfaces.

Lewis Research Center, Cleveland, Ohio

A miniature instrument has been proposed for measuring flow on and near a surface of interest. Called a "micro hot wire chip," the instrument would be based on the established concept of hot-wire anemometry and would be fabricated by techniques used to make computer chips.

The instrument (see figure) would include an airfoil that would protrude from the surface of interest and that would contain multiple hot-wire anemometers. By providing data on the flow near the surface, the instrument would contribute to understanding of turbulence and other complex flow phenomena. Such understanding may eventually make it possible to reduce skin friction in a variety of machines ranging from aircraft to watercraft such as submarines.

At its base, the airfoil would be integral with a block mounted flush with the surface of interest. The airfoil and block would be made of a thermally insulating material to reduce calibration and wall-proximity errors. Except at the leading and trailing edges, the airfoil would be configured with constant thickness so that the velocity in the midlength region on each side would be constant and equal to the velocity upstream from the airfoil. The hot wires would have rectangular cross sections and would be embedded at the surface of the airfoil at various distances from the surface of interest. One or more wire(s) could also be embedded in the base block for measuring the slip velocity at the surface of interest.

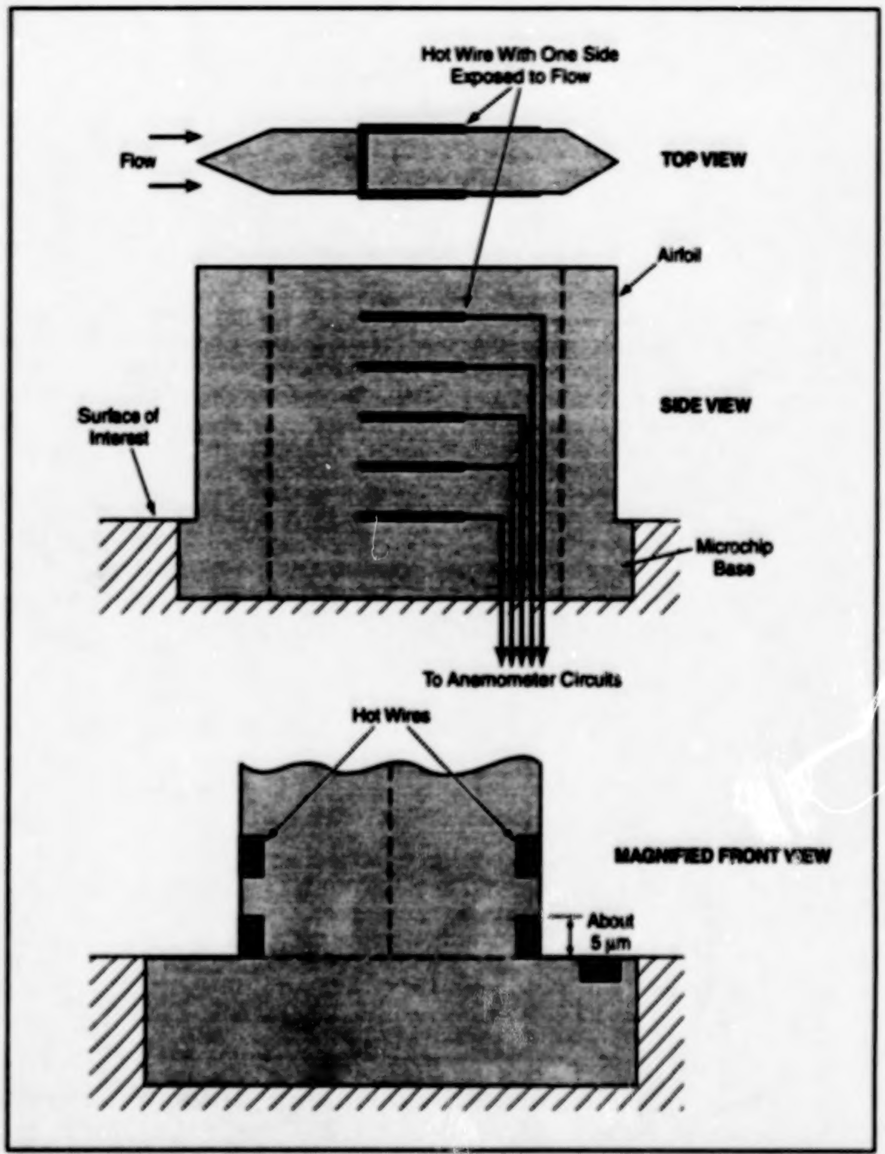

Thin Wires Would Be Embedded at the surface of a small protruding airfoil for measuring flow by the hot-wire-anemometer principle at various distances from a surface of interest.

Other instruments (including hot-wire anemometers) for measuring flow velocities near surfaces are available, but none is capable of measuring closer than about 0.02 in. (about 0.5 mm) from the surface. In the proposed instrument, the wires would be only about 0.0002 in. (about 5 µm) thick and one of them could be positioned just above the surface of interest. Thus, the proposed instrument would yield data on flows down to 1/100 of the previous lower limit on distance from the surface.

This work was done by Danny P. Hwang of **Lewis Research Center**. *Further information is contained in a TSP [see page 1].*

Inquiries concerning rights for the commercial use of this invention should be addressed to the Patent Counsel, Lewis Research Center [see page 1]. Refer to LEW-16229.

Fast, High-Sensitivity Dew-Point/Frost-Point Hygrometer

Response is faster than that of a chilled-mirror dew-point hygrometer.

NASA's Jet Propulsion Laboratory, Pasadena, California

Figure 1 schematically illustrates an improved dew-point/frost-point hygrometer — an instrument for measuring the reduced temperature at which ambient air becomes saturated with its present water-vapor content and the vapor begins to condense to liquid water or ice. Like the relative humidity, the dew point or frost point is a useful measure of

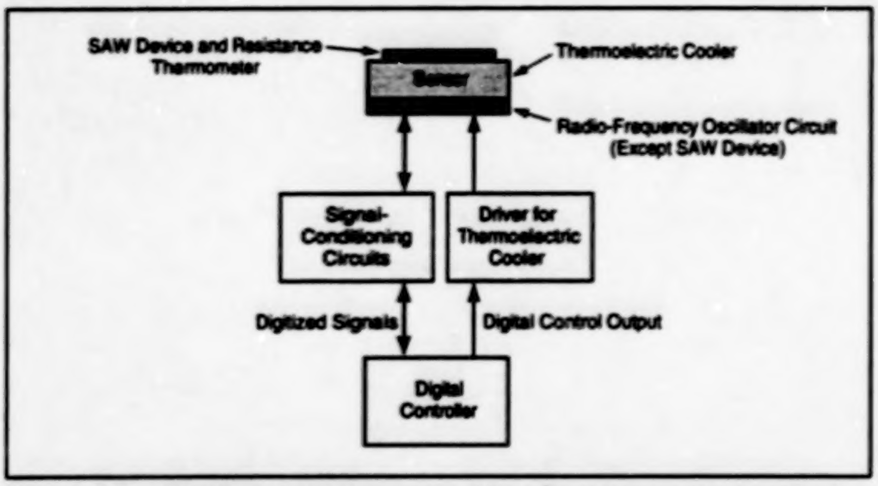

Figure 1. A Dew-Point/Frost Point Hygrometer of the present type operates according to a unique condensation-detection principle and to a feedback-temperature-control principle. Some aspects of the design and operation resemble those of older SAW-based and chilled-mirror dew-point/frost-point hygrometers.

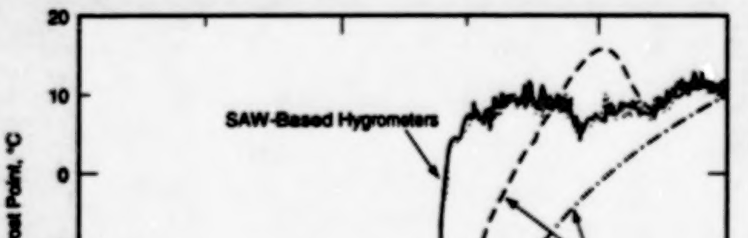

Figure 2. Relatively Small, Rapid Changes in the dew point or frost point can be tracked by the hygrometers of the present type, but are missed by the chilled-mirror hygrometers.

the water-vapor content of air and is widely used in meteorology and numerous other applications.

An instrument of the present type exploits feedback control of the temperature of a condensation-sensitive transducer to maintain equilibrium between condensation and evaporation. The condensation-sensitive transducer is a surface-acoustic-wave (SAW) device that serves as the resonant frequency-selecting element of a radio-frequency oscillator. The frequency of oscillation is extremely sensitive to condensation on the surface of the SAW device; thus, a change in the frequency of oscillation provides a sensitive and rapid indication that the temperature of the SAW device is at or very near the dew or frost point.

The SAW device, its oscillator circuitry, and a low-power electrical-resistance thermometer are mounted together on a thermoelectric cooler. The output of the oscillator is mixed to a lower frequency, filtered, amplified, and processed to obtain a raw digital indication of the frequency. Because the frequency depends somewhat on temperature in addition to surface condensation, the raw digital frequency-shift reading is corrected by use of frequency-vs.-temperature data derived from calibration measurements taken when the SAW device was known to be dry. The corrected frequency-shift reading thus provides the desired indication of the amount of liquid water or ice condensed on the SAW surface.

The corrected frequency-shift digital signal and the digitized output of the resistance thermometer are fed to a digital feedback controller, the digital output of which controls the current supplied to the thermoelectric cooler. The digital controller executes a feedback control algorithm that incorporates calibration parameters to adjust the temperature to correct for any deviation of the corrected frequency-shift reading from a value indicative of the onset of condensation. Thus, the controller constantly adjusts the temperature of the SAW device to track the evolving level of moisture in the ambient air, and the output of the resistance thermometer therefore necessarily indicates the temperature of the onset of condensation; that is, the dew or frost point.

Two dew-point/frost-point hygrometers of the present type were tested alongside two state-of-the-art commercial chilled-mirror hygrometers, which are based on a similar principle that they measure changes in condensation optically — in terms of changes in the reflectivities of chilled mirrors. The tests involved exposure to external air during the descent of an airplane. The data acquired during the tests (see Figure 2) indicate that the steady-state accuracy of the present SAW-based hygrometers is comparable to that of the chilled-mirror hygrometers, and that the present hygrometers respond much faster to changes in the dew point.

This work was done by Michael E. Hoenk of Caltech for **NASA's Jet Propulsion Laboratory.** *Further information is contained in a TSP [see page 1].*

In accordance with Public Law 96-517, the contractor has elected to retain title to this invention. Inquiries concerning rights for its commercial use should be addressed to

Larry Gilbert, Director
Technology Transfer
California Institute of Technology
Mail Code 315 - 6
Pasadena, CA 91125
(818) 395-3288

Refer to NPO-20006, volume and number of this NASA Tech Briefs *issue, and the page number.*

High-Pressure, High-Temperature Oxygen DTA/TGA System

This system was designed for safely evaluating materials for resistance to ignition and combustion.

Marshall Space Flight Center, Alabama

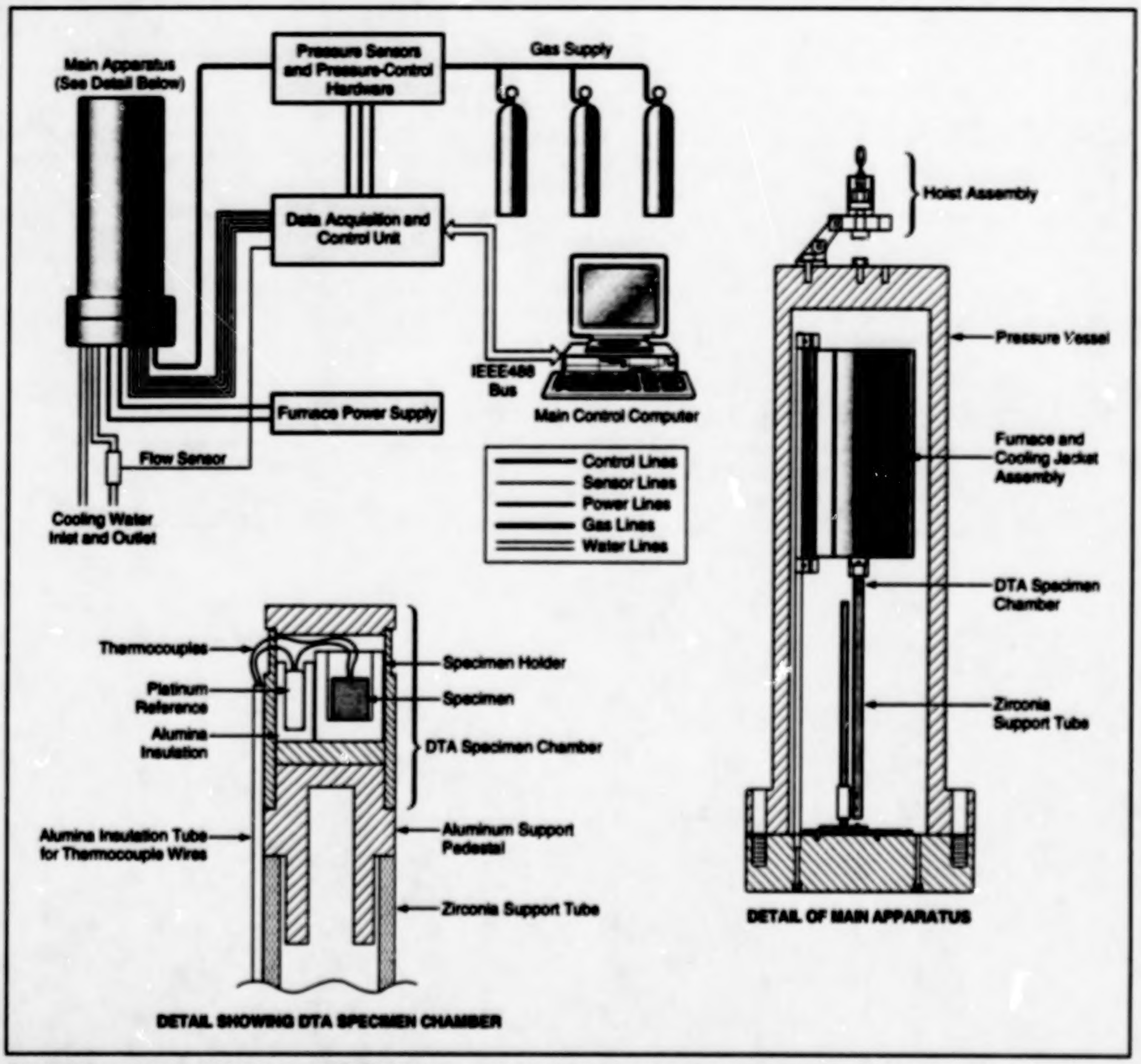

This High-Temperature, High-Pressure DTA/TGA System produces data that can be used to rank materials with respect to ability to resist ignition and combustion in a high-pressure oxygen atmosphere.

The figure illustrates a laboratory system for performing differential thermal analysis (DTA) and thermogravimetric analysis (TGA) of specimens of materials at high temperatures in high-pressure oxygen. The system was designed for evaluating the resistance to oxidation and combustion of both metals and nonmetals that might be used in oxygen-handling equipment. Specimen parameters that can be determined by use of this system include ignition and combustion temperatures, temperatures at the onset of major and/or catastrophic oxidation, and thermochemical activation energies that can be used in calculating rates of oxidation. The system can also be used to determine the fundamental parameters of chemical reactivity of material specimens with gases other than oxygen, as long as those gases are compatible with the internal system materials.

The system includes a main apparatus, which is a stainless-steel pressure vessel that contains an electric furnace for heating the specimen to the test temperature in the oxygen or other test atmosphere at the test pressure. The system also includes a gas-supply subsystem with pressure-sensing and -controlling equipment, a data-acquisition and system-control unit, a computer, a furnace power supply, and plumbing for cooling water.

The specimen is contained in a DTA or TGA assembly within the main apparatus. These two assemblies are interchangeable with respect to mounting in the main apparatus. Each assembly comprises a DTA or TGA specimen chamber on top of a zirconia support tube on an adjustable-height

platform. The specimen chambers are made of alumina, which was chosen for its stability, chemical inertness, and low electrical conductivity at high temperatures in oxidizing atmospheres.

The DTA assembly contains four Pt/(Pt/10 percent Rh) (type-S) thermocouples, which measure the furnace-control, furnace-monitor, specimen, and reference temperatures. The specimen and reference thermocouples are connected in a differential arrangement that yields an additional temperature-related difference between the specimen- and reference-thermocouple voltages. The TGA assembly (not shown in the figure) includes a microbalance, small pressure-resistant chambers for a servo photocell and source of light, a specimen-mounting subassembly, a counter-balance subassembly, a tare subassembly, and a balance stand.

The system has the following unique features:

- It yields useful readings at temperatures up to 1,500 °C (about 1,800 K) and pressures up to 34.5 MPa in both the DTA and TGA modes.
- The position and dimensions of the furnace are chosen to maximize the working space available for the TGA or DTA assembly and minimize the convection of heated gas. This minimization of convection (especially at high temperature and pressure) is essential for TGA.
- The electrical and mechanical subsystems and the computer hardware and software are fully accessible, so that the user can perform adjustments for special situations.
- The system operates safely, even though it contains oxygen at high temperature and pressure.
- Ignition, combustion, and onset-of-oxidation temperatures can be measured to within approximately 1.6 °C

This work was done by James W. Bransford of James W. Bransford & Associates for **Marshall Space Flight Center**. *Further information is contained in a TSP [see page 1].*

Inquiries concerning rights for the commercial use of this invention should be addressed to the Patent Counsel, Marshall Space Flight Center [see page 1]. Refer to MFS-26419.

Three-Dimensional Long-Trace Profilometer

Figures of cylindrical and conical surfaces can be measured without contact.

Marshall Space Flight Center, Alabama

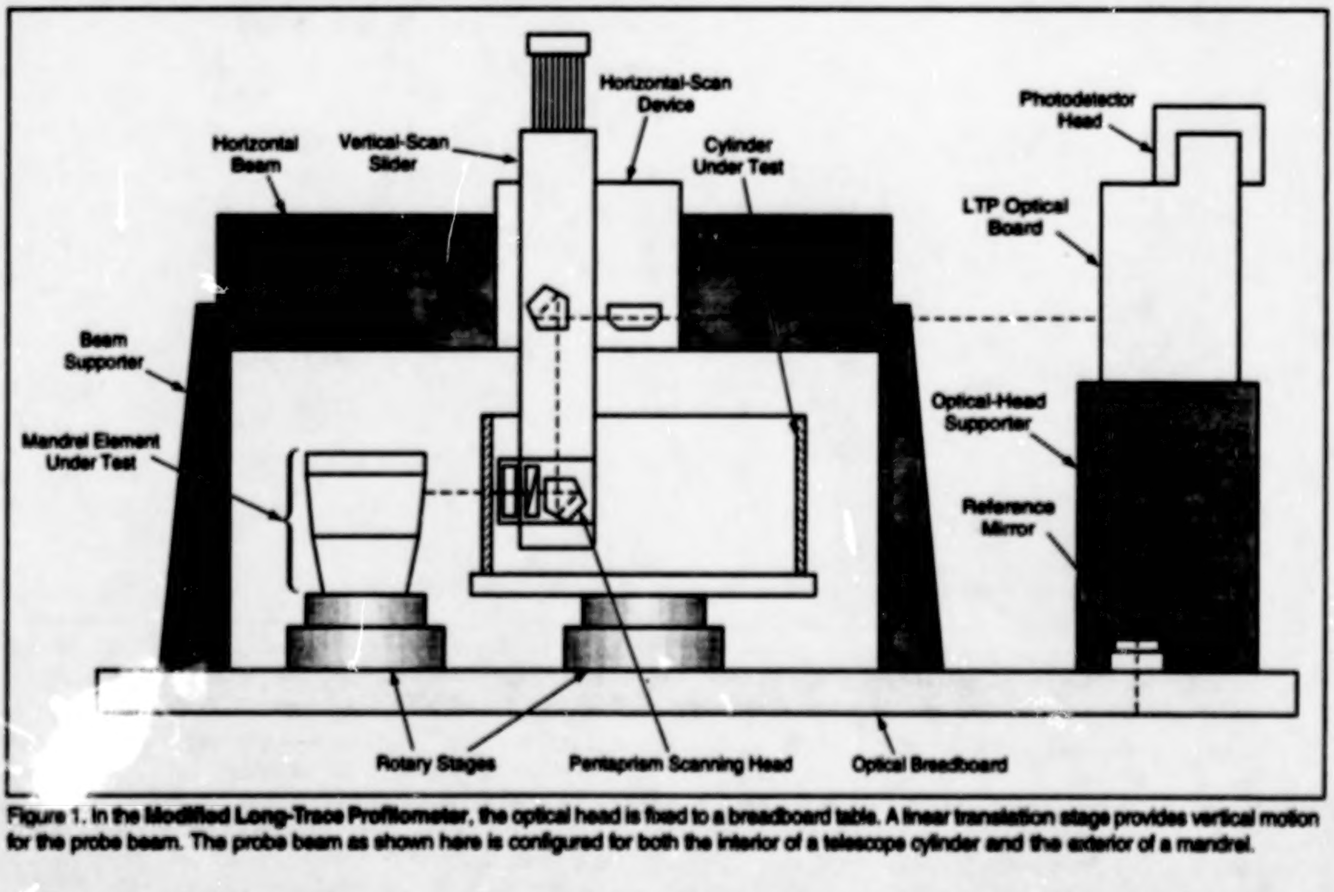

Figure 1. In the **Modified Long-Trace Profilometer**, the optical head is fixed to a breadboard table. A linear translation stage provides vertical motion for the probe beam. The probe beam as shown here is configured for both the interior of a telescope cylinder and the exterior of a mandrel.

An interferometric optical noncontact metrological instrument measures the three-dimensional surface figures of optical components with high precision. The instrument is designed especially for measuring (1) the interior surfaces of glass and metal cylinders and cones that are used as glancing-incidence reflectors in x-ray telescopes and (2) the exterior surfaces of polished mandrels from which thin-shell metal conical and cylindrical optics are made. The instrument is a modified version of the Long Trace Profilometer II (LTP II), which is a commercial slope-measuring interferometer that, during the past decade, has become the de facto world standard for synchrotron-radiation x-ray mir-

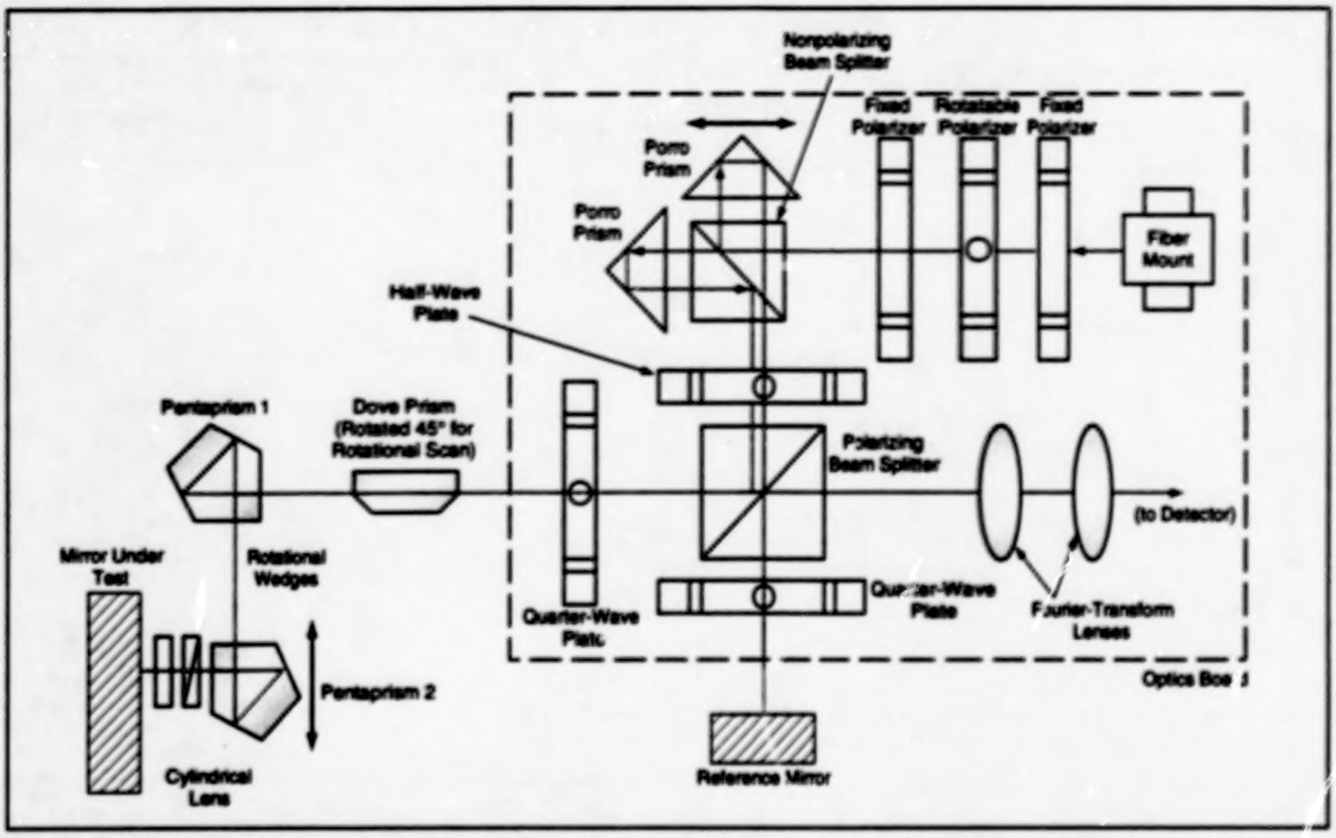

Figure 2. The Major Components of the Optical Head are shown here schematically. Items enclosed in the dashed-line box are parts of the unmodified LTP II. Other items are additions needed for the vertical-scanning capability.

rors. Results from the proof-of-principle experiment indicate that the modified LTP II is capable of three-dimensional measurement of surfaces of typical telescope parts with slope errors less than one microradian and height errors as small as a few nanometers.

The unmodified LTP II performs a horizontal line scan with two parallel and mutually coherent probe laser beams aimed downward onto an approximately or nominally horizontal surface. The two beams are separated by 1 mm along the horizontal scan axis. The optical and optoelectronic subsystems of the unmodified LTP II are contained in an optical head that is scanned by moving it along a bridgelike structure that stands over and spans the mirror or other surface under test.

The difference between the heights of the surface at the two beam spots is measured in terms of the difference between the phases of reflections of the two probe beams, and this difference in height divided by the horizontal distance between the probe beams is taken as a direct measure of the local surface slope in the vertical plane defined by the laser beams and scan line. The slopes thus measured can be integrated along the scan axis to obtain the relative surface height as a function of position along the scan axis; this amounts to two-dimensional information about the scanned surface.

The LTP II was modified into the present instrument to satisfy a need for three-dimensional measurements of nominally or approximately vertically oriented surfaces — especially vertically oriented cylinders and cones. (In the case of highly precise conical and cylindrical x-ray-telescope reflectors, the vertical orientation is necessary to minimize surface errors caused by sagging of the reflectors under their own weights.) The modification included the addition of a vertical translation stage for the optical head, plus a rotary stage for turning the cylinder or cone of interest about a vertical axis (see Figure 1); together, these stages provide a two-dimensional scan, which enables complete (three-dimensional) characterization of the scanned surface.

A pair of pentaprisms mounted on the vertical-translation stage make it possible to direct the laser beams at right angles onto the scanned mirror surface, with no error introduced into the measurement by imprecise motion of the translation stage. To provide an adjustment for scanning a conical (as distinguished from a cylindrical) surface, the modification of the LTP II also included the addition of means for offsetting the direction of the probe beams by use of a pair of Risley prisms. This adjustment enables one to add a bias to the direction of the probe beams so that they are normal to the average tilt angle of the surface. One of the benefits of this adjustment is that the measurement light spot remains centered on the array of photodetectors and utilizes the entire dynamic range of the system.

This work was done by Haizhang Li of Continental Optical Corp. for **Marshall Space Flight Center**. *Further information is contained in a TSP [see page 1].*

Inquiries concerning rights for the commercial use of this invention should be addressed to the Patent Counsel, Marshall Space Flight Center (see page 1). Refer to MFS-26386.

Polarimetric Microwave Radiometry for Measuring Ocean Winds

Anisotropy of thermal radiation is related to wind and its effects on waves.

NASA's Jet Propulsion Laboratory, Pasadena, California

$$\text{Stokes Vector} = \begin{bmatrix} I \\ Q \\ U \\ V \end{bmatrix} = \begin{bmatrix} T_v + T_h \\ T_v - T_h \\ T_p - T_m \\ T_l - T_r \end{bmatrix} = c \begin{bmatrix} \langle E_v E_v^* \rangle + \langle E_h E_h^* \rangle \\ \langle E_v E_v^* \rangle - \langle E_h E_h^* \rangle \\ 2\,\mathrm{Re}\,(\langle E_v E_h^* \rangle) \\ 2\,\mathrm{Im}\,(\langle E_v E_h^* \rangle) \end{bmatrix}$$

T_h : Brightness Temperature in Horizontal Polarization
T_v : Brightness Temperature in Vertical Polarization
T_p : Brightness Temperature in 45° Polarization
T_m: Brightness Temperature in −45° Polarization
T_l : Brightness Temperature in Left-Hand Circular Polarization
T_r : Brightness Temperature in Right-Hand Circular Polarization

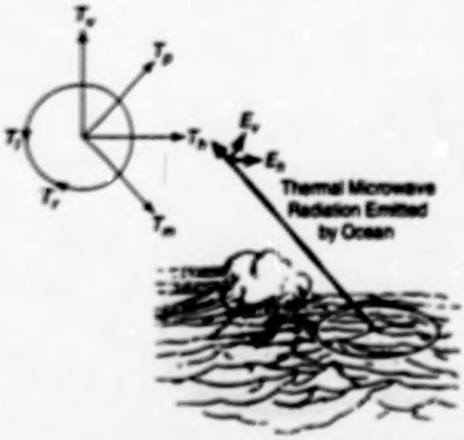

Figure 1. The **Stokes Parameters** (the components of the Stokes vector) summarize the information on amplitudes and relative phases of vertical and horizontal polarization components of the received radiation in a form that is convenient for some computations. In this case, the Stokes parameters are expressed in terms of brightness temperatures in the various polarizations.

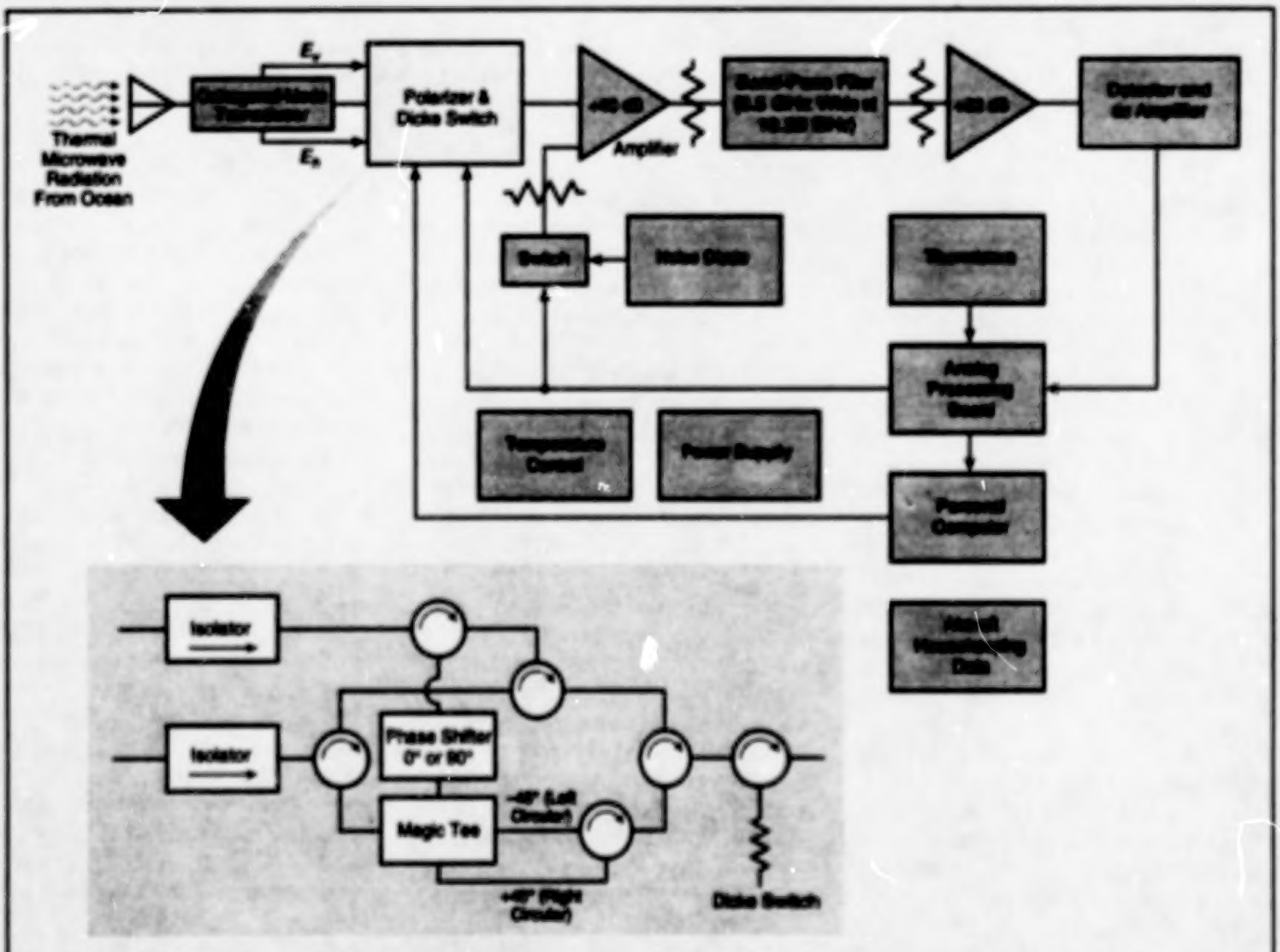

Figure 2. This **Polarimetric Radiometer** includes a waveguide switch network containing a magic tee; this network forms the various polarization components in preparation for measuring the brightness temperatures in those components.

A developmental method of estimating ocean-surface wind velocity is based on the interactions between winds and waves and the resulting anisotropy of thermal radiation emitted by the ocean surface. The method involves remote sensing by one or more polarimetric microwave radiometer(s) aboard an aircraft, which circles the ocean location of interest so that measurements can be taken at a suitable angle or angles of incidence (typically, 40° or 50°) and various azimuth angles. The polarimetric radiometric data are processed into Stokes parameters (see Figure 1). The azimuthal dependence of the Stokes parameters can be taken as an indication of the direction of the wind.

Figure 2 illustrates a polarimetric radiometer designed to take the required readings in initial experiments at a frequency of 19.35 GHz. The electric fields entering the antenna are split into horizontal and vertical (from the observation perspective) polarization components E_h and E_v, respectively, by an orthogonal-mode transducer. A waveguide switch network then produces four polarizations from E_h and E_v. A magic tee in the waveguide switch network is used to form the sum and the difference of the vertically and horizontally polarized electric fields to produce the +45° and -45° linear polarizations with the phase shifter set at the 0° phase-shift position. If the phase shifter is set at the 90° phase-shift position by a manual switch, the +45° and -45° linear polarizations become right- and left-hand circular polarizations. At each polarization setting, 22 pairs of antenna and reference load measurements are taken, corresponding to an integration time of 88 ms, and are reduced to one brightness-temperature sample. Four polarizations, including vertical, horizontal, -45° linear (or left-hand circular), and +45° linear (or right-hand circular) polarizations, are scanned sequentially, with switch positions commanded by a personal computer, to obtain four brightness-temperature samples, T_v, T_h, T_m (or T_l), and T_p (or T_r).

A second radiometer designed to operate at a frequency of 37 GHz is similar, except that it does not include the 90° phase shifter. Moreover, for lack of time, the 90° phase shifter in the 19-GHz radiometer was not used in initial experiments, so that data on T_l and T_r were not obtained and thus the fourth Stokes parameter was not determined. In one set of experiments, the 19-GHz polarimetric radiometer took readings at angles of incidence of 30° to 50°, from a DC-8 airplane circling wind-measuring buoys moored in the Pacific Ocean off the northern California coast. In a second set of experiments, both radiometers took readings at angles of incidence of 45°, 55°, and 65°. In both sets of measurements, the Stokes parameters in units of brightness temperature exhibited upwind-vs.-downwind anisotropies of the order of a few Kelvins; this finding lends credence to the hypothesis that microwave polarimetric radiometry can be used to determine the direction of the wind at the surface of the ocean. Presumably, the amplitudes of the azimuthal dependences of the Stokes parameters are indicative of the speed of the wind, but quantitative relationships between these amplitudes and wind speeds have yet to be established.

This work was done by Simon H. Yueh, William J. Wilson, Son V. Nghiem, and Fuk K. Li of Caltech for **NASA's Jet Propulsion Laboratory**. *Further information is contained in a TSP [see page 1].*
NPO-19583

Measuring Complex Permittivity of a Microwave-Heated Sample

Complex permittivity can be determined as a function of temperature.

NASA's Jet Propulsion Laboratory, Pasadena, California

An improved technique for measuring the complex permittivity of a microwave-heated sample of dielectric material provides for simultaneous control of heating power and/or measurement of the temperature of the sample. This technique is based partly on the established cavity perturbation technique, in which the real and imaginary parts of the permittivity of a small sample are calculated from the values of the resonance quality factor (Q) and resonance frequency (f_r) of the microwave cavity measured with and without the sample present. Older techniques based on the cavity perturbation technique do not provide for control of power and/or temperature, and are therefore not useful for characterizing samples at temperatures above ambient when only one microwave frequency is used for heating and detection.

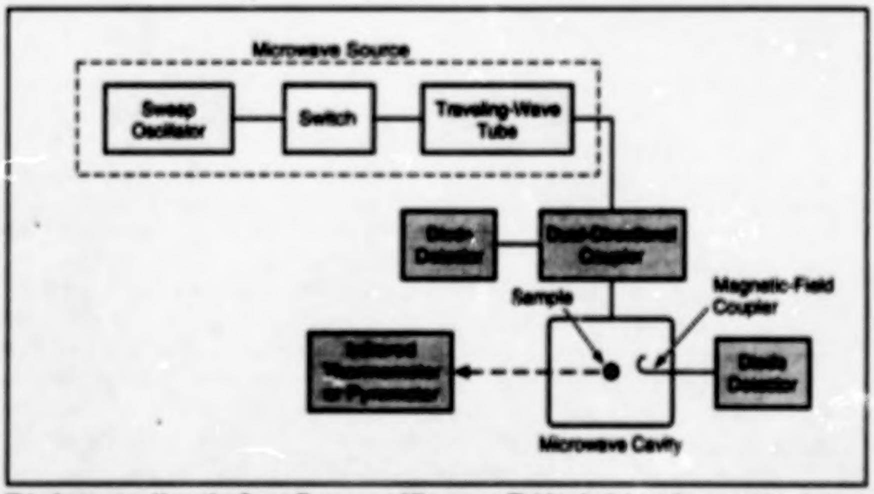

This Apparatus Uses the Same Resonant Microwave Field to both heat the sample and measure its complex permittivity. The apparatus includes circuitry that controls the power dissipated in the sample and the walls of the microwave cavity, plus other circuitry that adjusts the microwave frequency to track the resonance of the cavity with the sample present.

The complex permittivity of a dielectric material is a measure of its microwave-absorption properties and of some other physical and chemical properties. The complex permittivity is often called the complex "dielectric constant" even though it is not constant; indeed, one could use the present technique to measure the change in the complex permittivity of a sample during microwave heating and/or other processing to monitor the extent to which the material has been converted to the desired end condition.

In the present technique, one uses the same microwave field to both heat the sample in a controlled manner and measure its complex permittivity. The apparatus

used in this technique (see figure) includes a microwave source, the frequency and power of which can both be controlled. The frequency of the source is made to track f_r even as f_r changes somewhat with the condition of the heated sample; the f_r-tracking technique was described in "Measuring Q and f_r of a Microwave Cavity: Part II" (NPO-19356), *NASA Tech Briefs*, Vol. 19, No. 12 (December 1995), page 36. Controlling the frequency in this way confers two benefits: First, because the frequency is always at or close to f_r, power is delivered efficiently to heat the sample even as the dielectric parameters of the sample change during continued heating. Second, f_r can be continuously monitored by use of a frequency counter connected directly to the output of the oscillator.

Diode detectors are used to measure the forward power (P_F) traveling from the microwave source to the microwave cavity and the reflected power (P_R) traveling from the cavity back to the source, so that the net power transmitted into (and thus dissipated in) the cavity (P_T) can be calculated from $P_T = P_F - P_R$. The apparatus includes computer-controlled circuitry for maintaining P_T at a desired value. A third diode detector connected to a magnetic-field coupler in the microwave cavity measures a power (P_D) that can be shown to be proportional to the energy (E_M) stored in the resonant electromagnetic field in the cavity.

The total power transmitted into the cavity can be expressed as $P_T = P_S + P_W + P_E$ where P_S is the power dissipated in heating the sample, P_W is the power dissipated in heating the wall of the cavity, and P_E is the power loss in the input electronics. By continuously maintaining the critical coupling between the microwave source and cavity using an automatic impedance-tracking technique developed previously, the reflected power will be zero and power dissipated in the electronics will be equal to the power dissipated in the cavity. The resonance quality factor of the cavity is then given by $Q_T = 2\pi f_r E_M/P_T$. By virtue of the equation for the power-dissipation components, one can write $1/Q_T = 2(1/Q_W + 1/Q_S)$, where $Q_W = 2\pi f_r E_M/P_W$ and $Q_S = 2\pi f_r E_M/P_S$. Then the reciprocal of the quality factor associated with the sample is given by $1/Q_S = {}^1/_2 Q_T - 1/Q_W$. Provided that the temperature of the wall is maintained approximately constant (e.g., by cooling it with water) Q_W is independent of P_T and of the temperature (T) of the sample. By making substitutions from the equations and definitions above, the equation for $1/Q_S$ can be rewritten as $1/Q_S = P_T/2\pi f_r G_M P_D - 1/Q_W$, where G_M is the factor of proportionality between E_M and P_D ($G_M = E_M/P_D$). G_M depends only on the geometry of the cavity and magnetic coupler and can be determined from a low-power calibration measurement in the absence of the sample. By use of cavity perturbation theory, one can compute the complex permittivity of the sample from $1/Q_S$.

In a typical experiment, one sets P_T to a desired value while measuring T by use of a pyrometer or other noncontact device. Once T settles to a steady value, one measures f_r and P_D. One then increases P_T in steps and repeat the measurement procedure at each step to accumulate sets of data on P_T, f_r, and P_D at various increments of T corresponding to the increments of P_T. From these data, one obtains $1/Q_S$ as a function of T and thus also the complex permittivity of the sample material as a function of T.

This work was done by Martin Barmatz and Henry W. Jackson of Caltech for **NASA's Jet Propulsion Laboratory**. *Further information is contained in a TSP [see page 1].*
NPO-19773

Penetrator and Dart NMR Probes

Conventional sampling procedures would not be necessary.

NASA's Jet Propulsion Laboratory, Pasadena, California

The figure shows the major parts of penetrator and dart nuclear-magnetic-resonance (NMR) probes for analyzing soils and other materials. Originally intended for use during exploration of other planets, these probes might also be useful in remote analyses of soils and other materials on Earth. The terms "penetrator" and "dart" signify that the probes would be pushed or dropped into the materials to be sampled. The use of these probes would eliminate the need for such conventional sampling procedures as scooping up samples and placing them inside NMR coils; although such procedures are easy for human technicians on location, they are difficult to perform by use of robots or telemanipulators.

A penetrator NMR probe would include a cylindrical Halbach permanent-magnet assembly surrounding a hollow cylindrical NMR radio-frequency (RF) coil surrounding a hollow sample cylinder. Three 1 × 2-in. (25.4 × 50.8-mm) surface-mount boards holding electronic signal-processing circuitry could be placed in the upper portion of the probe. Upon insertion of the probe into the material to be analyzed, either a sample of the material could be pushed up into the sample tube from the bottom opening, or else the sample could fall in from the top opening. The probe could be operated in either the continuous-wave or pulsed NMR detection mode.

In its basic principle of operation, a dart NMR probe would be similar to NMR probes that are lowered into predrilled oil-well holes to detect surrounding oil. However, a dart NMR probe would push its way into the sample material, without need for a predrilled hole. In comparison with oil-well NMR probes, a dart NMR probe would be smaller and would consume less power.

In a dart NMR probe, two cylindrical permanent magnets would be positioned astride an axial gap with opposite polarities (north poles facing each other along the axis), so that a significant part of the permanent magnetic field would reach out into the surrounding sample material. An RF coil would be placed in the gap between the magnets; the RF magnetic field would also reach out into the surrounding material. Like oil-well NMR probes, a dart NMR probe would be operated in the pulsed NMR detection mode; pulsed operation would help to compensate for the effects of inhomogeneity of the permanent magnetic field in the particular opposite-polarity configuration. Dart NMR probes would offer two advantages over penetrator NMR probes; there would be no need to ensure that the samples entered sample cylinders, and there would be no need for concern over plugging of sample cylinders.

This work was done by Soon Sam Kim of Caltech for **NASA's Jet Propulsion Laboratory**. *Further information is contained in a TSP [see page 1].*
NPO-19651

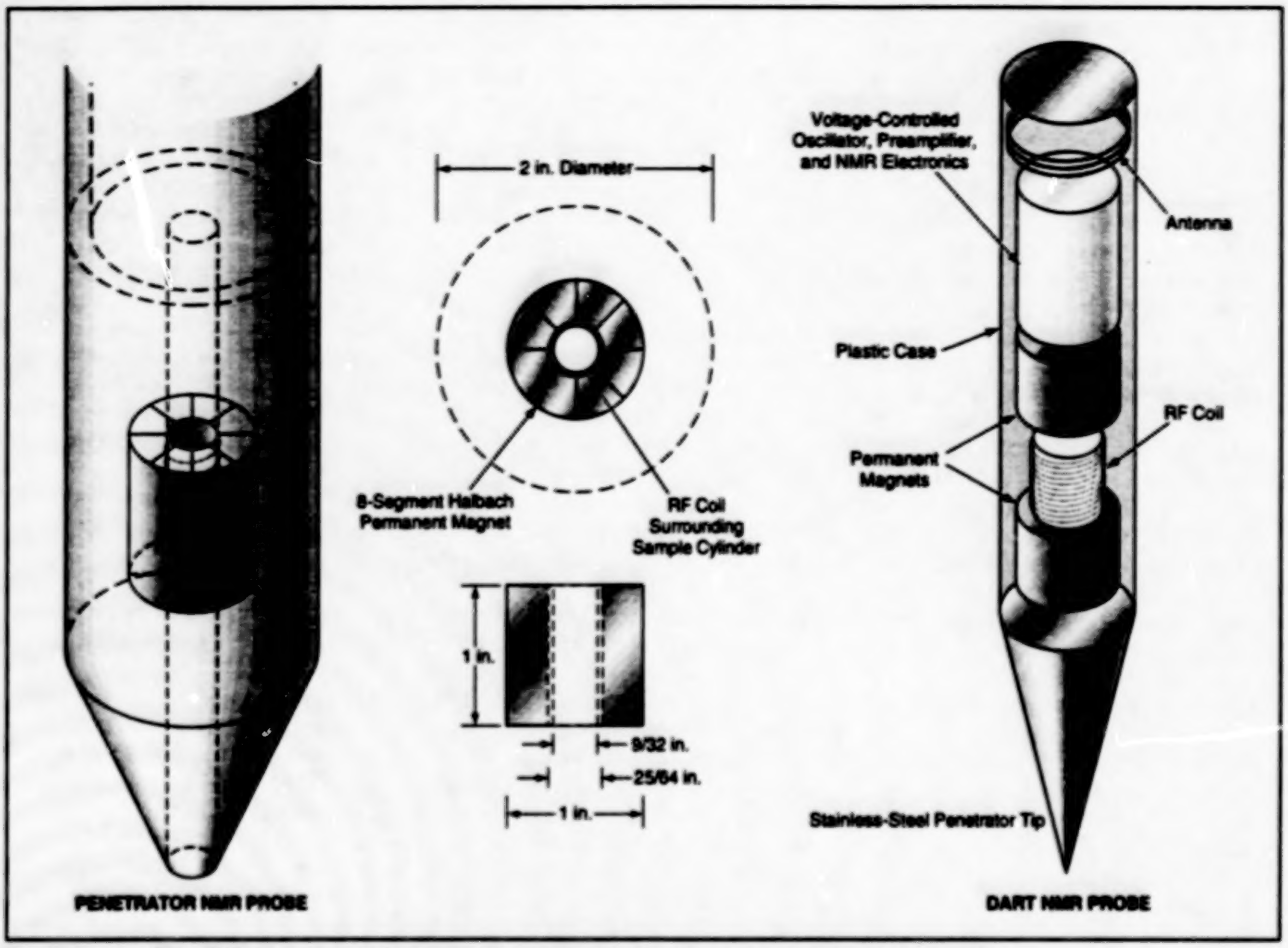

Penetrator and Dart NMR Probes would be dropped or pushed into the soils or other materials to be sampled.

Computing Erosion in Three-Grid Ion Thrusters

A computer code is based on particle-in-cell and Monte Carlo concepts.

NASA's Jet Propulsion Laboratory, Pasadena, California

A computer code is undergoing development for use in numerical simulation of erosion of the grids in three-grid ion thrusters. When fully developed, the code will be used to analyze and design three-grid ion thrusters, which can be tailored to reduce erosion significantly below the levels of erosion observed in an older generation of two-grid ion thrusters. The code runs on PC-compatible computers and provides real-time color graphical displays that facilitate analysis and interpretation of the simulated physical phenomena as computation progresses.

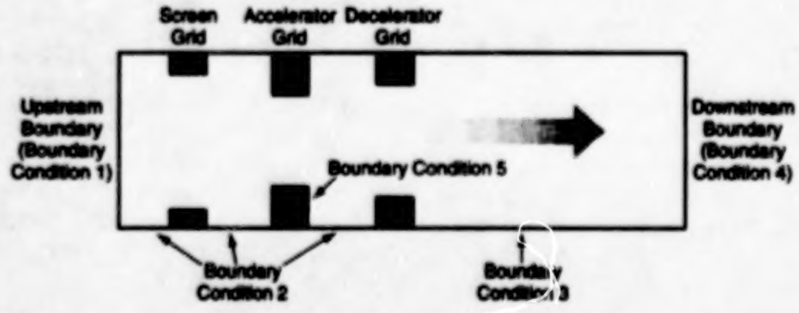

The Computational Domain for the DSMC calculation is a cylinder, with various boundary conditions at various positions on the upstream and downstream ends, the grids, and the side wall.

The grids in an ion thruster are eroded by sputtering from charge-exchange ions produced by collisions between the primary beam ions (the ions that one seeks to accelerate) and neutral atoms. The neutral atoms come from both neutral propellant gas escaping from a plasma-discharge chamber in the thruster and from residual gas in the vacuum chamber in which the thruster is tested or operated. The computer code, which simulates these and other phenomena relevant to the grid-erosion problem, is an extended version of software that was originally developed for two-grid thrusters.

Because of the low density and the small rate of charge-exchange collisions in ion thrusters, one can use direct motion-of-particles numerical-simulation methods to model the phenomena in an ion thruster. Accordingly, the computer code incorporates two algorithms that implement particle-oriented mathematical models. One of these algorithms implements a charged-particle model accord-

ing to the particle-in-cell method, in which the trajectories of a large number of particles are tracked to simulate the flow of a plasma or of ions. This model is used to simulate the ion beam and ion optics and is coupled with a Monte Carlo model for simulation of the charge-exchange collisions. The other algorithm simulates the flow of neutral atoms from both sources by use of the direct-simulation Monte Carlo (DSMC) method.

In the charged-particle/particle-in-cell algorithm, each simulation particle carries a representative electric charge and is located in one of the cells of a computational grid. The principal advantage of the particle-in-cell method is that it is based on first principles, with few approximations or *ad hoc* assumptions. The motion of each particle is computed directly from Newton's equations and the equation for Lorentz force. Self-consistent electric and magnetic fields for use in computing the Lorentz forces are computed by use of Maxwell's equations for the electric and magnetic fields generated in part by the motions of the particles themselves. Sputtering is calculated when the particle-in-cell model indicates that a particle strikes a grid.

In the Monte Carlo model for charge-exchange collisions, the time of free flight of a particle between collisions is chosen from a random distribution of such times in a simplified, approximate mathematical model of a relative-velocity-dependent collision frequency. A choice is then made from another random distribution to determine whether a given collision causes charge exchange. In the event of charge exchange, the velocity of the newly created ion is chosen from a random thermal distribution, and thereafter the ion is accelerated according to the charged-particle model.

In the DSMC method used to simulate the flows of neutral gas, the motions of thousands of neutral atoms or molecules are tracked. In this method, one assumes that the gas is so rarefied that the mean free path for collisions between neutral atoms or molecules is much larger than the accelerator grid structure. Thus, collisions between neutral atoms and molecules can be neglected, and the only collisions that must be considered are those between these neutral particles and the grids.

The particles that represent the neutral propellant gas escaping from the discharge chamber are introduced into the computational domain with Maxwellian distributions of velocity at an upstream boundary, as indicated by boundary condition 1 in the figure. Whenever a particle strikes a grid surface (boundary condition 5), the particle is assumed to be completely accommodated, and the velocity with which it leaves the grid is chosen from a Maxwellian distribution at the temperature of the grid. Whenever a particle reaches the outer cylindrical surface of the computational domain upstream of the last downstream grid surface (boundary condition 2), it is reflected back into the computational domain; this simulates the entry of particles from the surrounding region. When a particle reaches the far downstream limit of the computational domain (boundary condition 4) or the cylindrical surface downstream of the last grid surface (boundary condition 3), that particle is removed from the computation. The computation continues until a steady state is achieved.

The flow into the grid structure from the residual gas in the vacuum chamber is calculated similarly, except that the boundary conditions are different. The calculation of this flow serves to validate the DSMC algorithm, inasmuch as the density of neutral atoms or molecules in the steady state must become approximately uniform at the density of the residual gas in the vacuum chamber. The densities of neutral atoms or molecules obtained from the two Monte Carlo calculations are summed, and the sum is used as the neutral-particle density for the charge-exchange and sputtering calculations.

Predictions made by this computer code were compared with measurements taken in experiments on ion thrusters with several different three-grid configurations. The code predicted the differences among the purveyances of these configurations. It predicted the insensitivity of the current impinging on the accelerator grid to the pressure of the residual gas, but predicted too small a value for this current. The code also predicted the dependence of the decelerator-grid current on pressure and the fact that significant erosion can be caused by ions extracted from a weakly ionized downstream plasma.

This work was done by Quan Zhang, Xiaohang Peng, and Dennis Keefer of ERC, Inc., for **NASA's Jet Propulsion Laboratory**. *Further information is contained in a TSP [see page 1].*
NPO-30017

Galvanic Cell for Measuring Rates of Corrosion

A galvanic cell can serve as a simple apparatus for measuring rates of galvanic corrosion of dissimilar metals. Such a cell can be constructed by filling a glass beaker with an electrolyte like that encountered in the corrosive environment, (e.g., 0.1 M NaCl representing a coastal environment), partly immersing coupons of the two dissimilar metals in the solution, attaching wires to the dry parts of the coupons, and connecting the free ends of the wires to the terminals of an ammeter. The galvanic current indicated by the ammeter is directly related to the rate of corrosion.

This work was done by S. Rachel Khoshbin, John R. Emmons, and Martin W. Kendig of Boeing North American, Inc., for **Marshall Space Flight Center**. *Further information is contained in a TSP [see page 1].*
MFS-30103

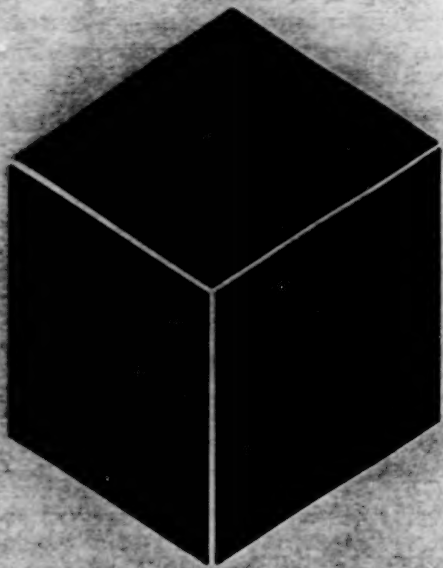

Materials

Hardware, Techniques, and Processes

Books and Reports

BLANK PAGE

Growing Small-Diameter, Single-Crystal Oxide Fibers

$Y_3Al_5O_{12}$ fibers may be useful as high-temperature reinforcements in composite materials.

Lewis Research Center, Cleveland, Ohio

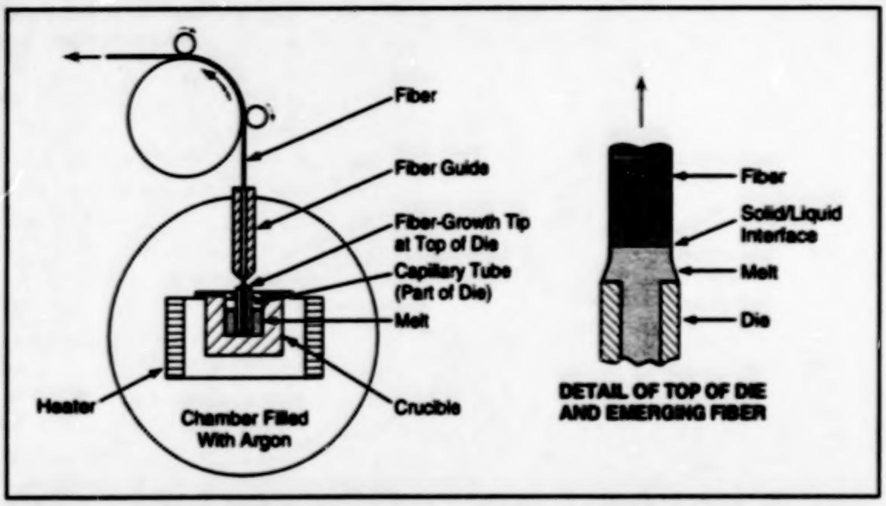

Figure 1. In the Basic EFG Process, a single-crystal fiber is pulled from a melt. The diameter of the fiber is governed by the outer diameter of the die, the top of which is wetted by the molten fiber material.

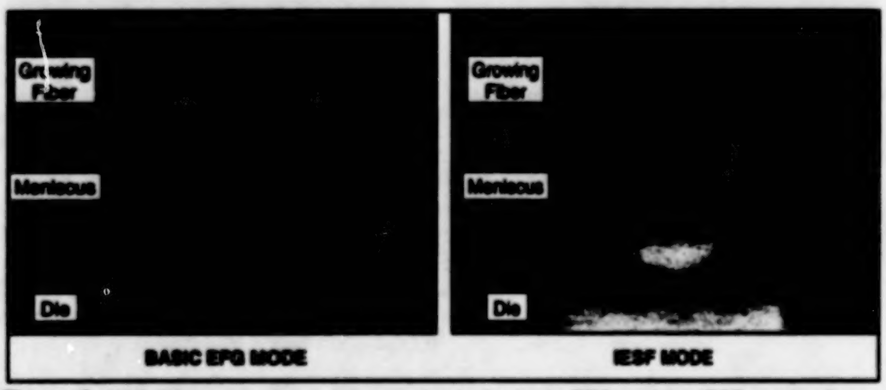

Figure 2. YAG Fibers are shown here growing in the basic EFG and the IESF modes from a die with an outer diameter of 250 µm and an inner diameter of 75 µm. In the IESF mode, the melt retracts to the orifice, so that the diameter of the growing fiber is governed by the inner diameter of the die.

Small-diameter, single-crystal fibers of $Y_3Al_5O_{12}$ (yttrium aluminum garnet, often abbreviated as "YAG") have been grown in an improved edge-defined, film-fed (EFG) growth process. YAG and other yttria alumina compounds have been considered for use in metal- and ceramic-matrix composite materials; because YAG resists creep at high temperatures, YAG fibers may be useful as high-temperature reinforcements of ceramic matrices.

Figure 1 illustrates the basic EFG process. A fiber is grown by cooling and thereby solidifying molten fiber material while pulling the material (in this case, molten sapphire) upward from the horizontal annular top surface of a vertical cylindrical die. Normally, the molten material wets the top of the die, and the outer diameter of the die and the fiber grows slightly narrower than this diameter. The molten material flows from a crucible below, through a capillary passage in the die to the orifice at the top of the die.

The surfaces of the top of the die and the capillary passage are made from a material that is compatible with the liquid and solid phases of the fiber material and is wetted by the molten fiber material. The capillary passage is extended into the molten material in the crucible and is dimensioned so that surface tension in the molten material is sufficient to provide the capillary action needed to feed the molten material to the top of the die.

Growth is started by causing the molten material on top of the die to solidify on a seed fiber, then starting to pull the seed fiber upward at a speed consistent with the rate at which molten material can be supplied to maintain the film and/or the rate at which heat liberated by solidification can be rejected. Proper adjustment of the temperature of the melt and the pulling speed makes it possible to grow a crystalline fiber continuously.

The present EFG process incorporates two improvements (see Figure 2). One of the improvements is a combination of (1) an increase in the pulling speed and (2) modification of the top surface of the die to decrease the tendency toward wetting. These changes affect the balance of hydrostatic and capillary forces in such a way as to enable growth to occur in the inside-edge-defined, self-filling (IESF) mode, in which the melt retracts to the orifice and the diameter of the fiber is governed by the inside edge of the die instead of the outside edge as before (see Figure 2). IESF growth is started in the same way as before, but as the pulling speed is increased, the shape of the meniscus changes and at a critical speed, the melt suddenly narrows to the diameter of the orifice. The advantage of IESF mode is that small-diameter fibers can be grown more easily while still using wide, robust dies.

The other improvement lies in the design of guides to help maintain the desired crystallographic orientation of the fiber, and to keep the fiber straight and centered on the centerline of the die. Traditionally, a rigid guide has been mounted on the furnace above the die. Given thermal expansion of the die and dimensional tolerances of mating parts, it is difficult to maintain the necessary precise orientation of the guide with respect to the die. In addition, if the guide fits too tightly about the growing fiber, such minor defects as small kinks in the fiber can jam at the guide, stopping growth. The improved design combines a precise guide mounted integrally with the die lid and a loosely fitting guide mounted on the furnace in which the crucible is located.

This work was done by Winfield B. Perry and Richard C. Ventura of Advanced Crystal Products Corp. and Ali Sayir of Case Western Reserve University for **Lewis Research Center**. *No further documentation is available.*

Inquiries concerning rights for the commercial use of this invention should be addressed to the Patent Counsel, Lewis Research Center [see page 1]. Refer to LEW-16013.

Si_3N_4-Based Fiber-Coating Material for Ceramic Composites

This material imparts graceful degradation and resistance to high-temperature oxidation.

Lewis Research Center, Cleveland, Ohio

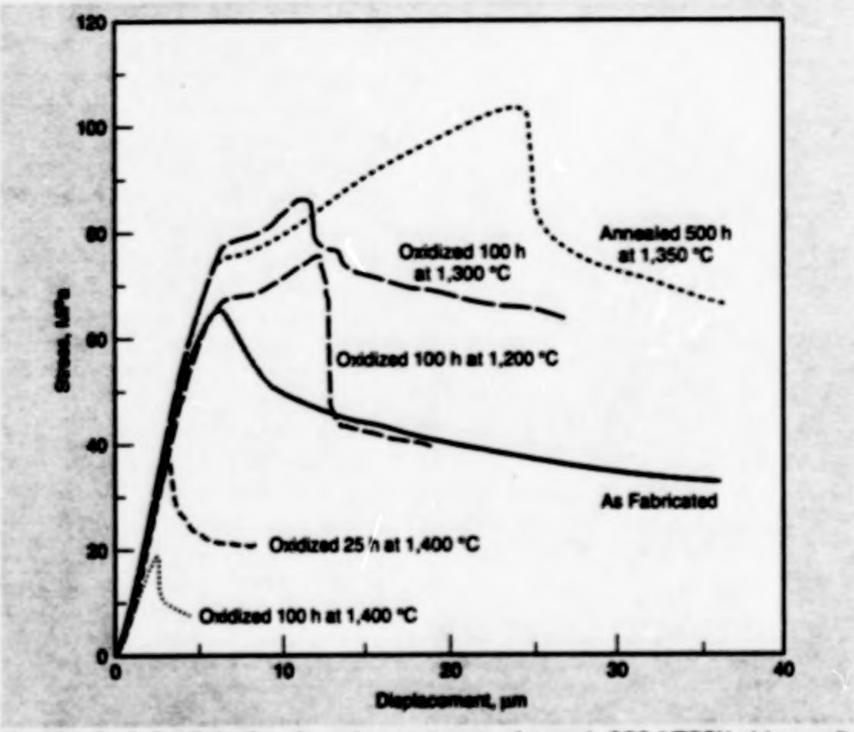

The Fiber-Push-Out Behavior, after various treatments, of a sample SCS-0/RBSN minicomposite with porous interphase is shown.

A Si_3N_4-based coating material and coating process have been developed to provide improved interfacial layers between SiC fibers and the SiC fiber or Si_3N_4-matrix of composite materials. SiC/SiC and SiC/Si_3N_4 composites are candidates for use in high-temperature turbines. Typically, ceramic composites of this type have been made with C- and BN-based fiber-coating materials, which have limited oxidation resistance. Experiments have shown SiC/Si_3N_4 composites made with this improved Si_3N_4-based fiber-coating material exhibit very good (good in terms of the "graceful failure" explained below) interfacial behavior as determined in fiber-push-out tests, in both the as-fabricated condition and after annealing and oxidation exposure.

In the context of a ceramic or other brittle composite material, "graceful failure" denotes a failure mode in which fibers debond from the matrix. This failure mode is desirable for limiting damage. The fiber-coating materials that are incorporated into nonoxide ceramic-matrix composites are weak interfacial materials that are used to promote graceful failure. The C- and BN-based fiber-coating materials mentioned above have not performed well because they become oxidized easily and in a way that can impair the long-term performance of the composites that contain them.

This improved Si_3N_4-based coating material is a silica former; when the interfacial layers are fully formed, they are porous mixtures that consist largely of Si_3N_4 and SiO_2. As a class, silica formers exhibit excellent resistance to oxidation, and are among the most promising candidates to succeed interfacial C and BN. When made with a high volume fraction of suitably dispersed pores, the Si_3N_4-based interfacial layers can perform the interfacial function of limiting damage through diversion of cracks. Porosity reduces the shear strength of brittle solids. Thus, a porous, brittle interfacial material in a ceramic-matrix composite is likely to constitute a preferred path for the diversion of cracks propagating from the matrix; this would promote debonding of fibers and thus graceful failure of the composite.

More specifically, the improved interfacial material contains Si_3N_4 bonded with silica, and with tailored porosity generated by the pyrolysis of organic microspheres. In the fiber-coating process, the precursor mixture destined to become the interfacial material is applied as a slurry coating on SiC fibers. The coating is then consolidated in slow calcination and annealing treatments.

Small composite specimens for use in the experiments were made with reaction-bonded silicon nitride (RBSN) as the matrix material, Textron SCS-0 (chemical-vapor-deposited SiC) as the fiber material, and the improved interfacial coating material. In the fiber-push-out tests, the mean fiber-debonding and sliding stresses of the specimens in the as-fabricated condition were ≈60 and 50 MPa, respectively. This performance can be compared with the current benchmark interfacial performances of (a) a debonding stress of 10 MPa characteristic of a composite that is similar except that the fiber material is SiC with a C-based coating (an SCS-6-fiber/RBSN-matrix composite) and (b) lack of push-out in another composite that is similar except that there is no interfacial material (an SCS-0-fiber/RBSN-matrix composite).

In the specimens containing the porous Si_3N_4/SiO_2 interfacial material, fiber-push-out was still achieved after two severe durability tests involving exposure to high temperatures. In one of these tests, the specimens were subjected to prolonged annealing in N_2 at a temperature of 1,350 °C to induce coarsening of the microstructure and promote bonding of the interfacial material to the fiber and matrix materials through sintering. In the other test, 1.0-mm-thick wafer specimens were oxidized for times from 25 to 100 hours, at temperatures from 1,200 to 1,400 °C. These were intended as accelerated tests to simulate what might happen to the interfacial layers in service.

In unnotched samples of the minicomposite (as-fabricated, annealed, or oxidized) tested to fracture in bending, the crack path was observed to pass through the porous interphase in all cases. In control samples of SCS-0/RBSN and SCS-6/RBSN oxidized for 50 h and similarly tested in bending, fracture included the fiber in places. The results of the fiber push-out tests are shown in the figure. The interfacial performance was not impaired by the high-temperature exposures: the stresses

needed for debonding and sliding remained in the range of 80 ± 20 MPa typically observed for SiC/SiC composites with a BN interphase. Accordingly, the porous Si_3N_4/SiO_2 interphase is considered to resist oxidation, and the composite that contains this interphase is considered to survive oxidation. Efforts to apply this material to small-diameter fibers in tows and weaves are underway.

This work was done by Linus U. J. Thomas-Ogbuji of NYMA, Inc., for **Lewis Research Center**. *No further documentation is available.*

Inquiries concerning rights for the commercial use of this invention should be addressed to the Patent Counsel, Lewis Research Center [see page 1]. Refer to LEW-16261.

Advanced Thermomechanical Fatigue (TMF) Testing of Composites

Degradation of measured elastic properties yields insight into the accumulation of TMF damage.

Lewis Research Center, Cleveland, Ohio

An advanced method for the thermomechanical testing of composite materials can be implemented in conjunction with any conventional or unconventional load-controlled cyclic thermomechanical fatigue (TMF) test (see Figure 1). The method involves the incorporation, into each collected TMF cycle, of measurements of the coefficient of thermal expansion (CTE) and of the isothermal static modulus of elasticity (E). Thus, CTE and E are determined as functions of the cycle number. The evolution of the values of these parameters as the TMF test progresses yields insight into the accumulation of damage within the specimen.

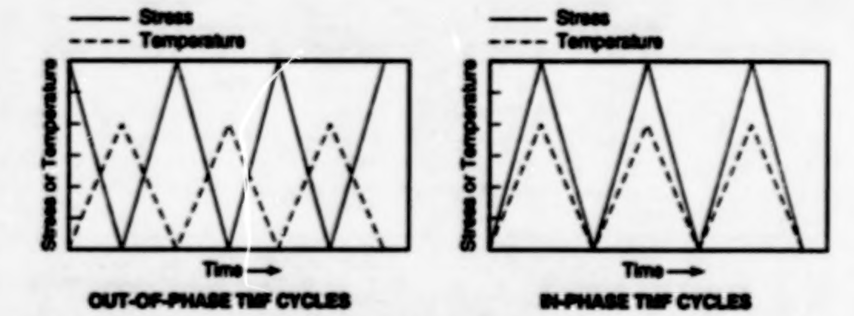

Figure 1. These Thermomechanical Fatigue Cycles are commonly used to test specimens of composite materials under relatively simple controlled conditions.

The measurements of CTE and E are automated. The basic TMF test conditions are altered only slightly. Figure 2 illustrates the method as applied during a typical TMF test with conventional in-phase cycles in which the temperature is cycled between lower and upper limits of T_1 and T_2, respectively, while an applied tensile load is cycled from zero to a specified maximum, in phase with temperature.

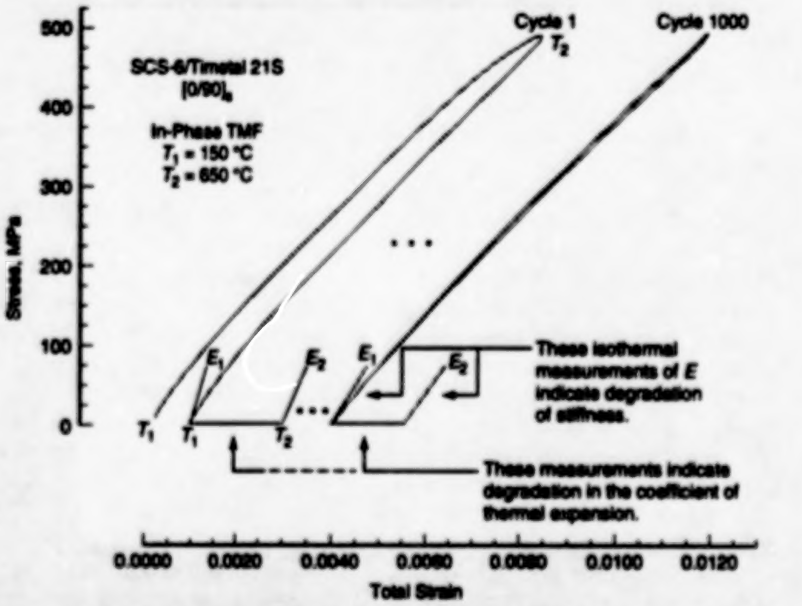

Figure 2. The First and 1,000th Cycles of a TMF Test, with ancillary zero-stress thermal and isothermal tensile cycles show degradation in the E and CTE of a specimen of a titanium-matrix composite material.

After each TMF cycle designated for data collection, the specimen is subjected to a thermal cycle identical to that of the TMF test, but the load is kept at zero. This thermal cycle is represented by the horizontal line from T_1 to T_2. The thermal expansion of the specimen is measured during this thermal cycle by use of a high-temperature extensometer, yielding data on the thermal strain response, by which CTE is calculated.

When the temperature reaches T_2, it is held there for a short time, during which E is measured by applying a small load and measuring the strain; this measurement is indicated by the line marked "E_2." At the end of the thermal cycle, the temperature returns to T_1 and is again stabilized for a short time while a similar measurement of E is performed, as indicated by the line marked "E_1." Then the next full TMF cycle begins. The load applied to measure E should be small enough so as not to introduce additional damage. For further information, see the following article: "An Advanced Test Technique to Quantify Thermomechanical Fatigue Damage Accumulation in Composite Materials," *Journal of Composites Technology and Research*, Vol. 16, No. 4, October 1994, pp. 323 – 328.

This work was done by Michael G. Castelli of Sverdrup Technology, Inc., for **Lewis Research Center**. *No further documentation is available.*

Inquiries concerning rights for the commercial use of this invention should be addressed to the Patent Counsel, Lewis Research Center [see page 1]. Refer to LEW-16003.

Lightweight, Thermally Insulating Structural Panels

Aerogels and radiation-control films reduce heat transfer to unprecedented low levels.

NASA's Jet Propulsion Laboratory, Pasadena, California

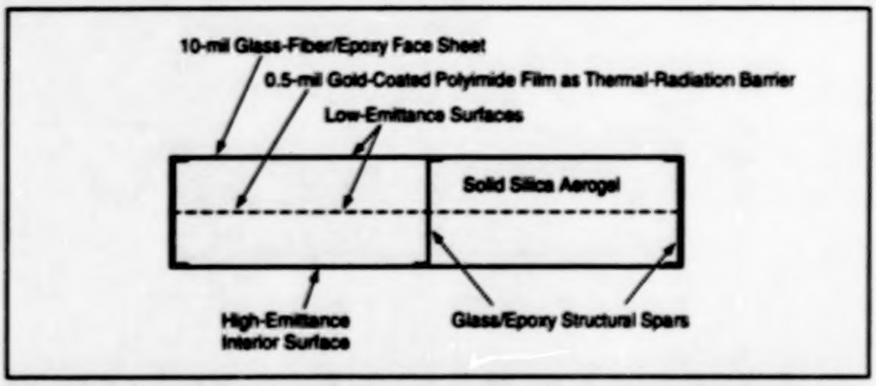

Spaces in Columns formed by spars and sheets are filled with a low-density, high-thermal-resistivity solid silica aerogel. Gold films at the outer surfaces, midplane, and inner surface reduce the radiative transfer of heat.

Condition	Temperature (°C)	Thermal Conductivity (W/m-K)
1 atm	25	0.0333
10 torr CO_2	−79	0.0089
10 torr CO_2	−27	0.0126
10 torr CO_2	25	0.0163
1.2×10^{-3} torr Nitrogen	−78	0.0049
1.2×10^{-3} torr Nitrogen	−26	0.0074
0.4×10^{-3} torr Nitrogen	25	0.0113

Additional Thermal Conductivity Data for the structure as a function of pressure and temperature are shown.

Lightweight composite-material structural panels with superior thermal-insulation properties have been developed. These panels feature a sheet-and-spar construction with column (hollow-core) volumes filled with low-density solid silica aerogel (see figure). In comparison with the previous state-of-the-art panels comprising honeycomb cores filled with opacified silica aerogel powder, the present panels have about 50 percent less mass density and 30 percent less thermal conductivity. These panels could be particularly useful as integrated insulating and structural members in high-altitude aircraft, spacecraft, vacuum instruments, and low-pressure-processing equipment.

The spars and sheets are made of glass-fiber-reinforced epoxy. The silica aerogel filling has a mass of 1.25 lb/ft^3 (20 mg/cm^3), is hydrophobic, and exhibits high resistance to mechanical shock. The spatially averaged mass density of an experimental 1-in. (2.54-cm)-thick panel, including the sheets, spars, and insulation, was found to be 4.5 lb/ft^3 (72 mg/cm^3). Inasmuch as most of the mass of a panel comes from the glass-fiber/epoxy face sheets, a thicker panel would have less overall mass density.

The effective thermal conductivity of the experimental panel was found to be 0.033 W/(m-K) at a temperature of 24 °C. By pumping down to a vacuum with a residual pressure of 10^{-3} torr ($\approx 10^{-1}$ Pa), the effective thermal conductivity at 25 °C was made to decrease to only 0.0113 W/(m-K) (see table).

Convective heat transfer in a panel of this type is suppressed by the solid aerogel, the interstitial spacing of the lattice structure of which is orders of magnitude smaller than the mean free path of an air molecule at low atmospheric pressure. Conductive heat transfer is minimized by choosing a glass-fiber/epoxy composite with a low thermal conductivity and by minimizing the cross-sectional areas of spars and sheets. Radiative heat transfer is minimized by placing a low-emissivity film of gold-coated polyimide films on the outer surfaces of face sheets and at the midplane of the panel.

This work was done by Gregory S. Hickey, David F. Braun, Peter Tsou, David K. Brown, William H. Mateer II, and Willis W. Han of Caltech for **NASA's Jet Propulsion Laboratory**. *Further information is contained in a TSP [see page 1].*

In accordance with Public Law 96-517, the contractor has elected to retain title to this invention. Inquiries concerning rights for its commercial use should be addressed to

Larry Gilbert, Director
Technology Transfer
California Institute of Technology
Mail Code 315 - 6
Pasadena, CA 91125
(818) 395-3288

Refer to NPO-19504, volume and number of this NASA Tech Briefs *issue, and the page number.*

Increasing Cryogenic Fracture Toughness of Alloy 2195

A modified aging heat treatment produces a better distribution of strengthening precipitates.

Marshall Space Flight Center, Alabama

A modified aging heat treatment for alloy 2195 has been found to yield greater cryogenic fracture toughness than does the previous aging heat treatment. Alloy 2195 is a strong, lightweight alloy of aluminum with copper, lithium, and small amounts of other metals. Increasing the cryogenic fracture toughness of this alloy could enhance its utility in tanks for holding cryogenic fluids.

Alloy 2195 is commercially available in the form of rolled plates. A rolled plate as supplied by the manufacturer is solution-heat-treated, then stretched by several percent at ambient temperature prior to aging heat treatment. The figure illustrates the differences between the previous and modified aging heat treatments. The previous aging heat treatment is an isothermal one, in which the plate is typically heated for 14 to 18 hours at 300 °F (149 °C).

The disadvantage of the isothermal aging heat treatment is that it does not result in a repeatable and optimum distribution of strengthening precipitates in the alloy microstructure. The precipitates occur preferentially along grain or subgrain boundaries and are distributed nonuniformly throughout the matrix. The results are that fracture toughness is less than it could be with a more nearly uniform distribution, and there are differences among the mechanical properties of plates made from different ingots of the same nominal chemical composition.

The modified aging heat treatment is a multistep, controlled-heating rate process. In one version of this treatment, the temperature of a plate is held at 260 °F (127 °C) for 10 hours, increased at a rate of 1 °F/h (5/9 °C/h) to 275 °F (135 °C), held at 275 °F for 20 hours, increased at a rate of 1 °F/h to 290 °F (143 °C), then held at 290 °F for 25 hours. Another version of this treatment involves the same heating rate and holding temperatures but different holding times. In comparison with the isothermal aging heat treatment, this heat treatment reduces the concentration of precipitates along the grain boundaries and provides an increased and more nearly uniform concentration of precipitates in the matrix. The net results are increased cryogenic fracture toughness, smaller ingot-to-ingot differences in mechanical properties, greater tolerance of ingot-to-ingot differences in chemical composition, and greater tolerance of variations in prior thermomechanical processing.

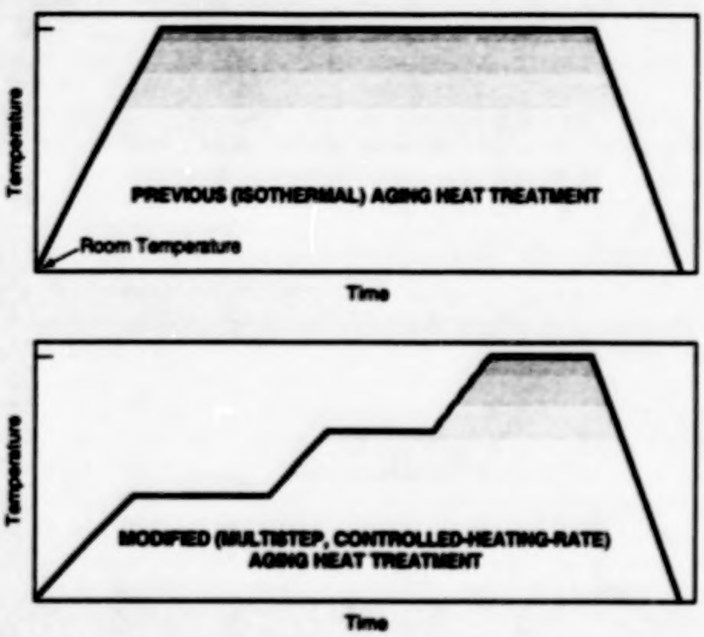

The **Multistep, Controlled-Heating-Rate** aging heat treatment produces a more favorable distribution of strengthening precipitates, resulting in an increase in cryogenic fracture toughness.

This work was done by Tina W. Malone and William P. Stanton of **Marshall Space Flight Center** *and Po-Shou Chen and A. K. Kuruvila of IIT Research Institute.*

Further information is contained in a TSP [see page 1].

Inquiries concerning rights for the commercial use of this invention should be addressed to the Patent Counsel, Marshall Space Flight Center [see page 1]. Refer to MFS-26359.

Protective Coatings for Gamma Titanium Aluminides

These coatings could be used to make lightweight components for turbine engines.

Lewis Research Center, Cleveland, Ohio

Coating alloys of general composition Ti/Al/X (where X denotes Cr, Fe, or another suitable metal) have been developed recently to protect gamma titanium aluminide (γ-TiAl)-based alloys. At half the density of superalloys, γ-TiAl-based alloys are promising candidate materials for use at temperatures between 600 and 850 °C in turbine engines. Replacement of superalloys by γ-TiAl-based alloys would increase thrust-to-weight ratios in the engines and reduce the costs of operating them. However, protective coatings are needed because bare γ-TiAl-based alloys do not resist oxidation adequately and are potentially susceptible to embrittlement by oxygen and nitrogen; this is especially true at temperatures above 750 to 850 °C.

Aluminizing treatments, conventional MCrAlY (M = Ni or Fe) coating alloys, and ceramic coatings for γ-TiAl-based alloys have not proven successful because of

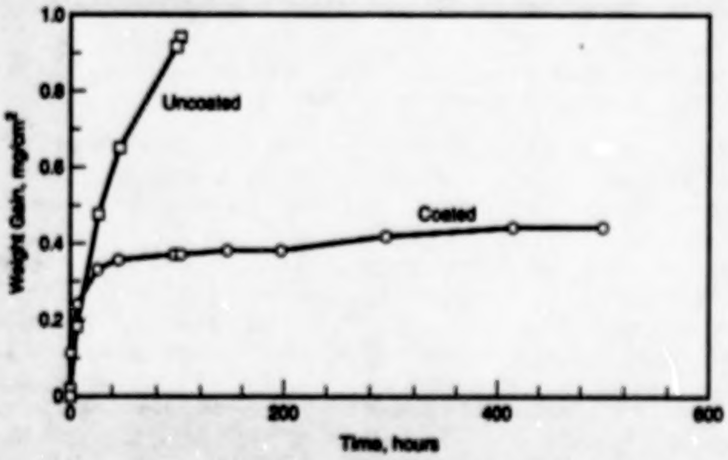

These **Plots of Weight Gains** show data from an experiment on uncoated and Ti/51.25Al/12.25Cr-coated Ti/48Al/2Cr/2Nb substrates in air at a temperature of 800 °C in a furnace. At each data point, the specimen was cooled in air to room temperature, weighed, and returned to the furnace. The data indicate that the coating protected the substrate from oxidation.

poor mechanical properties, mismatch of thermal expansion coefficients, or chemical incompatibility. Promising coating alloys have previously been identified in the Ti/Al/Cr system: These alloys exhibit excellent resistance to oxidation and are generally compatible with the γ substrate alloys. However prior to the development of the present Ti/Al/Cr alloy, the alloys in this system had been found to be extremely brittle.

A Ti/Cr/Al coating alloy developed at NASA Lewis exhibits excellent compatibility with substrates and some improvement in mechanical properties, without sacrifice of resistance to oxidation. The alloy composition, Ti/51.25Al/12.25Cr (the numbers indicate atomic percentages), was selected so that the microstructure consists of the γ phase with a minor volume of the oxidation-resistant Laves phase $Ti(Cr,Al)_2$. By basing the coating alloy on the γ phase, one optimizes mechanical properties and compatibility with γ substrates. The volume fraction of the Laves phase is kept to a minimum because it is extremely brittle.

The Ti/51.25Al/12.25Cr coating alloy was applied to a substrate of the γ alloy Ti/48Al/2Cr/2Nb by low-pressure plasma spraying. Oxidation tests at temperatures of 800 and 1,000 °C in air indicated that the coating alloy successfully protected the substrate from oxidation (see figure). Evaluation of the isothermal fatigue behavior of the coated substrate at high temperatures in air is in progress.

The fundamental studies that led to the development of the Ti/51.25Al/12.25Cr alloy also provided a basis for the selection of new oxidation-resistant Ti/Al/X alloys. One such alloy is Ti/53Al/11Fe. This alloy is potentially useful as a reaction barrier between conventional FeCrAlY oxidation-resistant coatings and γ-TiAl-based substrates. FeCrAlY coatings are not chemically compatible with titanium aluminides, and form brittle reaction products. The Ti/53Al/11Fe alloy would be an excellent reaction barrier because its Fe content is intermediate between the Fe contents of the coating and substrate, and because it resists oxidation.

This work was done by Michael P. Brady of the National Research Council and James L. Smialek and William J. Brindley of **Lewis Research Center**. *Further information is contained in a TSP [see page 1].*

Inquiries concerning rights for the commercial use of this invention should be addressed to the Patent Counsel, Lewis Research Center [see page 1]. Refer to LEW-20003.

Microwave-Induced Combustion Synthesis of Ceramic/Metal Composites

Heating proceeds from the inside out rather than from the outside in.

NASA's Jet Propulsion Laboratory, Pasadena, California

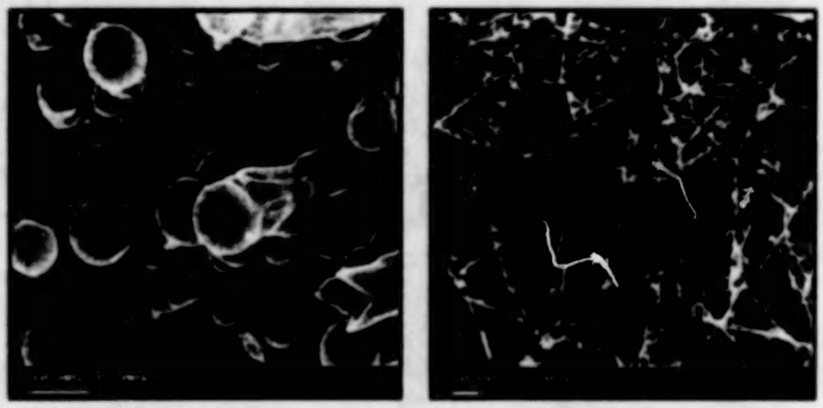

These Scanning Electron Micrographs of uniaxially pressed samples show different whisker microstructures, suggesting different formation mechanisms.

Microwave-induced combustion synthesis has shown promise as a technique for making improved ceramics and ceramic/metal composites. Combustion synthesis is also called self-propagating high-temperature synthesis (SHS) because it involves exothermic reactions that, once started, sustain themselves and propagate through the mixture that is the precursor of the material to be synthesized. SHS offers an attractive, energy-efficient approach to the synthesis of high-temperature composite materials and metastable phases. Microwave-induced combustion synthesis provides advantages over older techniques of SHS, as explained below.

Heretofore in SHS, it has been common practice to ignite the exothermic reactions at the surfaces of the samples of precursor mixtures by use of thermal radiation. In a given case, the thermal radiation can be delivered via a laser beam or from a heating coil placed close to the surface of the sample. Alternatively, the entire sample can be heated to the ignition temperature in an isothermal furnace. The common feature of these ignition techniques is that they produce gradients of temperature in the samples; the surfaces being always hotter than the center.

Microwave-induced combustion synthesis is suitable for cases in which the precursor materials have little or no electrical conductivity. The microwaves penetrate a sample of such a material, delivering heat to the interior. The interior heating results in a temperature gradient that, qualitatively, is the reverse of the gradient produced by thermal radiation. Thus, the combustion front propagates radially outward from the center of the sample. The microstructure of the product material can be completely different from that of the product material obtained in SHS induced by exterior heating. The interior heating in microwave-induced combustion synthesis can also lead to a more complete conversion of reactants from the precursor mixture.

An experimental study was conducted to demonstrate microwave-induced combustion synthesis and to compare it with conventional SHS, using the model reaction $3TiO_2 + 3C + (4 + x)Al \rightarrow 3TiC + 2Al_2O_3 + xAl$. In some experiments, the precursor material contained no excess aluminum ($x = 0$); in others, there was excess aluminum ($x = 4$). (In a production scenario, one would incorporate excess aluminum if one desired to achieve a denser composite product by allowing the molten aluminum generated in the exothermic reaction to infiltrate the pores of the ceramic matrix of the product. The ductile aluminum offers the potential for toughening of the otherwise brittle composite material.)

In the experiments, various samples were subjected, to slow and fast heating by

external and microwave techniques, and some of the samples were uniaxially pressed at levels from 200 to 1,400 psi (1.4 to 9.7 MPa). In all the cases of slow heating, the reactions were incomplete; that is, the precursor materials were not converted completely to the composite product. For $x = 4$, solid Al_2O_3 whiskers were observed in the microwave-heated samples, whereas hollow Al_2O_3 whiskers with bulbous heads were observed in the conventionally heated samples (see figure). The $x = 0$ samples processed with fast and slow microwave heating reached higher densities than did the conventionally heated samples.

This work was done by Martin B. Barmatz and Tzu-Yuan Yin of Caltech for **NASA's Jet Propulsion Laboratory**. *Further information is contained in a TSP [see page 1].*

In accordance with Public Law 96-517, the contractor has elected to retain title to this invention. Inquiries concerning rights for its commercial use should be addressed to

Larry Gilbert, Director
Technology Transfer
California Institute of Technology
Mail Code 315 - 6
Pasadena, CA 91125
(818) 395-3288

Refer to NPO-19637, volume and number of this NASA Tech Briefs *issue, and the page number.*

Copper/Graphite Composites Made With Metal Carbide Coatings

Better composites can be produced at lower cost.

Lewis Research Center, Cleveland, Ohio

A novel method of mass-producing copper-matrix/graphite-fiber composite materials involves coating the fibers with suitable metal carbides, then infiltrating fiber preforms with molten copper. The copper/graphite composites produced by this method are superior to those made by older methods, and the cost of production is lower.

Copper/graphite composites are well-suited for use in advanced thermal-management applications (e.g., heat-sinking structural supports for microelectronic circuits). When a copper/graphite composite is made with high-thermal-conductivity graphite fibers, its thermal conductivity can exceed that of pure copper. Copper/graphite composites also offer lower densities and greater stiffnesses, relative to pure copper. Yet another advantage of copper/graphite composites arises from the negative coefficients of thermal expansion of graphite fibers; by adjusting the proportions of copper and graphite and the distributions of graphite fibers, one can tailor the thermal expansions of the composites to match those of other materials.

Heretofore, it has been difficult to produce copper/graphite composites because graphite is not wet by molten copper. Some prior methods involve the addition of alloying agents to copper or coating the fibers with metal-based alloys or compounds to enhance wetting, but these methods introduce undesirable effects; for example, some cause reductions in thermal conductivity, while others cause chemical reactions that degrade the fibers.

Other prior methods involve, variously, high-pressure infiltration of molten copper into fiber preforms or hot pressing of copper-coated fibers into consolidated forms to overcome the surface-tension forces that prevent wetting. The composites made by these high-pressure methods tend to swell and develop voids when exposed to high temperatures.

In the present method, graphite fibers are coated with metal carbides that are wet by molten metals, including copper. The coating material used in most of the experiments to develop the method was molybdenum carbide, which was chosen because it offers the advantages of low density, low solubility in copper, and relatively low cost.

In a given case, the carbide, or else a metal or other layer that is a precursor to the carbide, can be deposited on the fibers by any of a number of processes; for example, sputtering, chemical vapor deposition, or electrodeposition from a molten salt. The precursor can then be reacted on or with the fiber surfaces to produce the carbide coats. For example, molybdenum metal can be deposited on the surfaces of the fibers by chemical vapor deposition, then reacted with the underlying fibers in a heat treatment to obtain molybdenum carbide coats.

A preform made of coated fibers can be made into a copper-matrix composite by immersing it in molten copper. Because the coating material is wettable, the preform becomes spontaneously infiltrated with the molten copper, without need for high applied pressure. As a result, copper/graphite composites can be mass-produced by relatively simple casting techniques; the cost and complexity of production by this method are reduced, relative to older high-pressure methods that involve such techniques as pressure casting, squeeze casting, hot pressing, and hot isostatic pressing.

Unlike copper/graphite composites made by older methods, the composites made by the present method exhibit no degradation of mechanical, electrical, or thermal properties after prolonged exposure to high temperatures or to thermal cycling. No dimensional hysteresis is observed during thermal cycling. Moreover, the composites made by the present method can be remelted and recast without detrimental effects.

This work was done by Joseph K. Weeks, Jr., Jared L. Sommer, and Todd E. Jarman of Technical Research Associates, Inc., for **Lewis Research Center**. *Further information is contained in a TSP [see page 1].*

Inquiries concerning rights for the commercial use of this invention should be addressed to NASA Lewis Research Center, Commercial Technology Office, Attn: Tech Brief Patent Status, Mail Stop 7–3, 21000 Brookpark Road, Cleveland, Ohio 44135. Refer to LEW-16103.

Books and Reports

Analysis of the Defect Structure of B2 FeAl Alloys

A report presents a study of the defect structure of the B2 phase of FeAl alloys. In the study, the BFS method was used to analyze the defect structure of FeAl from the perspective of energy considerations at zero absolute temperature. The BFS method is based on the idea that the energy of formation of an alloy can be calculated as a superposition of contributions from individual nonequivalent atoms in the alloy. BFS calculations were performed on a large number of candidate ordered structures to determine the configurations of lowest energy and to search for states that could be metastable.

Overall, the results of the calculation were found to provide a description of the defect structure consistent with available experimental data: For example, the calculations were successful in determining the phase field of the B2 structure; the results were consistent with experimental observations that the B2 phase is stable at aluminum contents up to about 52 atomic percent. The results were also in qualitative agreement with experimental observations that the lattice parameter increases with aluminum content.

This work was done by John Ferrante and Ronald D. Noebe of **Lewis Research Center**, *Guillermo Bozzolo of Analex Corp., and Carlos Amador of Universidad National Autónoma de México. To obtain a copy of the report, "Analysis of the Defect Structure of B2 FeAl Alloys," see TSP's [page 1].*

Inquiries concerning rights for the commercial use of this invention should be addressed to NASA Lewis Research Center, Commercial Technology Office, Attn: Tech Brief Patent Status, Mail Stop 7-3, 21000 Brookpark Road, Cleveland, Ohio 44135. Refer to LEW-16426.

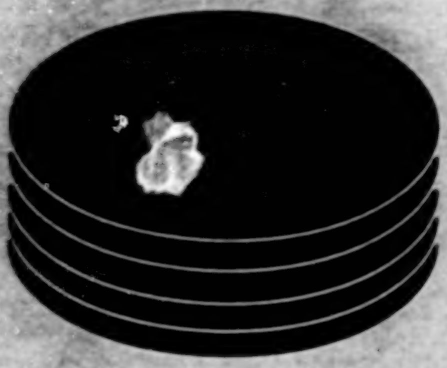

Computer Programs

BLANK PAGE

Computer Programs

These programs may be obtained from COSMIC. Please contact

COSMIC®
Computer Services Annex
University of Georgia
Athens, GA 30602
Telephone No. (404) 542-3265.

Materials

CEMCAN — Ceramic Matrix Composites Analyzer

Behavior can be analyzed from the constituent level to the ply level.

CEMCAN (CEramic Matrix Composites ANalyzer) is a computer program that was developed for analyzing fiber-reinforced ceramic-matrix composite materials. CEMCAN incorporates micromechanics, macromechanics, and laminate theories to enable a comprehensive point analysis of the behavior of a composite material.

CEMCAN uses a novel fiber substructuring technique that enables more accurate micromechanical representation of interfacial conditions, and at the same time provides a higher degree of detail of microstresses at a very high computational efficiency. One can evaluate the effects of interfacial conditions, fiber/matrix breakage, fabrication parameters, degradation of material performance due to environment, and other effects at a laminate level. CEMCAN also provides stress/strain relations up to failure, accounting for redistribution of stresses as matrices in these composites are brittle and start cracking at relatively low stress levels. Such a comprehensive capability from the constituent level to the laminate level does not exist in another computer code for brittle-matrix composites.

CEMCAN is written in FORTRAN 77 for Sun4-series computers running Solaris 2.x. A sample executable code is included on the distribution medium. COSMIC has successfully converted the FORTRAN 77 code to C language by use of the utility program f2c and has tested the code on a Zenith Z-station VP computer with a Pentium 75 central processing unit running Linux 1.3.71 using gcc v2.7.0 and libc v5.0.9. A math coprocessor is required to run CEMCAN under Linux. The binaries and library files for f2c are available to the public. Details are available from COSMIC. The standard distribution medium for CEMCAN is a 0.25-in. (6.35-mm) streaming-magnetic-tape cartridge (Sun QIC-24) in UNIX tar format. Alternate distribution media are available upon request. This version of CEMCAN was released to COSMIC in 1996.

This program was written by P. Murthy, and C. Chamis of ***Lewis Research Center*** *and S. K. Mital of University of Toledo. Further information is contained in a TSP [see page 1].*
LEW-16327

Mechanics

Software for Efficient Packing of Cargo

Positions, weights, and centers of gravity of packed items are taken into account.

The Stowage Tactics for User Flights (STUF) computer program enables space-station users to develop schemes for efficient packing of their cargo. Users determine which trays to use and where those trays are located in a stowage rack. Locations of cargo items in a tray can be determined by computer, or a user can place items as desired. The weight and center of gravity of each item are monitored. Any out-of-bounds condition for a packed tray or rack is highlighted for corrective action. STUF can also combine many users' packing schemes into one cargo manifest; this enables a NASA Center to integrate all user stowage for a space-station mission.

After a file representing user cargo data is read by STUF, cargo is tentatively assigned to a stowage tray and checked for interference with items already assigned to the tray. Any items that do not fit the current tray are assigned to subsequent trays, if possible. Once all trays are loaded, the user determines the location of each tray in a space-station rack. The analytical results returned by STUF become inputs to a broader space-station cargo manifest.

The user interface for STUF is primarily menu-driven. STUF provides two operational modes for tray packing: automatic and interactive. The interactive mode is the quickest to use when packing hundreds of items, and it results in the best packing efficiency. The automatic mode enables the computer to determine where each cargo item is to be placed. A single tray size selected by the user is then used repeatedly for all trays.

Once a set of trays has been packed, the user may wish to place those trays into space-station racks. Stowage racks contain locker assemblies specifically designed to hold certain tray sizes. Although STUF allows a user to determine where a tray is located within the rack, STUF will not place the tray there if the location cannot accommodate it. If a tray-packing solution is later edited, STUF automatically updates mass properties for the rack that contains that tray.

STUF can accommodate 9,999,999 cargo items, 999 trays, and 99 racks per packing operation. Packing foam must be accounted for as part of each cargo item. STUF does not add the properties of foam to the mass properties of any item.

STUF is written to run with DesignCAD 3-D and is available only as object code for IBM PC-compatible computers. It has been successfully implemented on a 486 DX2 computer under MS-DOS 5.0. STUF requires DesignCAD 3-D v4.0, 640K of random-access memory, a graphics display, and a hard disk drive. A printer is highly desirable for capturing STUF output. The standard distribution medium for STUF is one 3.5-in. (8.89-cm), 1.44MB, MS-DOS-format diskette. An electronic copy of the documentation in ASCII format is included on the distribution medium. STUF was released to COSMIC in 1996 and is a copyrighted work with all copyright vested in NASA.

This program was written by Vance Houston of ***Marshall Space Flight Center****. Further information is contained in a TSP [see page 1].*
MFS-31101

Mathematics and Information Sciences

Improved 3DGRAPE

Grids of better quality can be generated.

"3DGRAPE/AL" denotes the Three-Dimensional Grids About Anything by Poisson's Equation/The Ames-Langley Technology Update computer program. 3DGRAPE/AL is a significantly improved version of 3DGRAPE, which has been widely distributed and has been described previously in *NASA Tech Briefs*. 3DGRAPE/AL generates volume grids by iteratively solving Poisson's Equation in three dimensions. The terms on the right side of the equation are designed so that user-specified grid-cell heights and user-specified grid-cell skewness near boundary surfaces are obtained automatically, with little intervention by the user. Versatility was a high priority in the development of this code, and as a result, the code can generate grids in almost any three-dimensional physical domain. 3DGRAPE/AL can be run in batch mode like the original 3DGRAPE, and it offers a graphical user interface (GUI) on Silicon Graphics, Inc. (SGI) computers.

3DGRAPE/AL reads in predefined data, generates a grid, and writes it out. For those boundary surfaces which are of interest ("the body"), it expects to read X,Y,Z coordinates of surface grid points that the user has defined previously by use of other software. Other boundary surfaces of less interest ("the outer boundary") can be found by the program itself, using simple analytic shapes. The grid can consist of multiple blocks, and the program is capable of finding its own internal block-to-block boundary surfaces.

3DGRAPE/AL offers a significant number of features that were not offered by 3DGRAPE. In 3DGRAPE/AL, grid quality is enhanced by reformulated control terms in Poisson's Equation. The user can specify arbitrary angles with which lines are to intersect boundaries; that is, these angles are no longer limited to the single value of 90° everywhere. Better grid quality results from the addition of Thomas & Middlecoff (T&M) clustering terms for cases in which all six faces of a block are read in. The user can choose terms of either the Steger & Sorenson or the T&M type, or a blend between the two types that gives good cell size and skewness control at both boundaries and the interior. Grid quality is evaluated by computing and printing maxima, minima, medians, and averages of cell heights and nonorthogonality, at boundaries and in the interiors of the blocks of the finished grid.

Other features in 3DGRAPE/AL provide for speedier convergence. Initialization is improved by trans-finite interpolation (for cases with six fixed boundary surfaces), which either offers a final grid or speeds convergence. The use of Erlich's *ad hoc* method for computing locally optimum relaxation parameters for a successive-over-relaxation (SOR) solver in the code can also speed convergence. In addition, convergence can be accelerated when the code is vectorized in any of the three coordinate directions (when installed on Cray computers), allowing the longest possible vector length in each block. These features, combined with careful code optimization, result in a speedup over the previous code by approximately a factor of four.

Various other features that assist in the input of data are also offered by 3DGRAPE/AL. These features include two input filters: (1) an input filter that accepts GRIDGEN (ARC-13371) output as input and converts it to 3DGRAPE/AL input and (2) an input filter that reads input designed for the original 3DGRAPE and reformats it for use with 3DGRAPE/AL. For more versatile input, required cell heights and skewness at read-in surfaces can be specified by the user at each point from a file, a complete grid generated elsewhere can be read in, and an elliptic solver in 3DGRAPE/AL can be run a few steps to smooth the grid. More extensive error checking of input data has been implemented, and a GUI (for SGI computers) enables the user to watch selected grid surfaces while the grid solver in 3DGRAPE is iterating. The GUI also enables the user to suspend the iterative process and plot convergence histories.

3DGRAPE/AL is written in FORTRAN 77 for UNIX-based computers. The graphical mode of 3DGRAPE/AL makes use of the Iris Graphics Library (IGL) and is written in FORTRAN 77 for SGI IRIX machines. An ANSI standard FORTRAN compiler is required to build executable codes. Sample input and output are included on the distribution medium. The batch mode of 3DGRAPE/AL has been successfully implemented on the following computers: an SGI Indigo2 running IRIX 5.2, a Sun4 running SunOS 4.1.3, a Sun4 running Solaris 2.4, an IBM RS/6000 running AIX 4, an HP 9000/720 running HP-UX 9.03, and a Cray Y-MP running UNICOS 8.0.3.4. The graphical mode of 3DGRAPE/AL has been successfully implemented on an SGI Indigo2 running IRIX 5.2. The standard distribution medium for 3DGRAPE/AL is a 0.25-in. (6.35-mm) streaming-magnetic-tape cartridge (Sun QIC-24) in UNIX tar format. Alternative distribution media and formats are available upon request. An electronic copy of the documentation in PostScript format is included on the distribution media. 3DGRAPE/AL was released to COSMIC in 1996.

This program was written by Reese L. Sorenson *for* **Ames Research Center**. *Further information is contained in a TSP [see page 1].*
ARC-14069

Mechanics

Hardware, Techniques, and Processes

BLANK PAGE

Screens Would Suppress Flow-Induced Resonances in Cavities

The key is to choose proper spacing of holes. *Ames Research Center, Moffett Field, California*

Aeroacoustic resonances in shallow cavities exposed to subsonic airflows would be suppressed, according to a proposal, by partly screening the cavity apertures with perforated thin metal sheets. (As used here, "shallow cavities" denotes cavities that are longer than they are deep.) It is desirable to suppress flow-induced pressure fluctuations associated with aeroacoustic resonances where they could interfere with equipment mounted in the cavities; such equipment could include heat exchangers, weapons on aircraft, acoustic sensors, sound absorbers, and chemical-analysis instruments, for example.

For a given screened cavity, aeroacoustic resonances occur because of coupling between aerodynamic excitation on the screen and acoustic pressure fluctuations in the cavity. More specifically, aeroacoustic resonances occur because of coupling between (1) oscillations of flow into and out of the cavity, associated with shedding of vortices from the holes (see Figure 1); and (2) pressure fluctuations associated with acoustic resonances of the screened cavity. Indeed, the frequency of shedding of vortices tends to lock to the nearest cavity modal frequency.

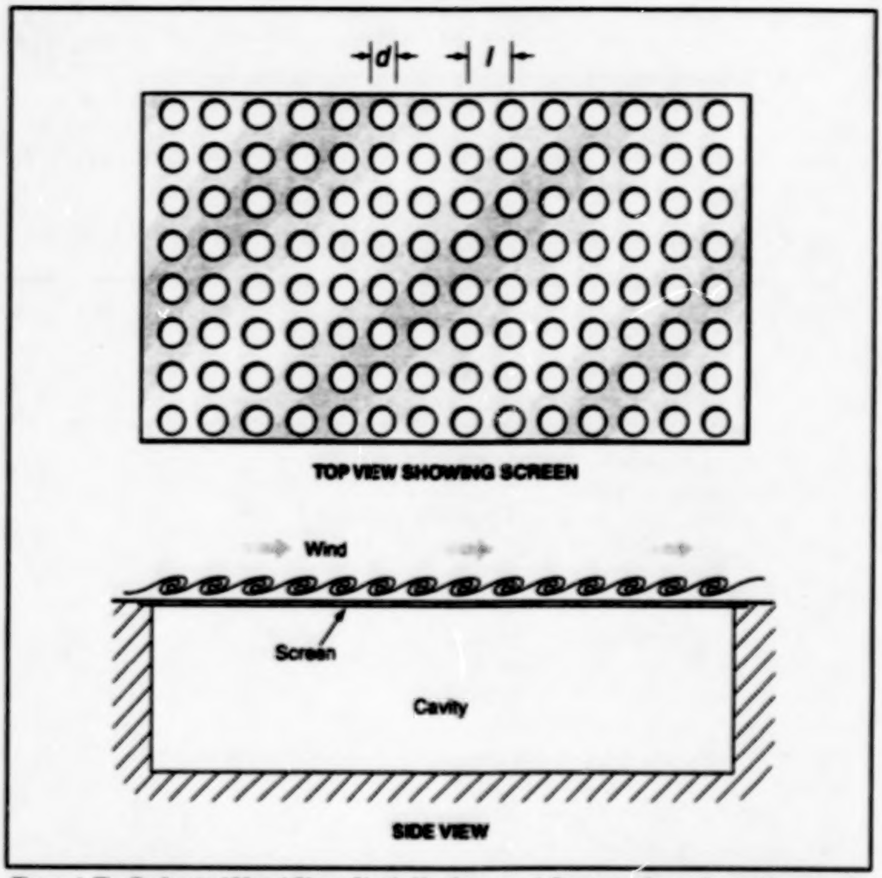

Figure 1. The Perforated Metal Sheet Sheds Vortices as air flows past the cavity, exciting acoustic resonances in the cavity.

The frequency of shedding of vortices is given by $f_V = S_t U_0/d$, where S_t is the Strouhal number, U_0 is the average airspeed, and d is the diameter of a hole. If the diameter is specified in millimeters, then the Strouhal number is given by $S_t = m(0.10d - 0.01)$, where m is a positive integer that corresponds to the harmonic of the fundamental shedding frequency.

The tendency toward the coupling that causes aeroacoustic resonances can be expressed in terms of a phase-coupling parameter given by $\lambda_V/l = U_C/(f_V l)$, where λ_V is the vortex-sheet wavelength (that is, the streamwise distance between vortices), l is the distance between holes, and U_C is the speed of convection of the vortices. Wind-tunnel tests have shown that the aeroacoustic resonances occur when the phase coupling parameter has a value of 1/4, 1/2, or 1.

Substituting the expression for f_V into the equation for the phase coupling parameter, one obtains

$$\lambda_V/l = U_C d/[U_0 l m(0.10d - 0.01)]$$

Thus, the phase coupling parameter depends only on the perforation geometry and on U_C/U_0. In general, U_C/U_0 lies between 0.5 and 0.75, and is probably constant over a wide range of airspeeds. This suggests that it should be possible to choose the perforation geometry (that is, to choose d and l) to set the phase coupling parameter at a value other than 1/4, 1/2, or 1 to suppress aeroacoustic resonances.

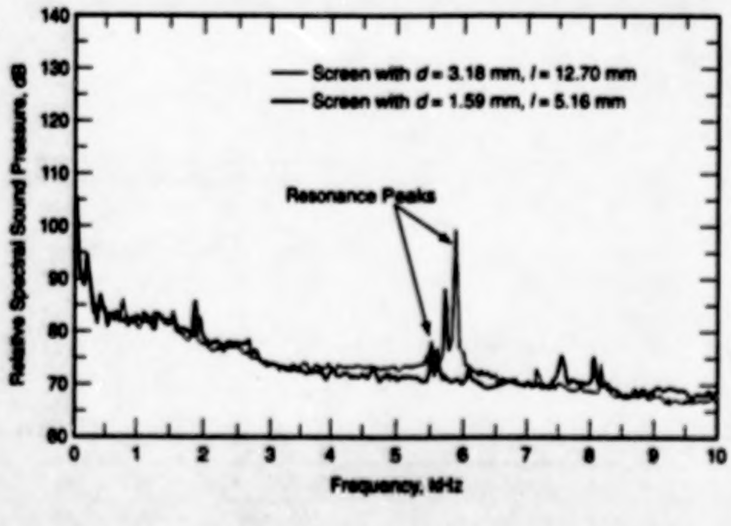

Figure 2. The Peaks in the Spectrum of Sound excited by air flowing past the cavity are reduced sharply by choosing l and d to avoid aeroacoustic resonances.

Practical values of d lie between 1.5 and 3 mm. Preferably, d should be cho-

sen toward the low end of this range; as the holes are made smaller, the flow into and out of the cavity becomes increasingly affected by viscous damping at the edge of the hole, so that resonances become weaker.

Suppose, for example, that one chooses d = 1.59 mm and l = 5.16 mm. This results in U_C/U_0 = 0.58, and the resulting value of the phase coupling parameter is approximately 1.2, 0.6, or 0.4 for m = 1, 2, or 3, respectively. These values differ significantly from the resonance values so that, in principle, the resonances should be suppressed. In an experiment to test this concept, a screen with these dimensions was placed over a cavity 302 mm deep. Another cavity of equal depth was covered with a screen of d = 3.18 mm and l = 12.70 mm to obtain a phase coupling parameter of 0.5, which is a resonance value. The results of the experiment indicated that the resonance was much weaker in the cavity covered by the d = 1.59 mm, l = 5.16 mm screen, as expected.

This work was done by Paul T. Soderman of **Ames Research Center**. *Further information is contained in a TSP [see page 1].*
ARC-13213

Gripper for Testing Composite-Material Tubes

Special preparation of ends of tubes is unnecessary. *Lewis Research Center, Cleveland, Ohio*

A tool has been designed to grip an end of a tubular specimen of composite (matrix/fiber) material for mechanical testing, without crushing or unduly deforming the gripped portion of the specimen. The tool makes it unnecessary to fabricate the ends of specimens to complex shapes for gripping, as has been common practice until now. The tool simplifies and reduces the cost of mechanical tests to measure torsion and tension properties of tubes made of metal-matrix composites for material characterization and for such applications as torsion bars and drive shafts.

The tool (see figure) is essentially a combination of a mandrel and a collet. The mandrel comprises three sectors of a cylinder with a conical inner surface that mates with a conically tapered inner plug. The mandrel is inserted in the tube and, by use of the tapered plug, is expanded gently into contact with the inner surface of the tube.

The collets are installed into a commercially available hydraulic gripping device used in materials testing, and remain there throughout the test program. The tube-and-mandrel assembly is then inserted into the collets, and hydraulic pressure is applied to circumferentially grip the specimen. The test can then proceed.

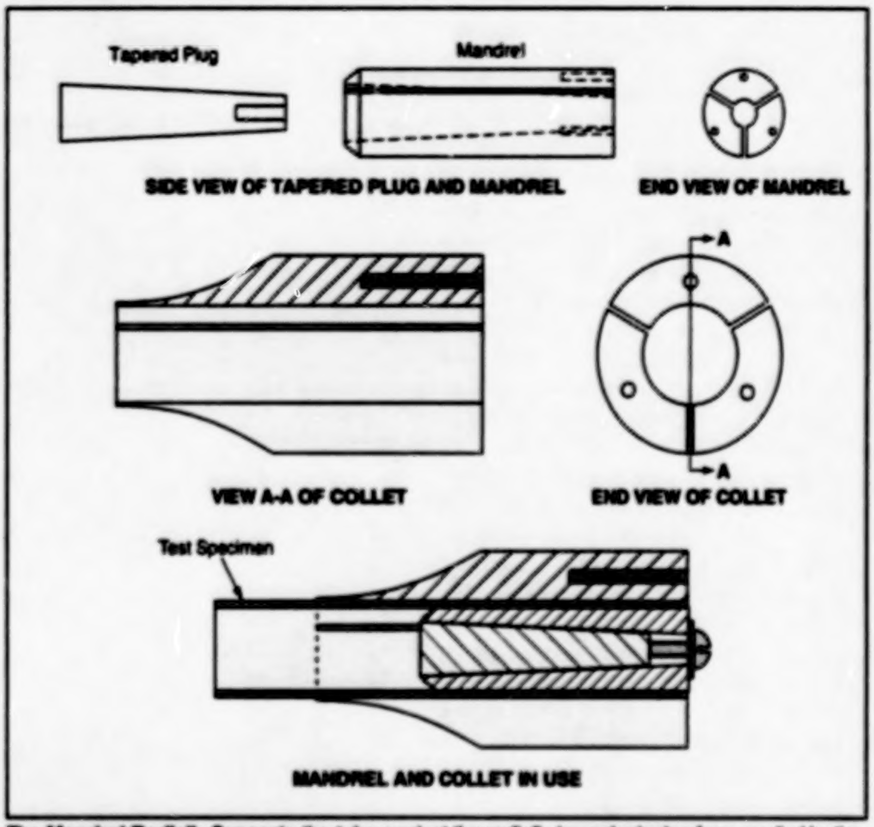

The Mandrel Radially Supports the tube against the radially inward gripping force applied by the collet, thereby preventing crushing of the tube.

This work was done by Christopher S. Burke of NYMA, Inc., for **Lewis Research Center**. *Further information is contained in a TSP [see page 1].*

Inquiries concerning rights for the commercial use of this invention should be addressed to the Patent Counsel, Lewis Research Center [see page 1]. Refer to LEW-16220.

Technique for Calibration of a Shearographic Instrument

Shearograms are taken on a cantilever beam. *Marshall Space Flight Center, Alabama*

A technique for calibration of an optoelectronic shearographic instrument is based on the use of a cantilever beam with a concentrated end load as a standard for elastic deformation of a test object under mechanical stress. Deformations of a test object under mechanical stress can include displacements of surfaces in directions perpendicular to the surfaces. Shearography is a noncontact optical method (explained briefly below) of measuring such displacements along lines of sight approximately perpendicular to the surfaces. A cantilever is particularly suitable as the elastic-deformation standard in the present technique because cantilever beams are commonly used to teach stress-vs.-strain relations to engineering students, and the basic equations for elastic deformation of a cantilever beam are well established.

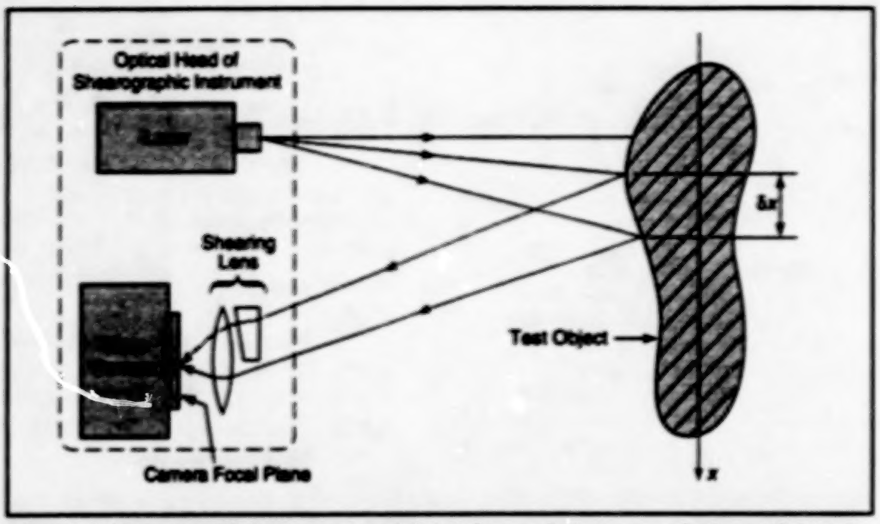

Figure 1. A Shearographic Instrument exploits interference between rays of coherent light arriving at one point on the camera focal plane from two different positions on the test object.

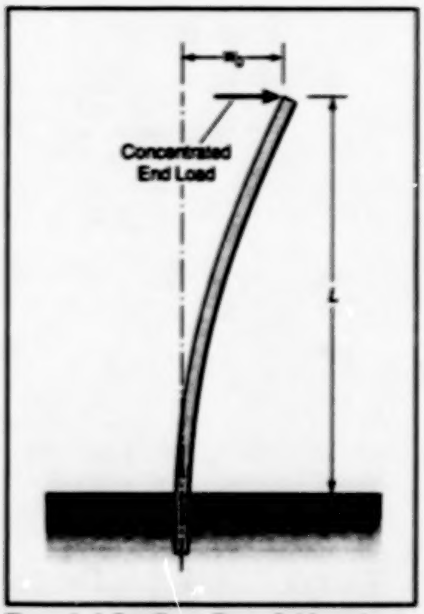

Figure 2. A Cantilever Beam Subjected to a Known Displacement by a concentrated end load serves as the test object in the present calibration technique.

A representative optoelectronic shearographic instrument (see Figure 1) includes a laser and optics that provide an expanded beam of coherent light to illuminate the test object. The instrument also includes a video camera equipped with an image-shearing lens, which is a lens covered partly with a wedge-shaped prism (or with a birefringent plate). The image-shearing lens produces two closely related effects; each point on the test object is imaged at two points on the focal plane of the camera, and each point on the focal plane of the camera receives light from two points on the test object. The distance (δx) between the points on the test object is called the "shear distance" and is easily measurable on the test object.

Shearography is an interferometric method that relies on the second-mentioned effect of the image-shearing lens. The portions of light arriving at a point on the focal plane of the camera from two points separated by δx have two different phases because of the difference between the distances the two portions have traveled from the laser. The phase difference and thus the interference between these two portions depends on the local deviation of the surface of the test object from a nominal constant-phase surface approximately perpendicular to the line of sight. The overall effect is to produce an image containing interference fringes that correspond to contours of the slope of observed surface of the test object. Typically, one records such a shearographic image when the test object is unstressed, then records another image when the object is stressed. From the shift in interference fringes between the stressed and unstressed conditions, one can compute changes in slope and displacement of the observed surface of the test object.

In the present technique, the apparatus is set up to observe the slope and displacement of a cantilever beam (see Figure 2). Shearograms are recorded both with the beam undeflected and with the beam under a concentrated end load to obtain a measured end deflection w_0. The two main equations used in the present technique are derived from the basic equation for shearographic interference and the basic equation for deformation of a cantilever beam under a concentrated end load. The first equation gives the order, n, of the interference fringe at point x along the beam:

$$n = \left(3w_0\delta x / \lambda L^3\right)\left(2Lx - x^2\right)$$

where w_0 is the deflection at the end of the beam, λ is the laser wavelength, and L is the length of the beam. The second equation gives the calibration error, expressed as the fractional difference, ξ, between the observed and predicted values of the slope of the beam at point x:

$$\xi = n\lambda L^3 / 3w_0\delta x\left(2Lx - x^2\right) - 1$$

During a calibration procedure, one determines the position x at which each integer fringe order n occurs on the shearogram, then inserts the values of n and x into the second equation. Thus, a value of fractional error is assigned to each fringe. If the range of slopes to be encountered during subsequent tests is known or can be predicted, then the maximum error observed in that range during calibration can be taken as the maximum error during the subsequent tests.

This work was done by Samuel S. Russell of **Marshall Space Flight Center** *and Matthew D. Lansing and Gary L. Workman of the University of Alabama in Huntsville. Further information is contained in a TSP [see page 1].*
MFS-26364

Liquid-Vaporizing Microthrusters

Liquid propellant would substantially reduce or eliminate containment and leakage problems.

NASA's Jet Propulsion Laboratory, Pasadena, California

A development of liquid-vaporizing microthrusters is proposed for spacecraft with masses of no more than 10 kg. In a typical application, a propellant liquid (e.g., water, ammonia, or hydrazine) would be stored in the liquid phase. When thrust was needed, some of the liquid would be fed to a microthruster, wherein the liquid would be heated, vaporized, and expanded through a nozzle to produce thrust. The microthruster would be micromachined from silicon and would weigh only a few grams. The microthruster assembly would be made to fit on a chip typically 1 cm^2. One of the principal advantages of using a

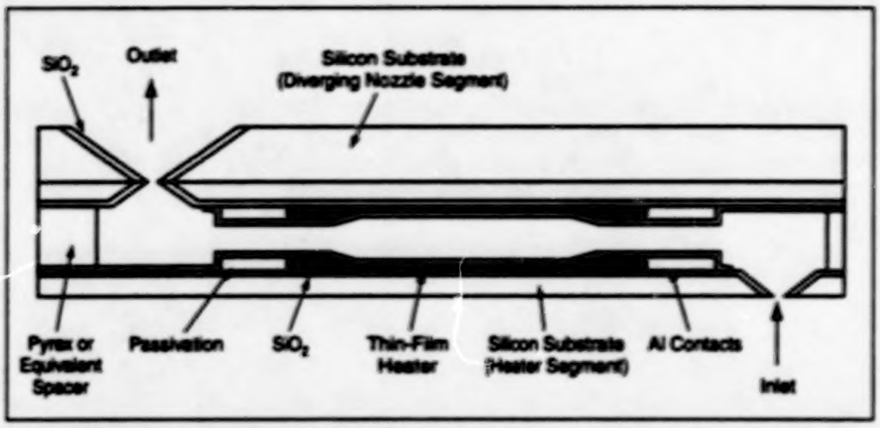

A Liquid-Vaporizing Microthruster Concept would be based on a layered structure using thin-film electrical heaters to vaporize liquid propellants.

liquid propellant (in contradistinction to a gaseous propellant) is that a liquid propellant could be contained much more easily, presenting less of a leakage problem.

A typical microthruster (see figure) would feature a layered structure with silicon dioxide films (for thermal insulation) on silicon substrates, thin-film electrical heaters made of polysilicon, gold electrical contacts, and passivation layers of silicon nitride covering all surfaces in contact with the flow.

This work was done by Juergen Mueller, Stephanie Leifer, Lilac Muller, and Thomas George of Caltech for **NASA's Jet Propulsion Laboratory**. *Further information is contained in a TSP [see page 1].*
NPO-19928

Torque-Limiting Driver Based on Displaceable Bevel Gear

The use of multiple intermediate gears would contribute to reliability and long life.

Lyndon B. Johnson Space Center, Houston, Texas

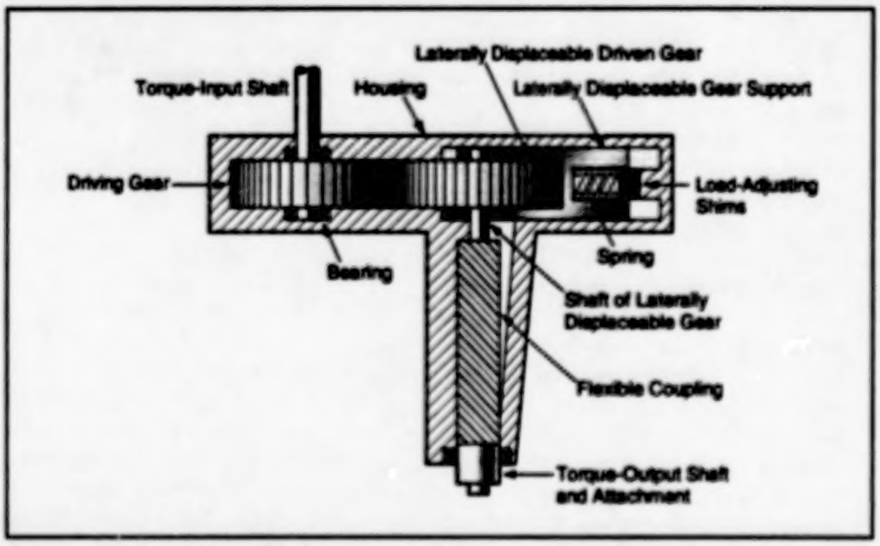

Figure 1. This Torque-Limiting Driver, a predecessor to the present improved driver, would have a displaced-axis configuration that could give rise to a spurious bending moment.

A proposed improved torque-limiting driver would act similarly to a number of other devices in that it would limit an applied torque to a preset value. Thus, a combination of this driver with an ordinary wrench would act as a conventional torque wrench. As in another proposed torque-limiting driver of the same type, the torque would be limited in this driver by the slippage of gears that would be spring-loaded against each other. Both proposed drivers are related to the driver described in "Tool for Driving Many Fasteners Simultaneously" (MSC-22386), *NASA Tech Briefs*, Vol. 19, No. 7, (July, 1995), page 24.

The other proposed driver of the same type (see Figure 1) would contain a single driving gear and a single driven gear, so that during a significant fraction of the time, a single tooth on each gear would bear the entire torque load. In the improved driver, the transmission of torque and the slippage would occur at multiple simultaneously meshing gears, so that no single gear tooth would have to bear the entire load. The reduction of the loads on individual gear teeth would reduce wear and reduce the probability of breakage of gear teeth, thus increasing the reliability and prolonging the useful life of the driver.

In the other driver, the input and output torque-drive axes would be offset from each other. As a consequence, the inadvertent application of an axial force during use would result in the application of a spurious and possibly damaging bending moment to the driven nut, bolt, or shaft. The improved driver would have an in-line drive configuration, which would eliminate this spurious bending moment.

In the improved torque-limiting driver, the spring loading and slippage of gears would occur in the axial direction, and all loads would be distributed symmetrically about the single drive axis (see Figure 2). The input torque would be applied by a wrench to the upper torque coupling, then transmitted through the torque-input shaft to the axially displaceable bevel gear, which would be axially spring-loaded against several intermediate bevel gears. Provided that the applied torque was less than the preset limiting torque, the intermediate bevel gears would transmit the torque to the output bevel gear.

Because of the inclinations of the gear teeth, the driving forces between engaged teeth would include circumferential, radial, and axial components. The circumferential force would produce the output torque, but in other situations, the radial and axial forces are often considered wasteful byproducts. In this case, however, the axial force would be used to control the output torque. When the transmitted torque reached the preset limit, the axial force at the engaged teeth of the displaceable bevel gear and the intermediate bevel gears would equal the axial load applied by the torque-control spring. An attempt to apply a greater torque would cause the axially displaceable bevel gear to move away from the intermediate bevel gears.

Continued turning in an attempt to apply a greater torque would cause the gears to disengage, slip, and re-engage repeatedly.

The axial force that pushed the gears apart against the torque-control-spring load would be proportional to the applied torque. The factor of proportionality would be a function of the geometrical relationships between the axially displaceable gear and the intermediate bevel gears. The torque-control spring and its adjustment would be designed according to this factor of proportionality. The spring preload load and thus the preset limiting torque would be adjusted by turning a micrometer-type adjustment knob to one in a set of calibrated torque-setting marks on the side of the housing.

The input attachment would contain a spring-loaded, splined coupling between itself and the torque-input shaft. The axial-load-limiting spring would be used to limit the amount by which the output torque could increase when the technician applied an axial load to the input attachment. When the applied axial load exceeded the preload on this spring, the spring would become compressed and the splines would disengage, so that no input torque would be transmitted.

This work was done by Joseph S. Cook, Jr., of **Johnson Space Center**. *Further information is contained in a TSP [see page 1].*

This invention is owned by NASA, and a patent application has been filed. Inquiries concerning nonexclusive or exclusive license for its commercial development should be addressed to the Patent Counsel, Johnson Space Center [see page 1]. Refer to MSC-22384.

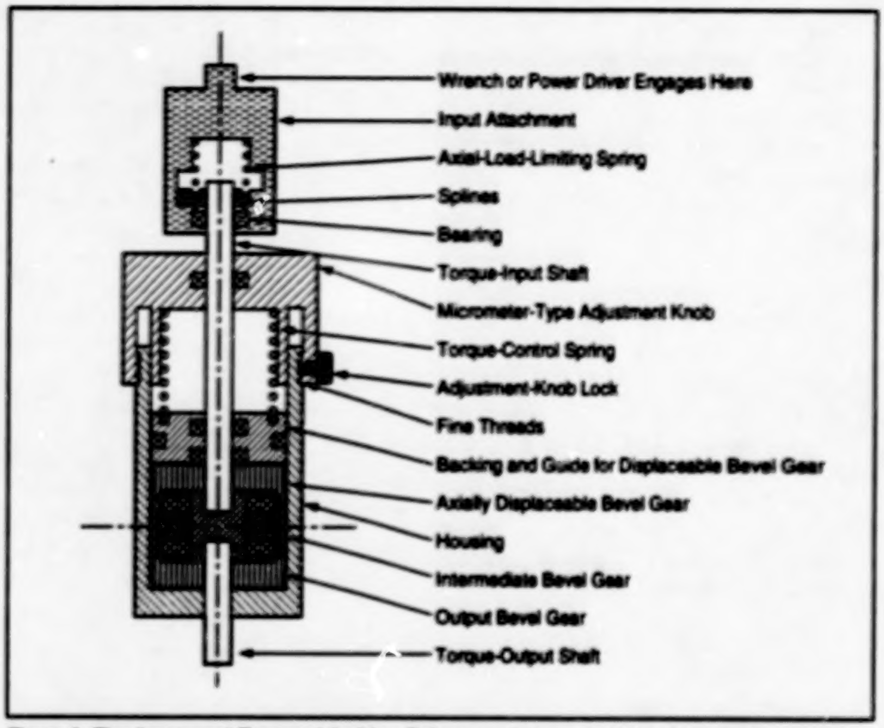

Figure 2. The **Improved Torque-Limiting Driver** would have an inline drive configuration.

Pneumatically Loaded Torque-Limiting Driver

The limiting torque would be a function of air pressure.

Lyndon B. Johnson Space Center, Houston, Texas

The figure illustrates a proposed pneumatically loaded torque-limiting driver related to the mechanism described in "Tool for Driving Many Fasteners Simultaneously" (MSC-22386), *NASA Tech Briefs*, Vol. 19, No. 7, (July, 1995), page . It is also related to the mechanisms described in the preceding article, "Torque-Limiting Driver Based on Displaceable Bevel Gear" (MSC-22384).

With the exception of the components used to set the limiting torque, the present mechanism would be nearly identical to the mechanism illustrated in Figure 1 of the preceding article. The driven gear would be connected to the output shaft via a flexible coupling and would be mounted in a gear support that was capable of sliding radially (laterally). As in other torque-limiting mechanisms based on the same principle, the

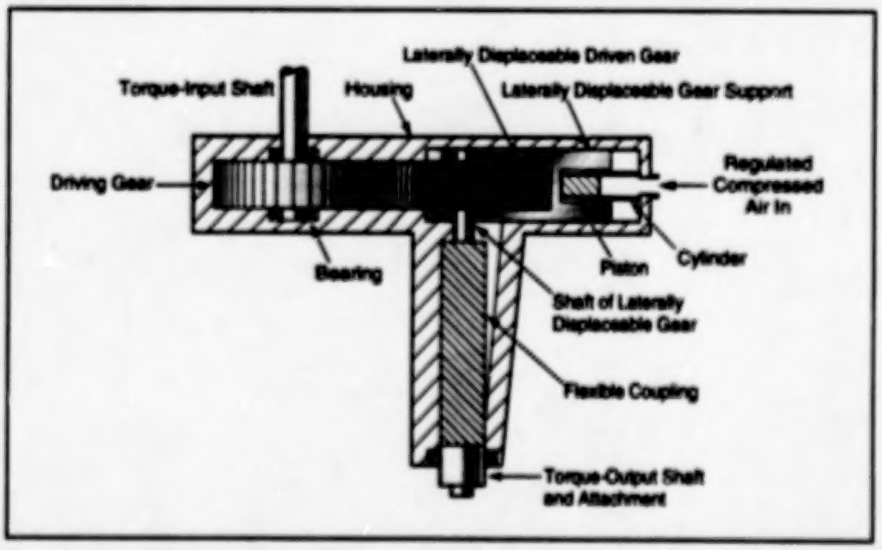

Compressed Air at Regulated Pressure would be applied to the piston to push the gears together with a constant preload. The limiting torque would be the torque strong enough to force the gears to slip out of engagement at that preload.

gears would be pushed together with a preload that would define the limiting torque. This load would counteract the lateral repulsion between the gears. The lateral repulsion would be proportional to the applied torque, the factor of proportionality being a function of the gear-tooth geometry.

As long as the applied torque remained less than the preset limiting torque, the gears would remain in mesh and would thus transmit the torque from the input shaft to the output shaft. At the preset limiting torque, the lateral repulsion would equal the preload. Any attempt to apply a greater torque would cause the repulsion to exceed the preload, and the gears would be pushed apart. Continued turning in an attempt to apply a greater torque would cause the gears to disengage, slip, and re-engage repeatedly.

In the mechanism shown in Figure 1 of the preceding article, the preload would be applied by a spring. Unfortunately, deflection of the spring between the point of initial yielding and the point of slippage would result in an increase in preload and a concomitant increase in the limiting torque. The resulting torque range would constitute a band of uncertainty in the output torque. In addition, fatigue in the spring could decrease the stiffness of the spring, thus reducing the preload and adding another element of uncertainty to the torque setting.

In the mechanism proposed here, the preload would be applied to the laterally displaceable gear support by a piston sliding in a cylinder. Compressed air at regulated pressure would be supplied to the cylinder. The preload would equal the pressure × the cross-sectional area of the piston. The preload would thus remain constant as long as the regulated pressure remained constant, resulting in more precise control of torque.

This work was done by Joseph S. Cook, Jr., of **Johnson Space Center**. *Further information is contained in a TSP [see page 1].*

This invention is owned by NASA, and a patent application has been filed. Inquiries concerning nonexclusive or exclusive license for its commercial development should be addressed to the Patent Counsel, Johnson Space Center [see page 1]. Refer to MSC-22385.

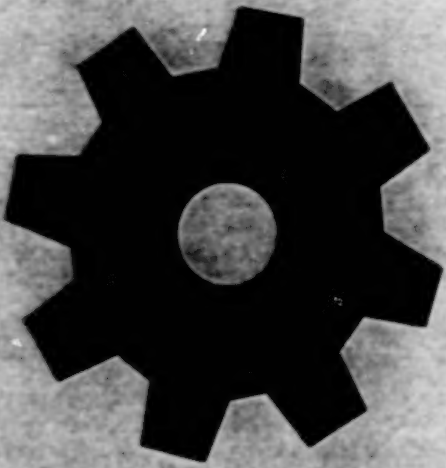

Machinery

Hardware, Techniques, and Processes

BLANK PAGE

Apparatus for Testing Sliding Seals for Hypersonic Engines

Seals are exposed to high-temperature conditions like those expected in service.

Lewis Research Center, Cleveland, Ohio

An apparatus is designed for testing specimens of sliding seals that are under consideration for use in advanced hypersonic aircraft engines. These variable-area-ratio engines require movable panels and panel seals to maximize engine thrust over the mach range of 0 – 25 (mach 1 = speed of sound). The sliding seals are needed to prevent the leakage of hot, pressurized engine gases through the gaps between the sliding panels and the walls. Several proposed designs for these seals were described in prior articles in *NASA Tech Briefs*; these articles were "Dynamic, High-Temperature, Flexible Seal" (LEW-14672, U. S. Patent no. 5,014,917), Vol. 13, No. 4 (April, 1989), page 101; "Dynamic, High-Temperature, Flexible Seals" (LEW-14695, U. S. Patent no. 4,917,302), Vol. 16, No. 3, (March, 1992), page 71; "High-Temperature, Flexible, Pressure-Assisted Brush Seal" (LEW-15086, U. S. Patent no. 5,076,590), Vol. 17, No. 2 (February, 1993), page 74; and "High-Temperature, Flexible, Fiber-Preform Seals" (LEW-15085, U. S. Patent no. 5,082,293), Vol. 17, No. 2 (February, 1993), page 75.

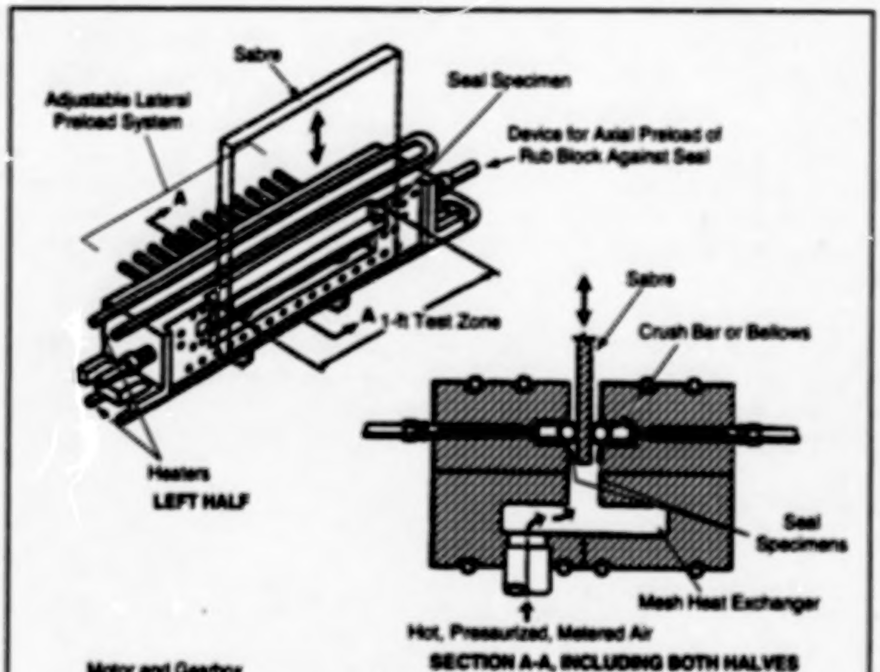

This **Hot Dynamic Seal Rig** is an apparatus for testing sliding seals under conditions like those anticipated in advanced hypersonic engines.

Using air as the test gas, the apparatus can measure leakage at temperatures from ambient to 815 °C (1,500 °F) and differential pressures up to 690 kPa (100 psi). The performance of the seal specimens can be measured while sealing against flat or distorted walls. In the apparatus, two horizontal seal specimens are preloaded against opposite sides of a device called a "sabre," which is a plate that simulates an engine wall and is slid transversely to the axes of the seals (that is, vertically) to simulate the scrubbing motions anticipated in engines. The surface of the sabre can be made flat or distorted and smooth or rough, as needed, to test the performance and durability of the seal specimens.

The length of the seal specimens and the corresponding long horizontal dimension of the sabre is about 30 cm (1 ft). The range of vertical motion of the sabre is ±5 cm (±2 in.). The sabre is moved vertically by use of a motor, gearbox, and crank; the average vertical speed is adjustable from 0 to 5 cm/s (0 to 2 in./s). The vertical position of the sabre is measured by a linear variable-differential transformer. The number of cycles of vertical motion is measured by a cycle counter connected to the crankshaft.

Rub blocks (not shown in the figure) prevent leakage at the ends of the seal specimens. The rub blocks are machined to seal precisely against the ends of the sabre. By use of pressurized bellows, the rub blocks are pneumatically preloaded, both against the sabre and lengthwise against the ends of the seal specimens.

The seal specimens can be preloaded against the sabre in either of two ways depending on the sealing concept under test; either variable-preload forces can be applied by pressurized bellows, or else the seal specimens can be crushed to a fixed extent by use of a shimmed crush bar.

Metered, pressurized air is supplied to a plenum in the base of the apparatus, upstream from (below) the seal specimens. Four 3.5-kW electrical-resistance air heaters operating under digital control with temperature feedback are threaded into the base. The plenum contains a

mesh heat exchanger, which diffuses the flows of air and heat. Each heater is controlled by a digital controller with temperature feedback. The heaters can supply air at a temperature of 815 °C (1,500 °F) at a flow rate of 0.009 kg/s (0.02 lb/s).

Leakage past the seal specimens is measured by flowmeters, which are placed upstream of the heaters to eliminate the need to capture and cool the leaking hot gas. The differential pressure across the seal specimens is measured by use of pressure taps, immediately upstream of the seal specimens, connected to room-temperature pressure transducers via tubes that are >15 cm long to prevent heating of the pressure transducers. Pressures in the seal cavities and in the preload bellows are also measured. The temperature of the impinging hot air is measured by thermocouples just upstream of the seal specimens. Load cells in the linear carriage assembly that supports the sabre measure seal drag; that is, friction between the seal specimens and the sabre.

NASA Lewis used this test fixture to evaluate the hot sliding durability performance of a number of candidate hypersonic engine seals, as documented in NASA TP-3483.

This work was done by Bruce M. Steinetz of **Lewis Research Center**, *Jeffrey H. Miller and Paul J. Sirocky of Sverdrup Technology, Inc., and Lawrence A. Kren of Case Western Reserve University. Further information is contained in a TSP [see page 1].*

Inquiries concerning rights for the commercial use of this invention should be addressed to the Patent Counsel, Lewis Research Center [see page 1]. Refer to LEW-16211.

Enhancement of the NA4 Gear-Vibration Diagnostic Parameter

This version of NA4 provides a more sensitive indication of damage.

Lewis Research Center, Cleveland, Ohio

"NA4*" denotes an enhanced version of the NA4 gear-vibration diagnostic parameter, which was described in "Analyzing Vibrations To Detect Damage on Gear Teeth," (LEW-15974), *NASA Tech Briefs*, Vol. 21, No. 2 (February 1997), page 1b. NA4 is one of several time-varying statistical parameters that are computed from measurements of vibration in gear trains to detect damaged gear teeth. Vibration-analyzing systems that compute NA4 and the other parameters are being developed to monitor gear drives to provide timely warnings during operation.

Vibration in a gear train is measured using an accelerometer mounted on the gear housing. The instantaneous output of the accelerometer is recorded digitally. A synchronizing signal is recorded with the vibration signal to allow time-synchronous averaging. Time-synchronous averaging reduces the effect of incoherent noise and improves the signal-to-noise ratio.

NA4 was developed to overcome some of the limitations of another parameter, called "FM4," that is widely accepted in industry. In preparation for computing NA4, the data are preprocessed into a residual signal by removing certain components synchronous with the meshing of gears while retaining first-order sidebands. NA4 is defined as the normalized fourth statistical moment of the residual signal divided by the square of the current run-time averaged variance of the residual signal. NA4* is similar to NA4 in that its numerator is also the kurtosis of the residual signal. However, the denominator of NA4* is the square of the variance of the undamaged gearbox signal.

The change from NA4 to NA4* allows the parameter to continue to grow with the severity of the fault. NA4* is a parameter that is more robust when damage progresses since the comparison is being made to the gearbox when it was in a good condition. The formulation of NA4* provides for indication of damage both at initiation and as damage progresses. In experiments on spur- and spiral-bevel gear fatigue test rigs, the performance of NA4* was examined and compared with those of NA4 and FM4 (see figure). In these experiments, the primary failure mode was pitting of gear-tooth surfaces. The following conclusions were drawn from the comparisons:

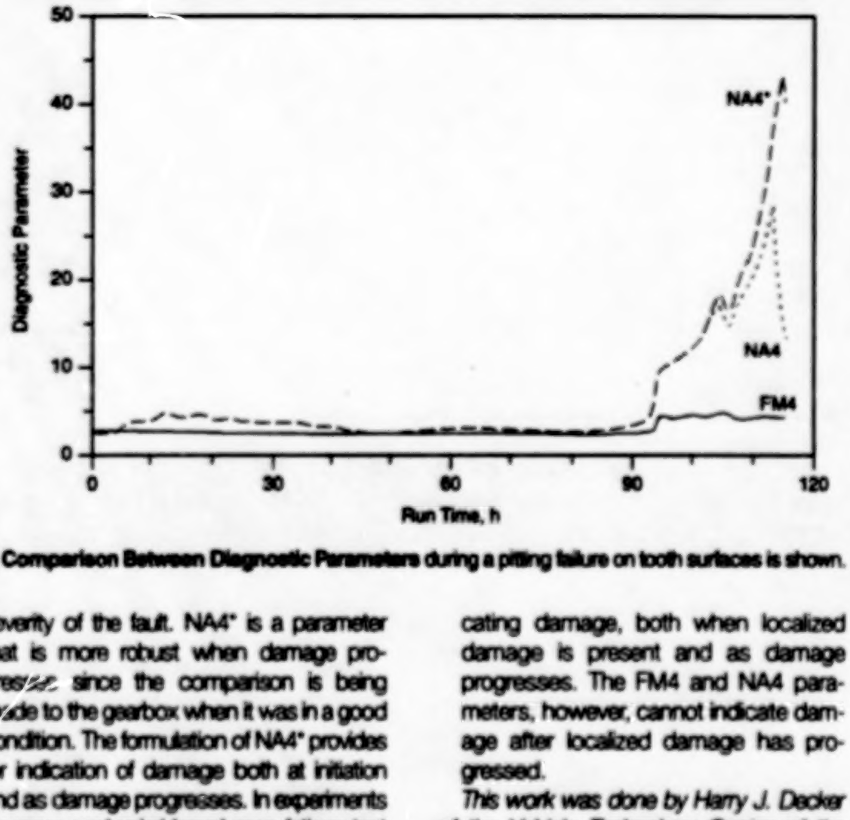

A Comparison Between Diagnostic Parameters during a pitting failure on tooth surfaces is shown.

- In almost all cases, NA4* gave a more sensitive indication of damage than did NA4.
- NA4* was found to be less likely to fail to indicate damage than were NA4 and FM4.
- NA4* was found to be capable of indicating damage, both when localized damage is present and as damage progresses. The FM4 and NA4 parameters, however, cannot indicate damage after localized damage has progressed.

This work was done by Harry J. Decker of the Vehicle Technology Center of the U.S. Army Research Laboratory, James J. Zakrajsek of **Lewis Research Center**, *and Robert F. Handschuh of the Vehicle Technology Center of the U.S. Army Research Laboratory. Further information is contained in a TSP [see page 1].*

Inquiries concerning rights for the commercial use of this invention should be addressed to NASA Lewis Research Center, Commercial Technology Office, Attn: Tech Brief Patent Status, Mail Stop 7-3, 21000 Brookpark Road, Cleveland, Ohio 44135. Refer to LEW-16284.

Automatic Regulation of Material Level in Industrial Blender

A control system automatically regulates the level of material in an industrial blender in which maintaining the correct level is necessary for both product quality and safety. The blender includes a mixing chamber with a turbine-type head that mixes two powder streams that enter from the top, with a liquid stream that enters from the bottom. The resulting blend flows out of the chamber through a discharge gate at its bottom. The level-regulating control system includes two level sensors on the side of the chamber, one slightly above the other. The outputs of these sensors are fed to a programmable-logic controller (PLC) that, in turn, controls a linear actuator that varies the opening of the discharge gate. The PLC modulates the gate opening to maintain the material level between the two sensors. A third sensor on the chamber lid provides redundant protection against flooding: if the material level rises to near the lid, the output of this sensor triggers an emergency shutdown of all material feeders.

This work was done by Joel Crook of Thiokol Corp. for **Marshall Space Flight Center**. *Further information is contained in a TSP [see page 1].*
MFS-31127

Vibration-Isolation System for Industrial Blender

A pneumatic suspension system for the industrial blender described in the preceding article suppresses low-frequency vibrations generated by the motor that drives the blender. It is necessary to suppress these vibrations because they can affect feed rates of the materials to be mixed and thereby alter the composition of the blend beyond narrow tolerances. The suspension system includes air bladders that support an outrigger frame that, in turn, supports the blender frame. When the bladders are inflated to a nominal pressure of 50 psig (gauge pressure of 0.34 MPa), the outrigger floats between upper and lower limit stops. Flexible inlet and outlet connections are needed to accommodate the flotation: The liquid-supply line is a polytetrafluoroethylene-lined hose enclosed in stainless-steel braid. The powder-supply lines are convoluted hoses. A specially designed flexible outlet assembly includes a sloped enclosed trough that enters a vertical discharge pipe through a loosely fitting notch in the pipe. A boot on this assembly encloses the process stream and accommodates the flotation of the blender as a whole, the motion of the discharge gate, and the motion of a transparent cover on the top of the pipe that moves with the discharge-gate actuator linkage.

This work was done by Joel Crook of Thiokol Corp for **Marshall Space Flight Center**. *Further information is contained in a TSP [see page 1].*
MFS-31126

BLANK PAGE

58

Fabrication Technology

Hardware, Techniques, and Processes

Books and Reports

BLANK PAGE

Sputter Texturing To Prepare Surfaces for Bonding

Patterns are defined by small ceramic particles temporarily attached to surfaces to be textured.

Lewis Research Center, Cleveland, Ohio

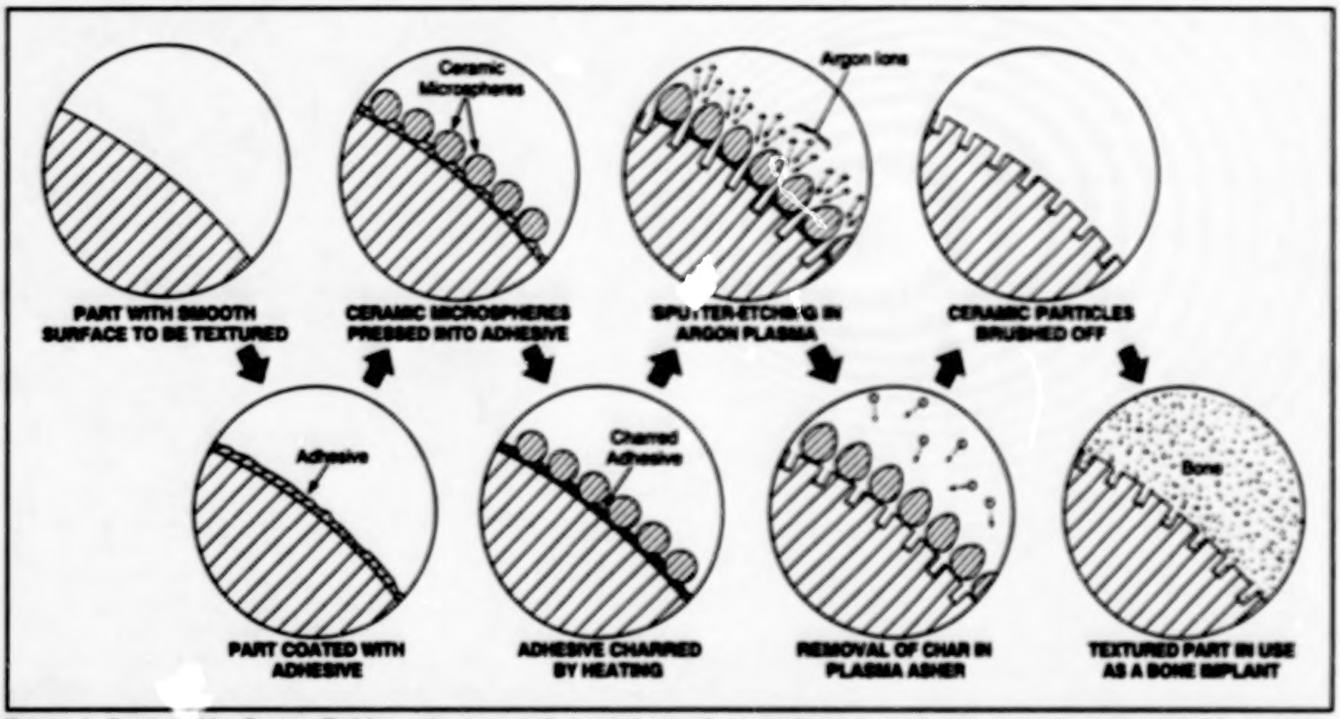

Texture Is Produced by Sputter Etching, using temporarily bonded ceramic microspheres to mask areas not to be sputter-etched in an argon plasma. When etching is complete, the charred adhesive is removed to release the particles. A textured, bondable surface remains.

A process for texturing the surfaces of complexly shaped metal parts includes a sputter-etching step in which the areas not to be etched are masked by small ceramic particles temporarily attached to the surfaces. By choice of the sputtering parameters and the size and distribution of masking particles, the width and depth of the textured features can be controlled over a wide range. Texturing improves bonding to other parts. The process has been used to texture metal fixtures to be anchored to composite-material (matrix/fiber) structural components. It could also be used to texture such prosthetic items as hip implants; textures could be sized and shaped to favor the ingrowth of adjacent bone to anchor the implants. [A related process for texturing molds for implants was described in "Improved Texturing of Surgical Implants for Soft Tissues" (LEW-15805), *NASA Tech Briefs*, Vol. 21, No. 1 (January, 1997), page 70.]

Unlike some other texturing processes, this process does not create loosely adherent particles which could lead to the formation of wear-causing debris. The widths and depths of etch pits can be controlled so that ingrown tissue is assured of nourishment or so that an adhesive material can grip strongly. The part is not overheated during the process, and its mechanical properties are therefore not degraded. The process can be used on recessed surfaces as well as on exposed ones.

The process consists of the following steps (see figure):

1. By spraying or dipping, a film of contact adhesive is applied to the surface of the part to be textured.
2. Ceramic microspheres are pressed into the adhesive.
3. The part is heated in an oven to drive off volatile constituent compounds and char the adhesive.
4. The part is placed in the discharge chamber of an ion source or triode sputtering apparatus that operates with argon gas. The part is biased between −500 and −2,000 volts with respect to the plasma in its vicinity, causing argon ions to bombard the part and thus to sputter-etch the char and the underlying metal in the areas not covered by the ceramic microspheres. The depth of the etch is controlled by the voltage on the part, the duration of sputtering, and the ion-current density.
5. The part is placed in a radio-frequency plasma asher, where atomic oxygen removes the remaining charred adhesive.
6. The microspheres are brushed away.

Typically, in the case of a bone implant, the part to be textured is made of pure titanium or an alloy of 90 percent titanium, 6 percent aluminum, and 4 percent vanadium. A part to be textured for use in another application could be made of any of a variety of electrically conductive materials such as metals, carbon, and composites that contain metals and/or carbon. Mixtures of microspheres of different sizes can be used to obtain complex textures.

This work was done by Bruce A. Banks of **Lewis Research Center**. *Further information is contained in a TSP [see page 1].*

Inquiries concerning rights for the commercial use of this invention should be addressed to the Patent Counsel, Lewis Research Center [see page 1]. Refer to LEW-15823.

Fiducial Grids for High-Resolution Beam Lithography

The position of a beam can be determined to within a few nanometers.

Marshall Space Flight Center, Alabama

Fiducial rectangular grids are essential components in a method for making high-resolution masks with patterns accurate enough for use in x-ray lithography. High accuracy is necessary for achieving correct registration of multiple overlaid layers in integrated electronic circuits fabricated by use of such masks.

A mask of this type is made by electron-, ion-, or photon-beam lithography. Heretofore, it has been necessary to estimate the position (x,y) of the beam in the two dimensions of the mask plane by use of the position readouts from a translation stage and/or any other device(s) used to scan the beam across the plane to form the pattern. Errors in the position estimates can arise from multiple sources, including thermal expansion, backlash and manufacturing tolerances in positioning mechanisms, misalignment between the substrate and scanning plane, nonorthogonality between the beam and substrate at some positions, and (in the case of an ion or electron beam) deflection of the beam by stray electric and magnetic fields. In the present method, one measures the position of the beam with the help of a fiducial grid; thus, it is no longer necessary to rely on possibly inaccurate beam-position estimates.

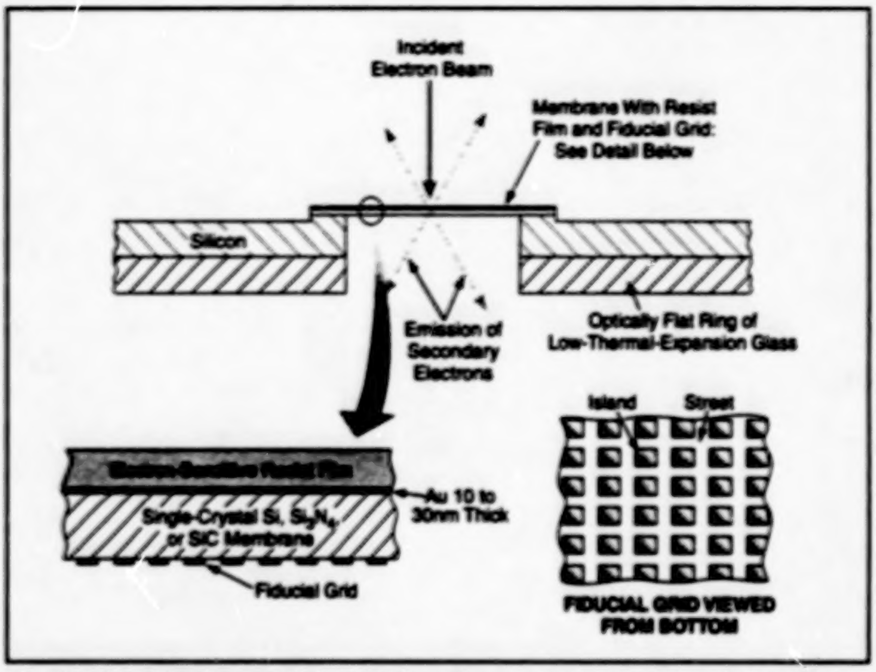

The Position of Impingement of the Electron Beam on the membrane can be identified as being on either an island or a street of the fiducial grid, as indicated by the level of emission of secondary electrons.

A fiducial grid of the type used in this method comprises metal-film islands separated by cross streets of comparable width and is either (1) formed on a surface or interior layer of, or else (2) mounted in a plane very close to, a multilayer membrane or a thicker substrate that one seeks to pattern into a mask by an electron-, photon-, or ion-beam lithographic process. A fiducial grid can be fabricated by holographic lithography; this technique is chosen because it can be manipulated to obtain a set of cross gratings that are free of distortion or in which the distortion is exactly predictable. The gratings constitute a set of (x,y) position references across the area to be patterned by the scanning beam.

The method can be practiced in many different versions, depending on specific applications. The figure illustrates an application that involves electron-beam lithography on a substrate with an electron-sensitive resist film on its top surface and a fiducial grid on its bottom surface. For measurement of position, the beam is attenuated so that it is not intense enough to produce appreciable changes in the electron-sensitive resist film yet is intense enough to cause emission of a measurable current of secondary electrons. This current can be measured by use of channel electron multipliers or other devices like those used to measure secondary electrons in scanning electron microscopes.

The secondary-electron yields of the islands and streets differ in a known way. Thus, at any instant as the beam is scanned across the grid, the level of the secondary-electron signal indicates whether the beam is impinging on an island or a street. If a raster scan is performed, then the secondary-electron readout can be processed, along with the scanning parameters and the scanning-apparatus readouts, by use of algorithms based on established techniques for analysis of moiré and interference fringes. These techniques make it possible to determine (x,y) position to within a fraction of the spatial period of the fiducial grid. In a typical case, the spatial period would be 200 nm, and one could determine the position of the beam to within 20 nm or less.

This work was done by Henry I. Smith, Erik H. Anderson, and Mark L. Schattenburgh of Massachusetts Institute of Technology for **Marshall Space Flight Center**. *Further information is contained in a TSP [see page 1].*

In accordance with Public Law 96-517, the contractor has elected to retain title to this invention. Inquiries concerning rights for its commercial use should be addressed to

Massachusetts Institute of Technology
77 Massachusetts Avenue
Cambridge, MA 02139

Refer to MFS-26300, volume and number of this NASA Tech Briefs *issue, and the page number.*

Books and Reports

VPS Fabrication of Parts To Withstand High Temperatures

A short paper reviews the state of the art of making refractory-metal and ceramic/refractory-metal composite objects by vacuum plasma spraying (VPS) of the constituent materials onto graphite mandrels. In large part, the paper reiterates descriptions of selected aspects of VPS fabrication technology of high-temperature parts as reported in prior articles in *NASA Tech Briefs*; namely, "Removable Mandrels for Vacuum-Plasma-Spray Forming" (MFS-30005), Vol. 19, No. 5 (May 1995), page 82, and "VPS Fabrication of Ceramic/Metal Furnace Cartridges" (MFS-29998), Vol. 21, No. 4 (April 1997), page 69. The paper is oriented somewhat toward the VPS fabrication of refractory-metal parts to withstand temperatures up to 4,500 °F (about 2,500 °C) in small solar thermal rocket engines, but the paper also indicates that the VPS fabrication technology is applicable to the commercial manufacture of small high-temperature parts for other uses.

This work was done by Philip D. Krotz of Rockwell International Corp. and William M. Davis of Boeing North American, Inc., for **Marshall Space Flight Center**. *To obtain a copy of the paper, "Vacuum Plasma Spray Fabrication of Solar Thermal Rocket Engines," see TSP's [page 1].*
MFS-30104

BLANK PAGE

64

Mathematics and Information Sciences

Hardware, Techniques, and Processes

BLANK PAGE

Collar Grids for Computing Flows at Intersections

Collar grids resolve the interaction regions and provide communication between component grids.

Ames Research Center, Moffett Field, California

Collar grids are placed at intersections of surfaces in an improved version of the chimera overlapping-grid scheme that is used in computing flow fields about aircraft and other complicated bodies. In the chimera scheme, multiple overlapping component grids that conform to the surfaces of wings, fuselages, and other components are used to solve the Navier-Stokes or Euler equations of flow by numerical integration. Information on the flow fields at the boundaries between grids is communicated between component grids by interpolation. However, for computations of viscous flows in the vicinities of intersections between surfaces (e.g., wing/fuselage intersections), the generation of suitable grids and the mathematical analogs of stencils to be used in interpolations in the intersection regions is not straightforward. Problems arise in connection with such matters as the resolution of the intersection regions and the appropriate definitions of the surfaces. The collar grids were devised as solutions of these problems.

In a representative application of the chimera scheme to an intersection between a cylinder and a curved surface, holes are cut in the two component grids in the intersection region (see Figure 1). In computation, holes are implemented by deleting the points in the holes from the domain; that is, by setting the contributions of those points to changes in the flow field equal to zero. Those points of each component grid that lie on the boundary of its hole are the points that receive flow-field data interpolated from the other component grid.

In the improved version of the chimera scheme, the overall hole formed by superposition of the two holes is filled with the collar grid (see Figure 2). The collar grid provides the communication between the component grids and spatially resolves the computed flow field in the intersection region. To avoid problems that might otherwise arise in geometric conflicts between the fine grid needed to resolve viscous flow in the intersection region and a typical component surface grid, the edges of the collar surface grid are generated by trilinear interpolation of the component surface grids. Component-grid points on the boundaries of the holes are moved to the surfaces defined by the collar grids. Once the collar and component grids are thus configured, interpolation stencils generated by the grid-joining software correctly reflect the relative locations of the component and collar grids. No other modifications of the chimera scheme and no modifications of the flow-computing algorithm are needed.

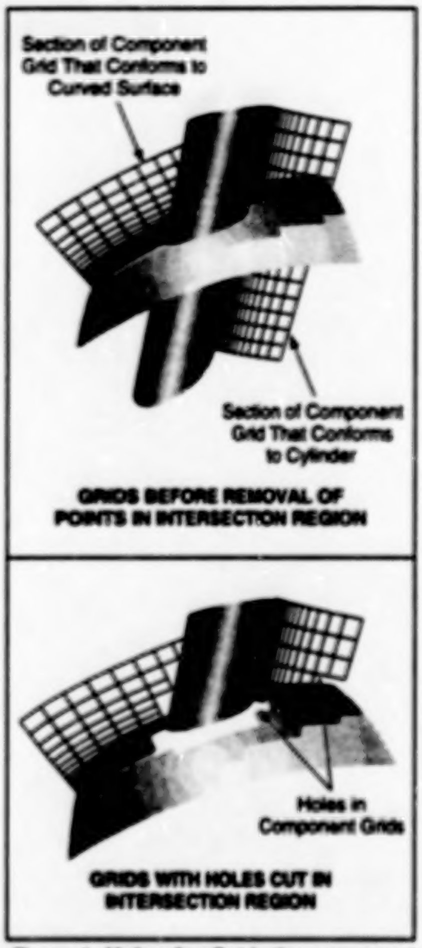

Figure 1. **Holes Are Cut** in the component grids at the intersection of a cylinder and a curved surface.

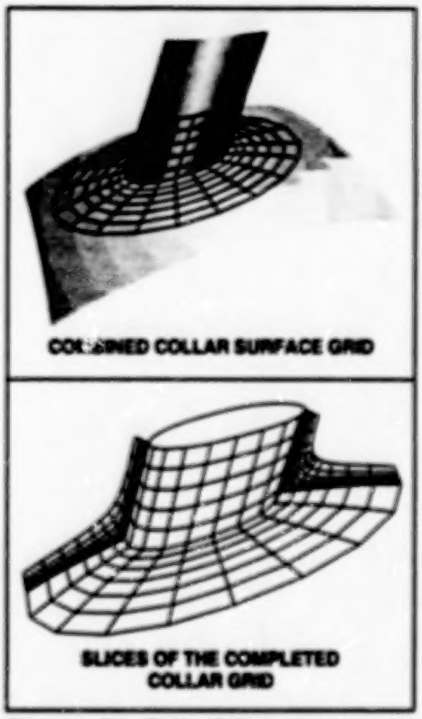

Figure 2. The **Collar Grid** is placed in the holes, filling the intersection region.

This work was done by Pieter Buning of **Ames Research Center**, *Steven J. Parks of Lockheed Engineering & Sciences Co., William Chan of MCAT Institute, and Joseph Steger of the University of California, Davis. Further information is contained in a TSP [see page 1].*
ARC-13183

Software for Managing Multidimensional Data Files

Users are relieved of much of the burden of translating between data formats.

Goddard Space Flight Center, Greenbelt, Maryland

The Common Data Format (CDF) Library is a portable software package for managing collections of scientific data that were originally recorded on magnetic tapes and other media in a variety of hardware- and software-based formats. Developed at the National Space Science Data Center at NASA's Goddard Space Flight Center for use in storing and distributing data, this software has also been distributed internationally and adopted by thou-

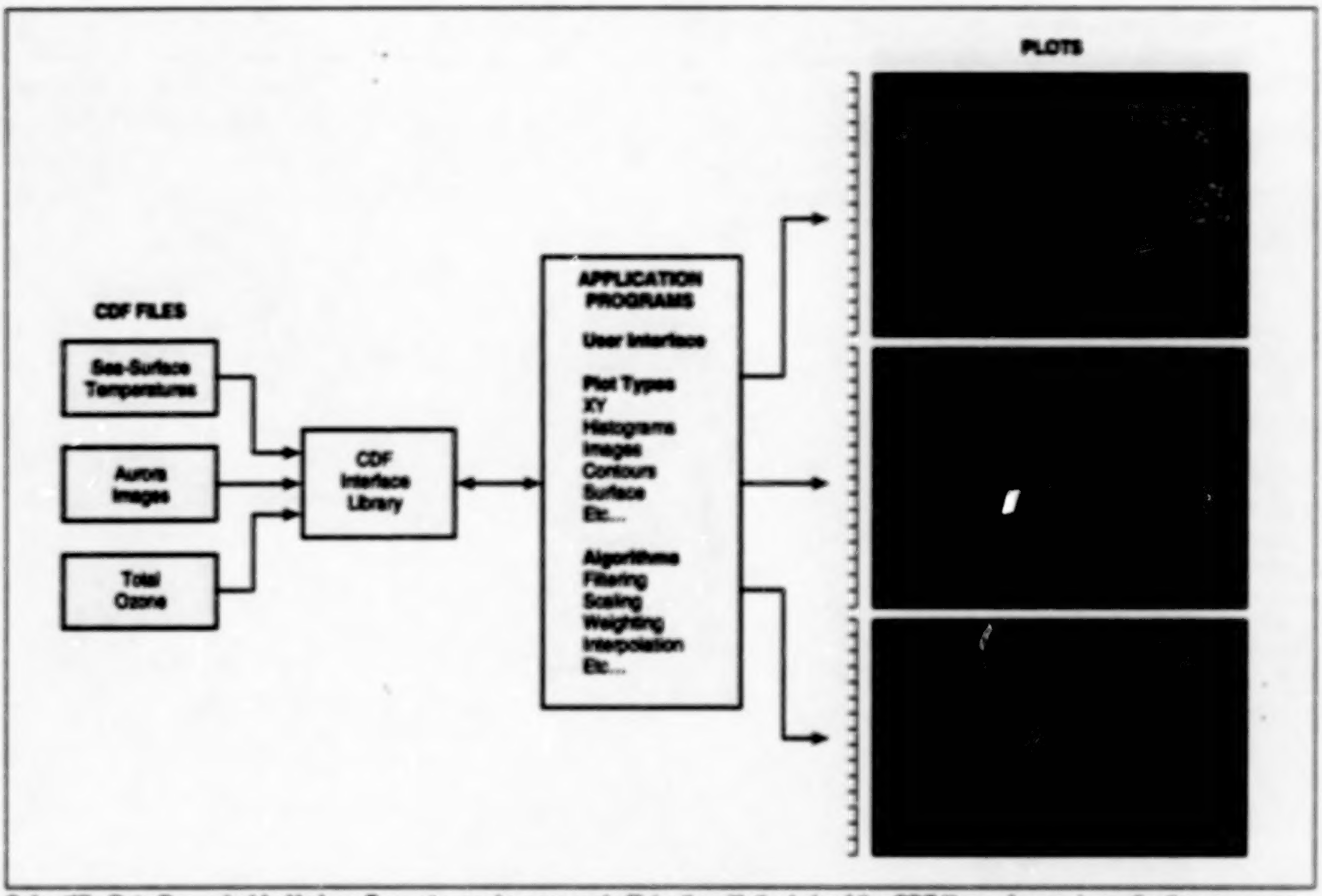

Scientific Data Recorded in Various Formats can be managed efficiently, with the help of the CDF library, for use in application programs.

sands of users that include government agencies, universities, commercial organizations, and independent researchers.

The CDF Library can save much time in the storage and retrieval of scientific data, minimizing the need for users to translate between different data and encoding formats. The hallmark of the CDF library is independence of data-management functions from specific sets of data. This independence is achieved by means of an internal format that is transparent to the programmer and is accessible through an easy-to-use standard set of interface routines in FORTRAN- and C-language versions. In a given application, the internal format includes a data dictionary (metadata) supplied by the user, plus the data themselves. Thus, in effect, the CDF describes itself; this self-describing property is what makes the CDF useful for managing data that originate in various formats from various scientific disciplines.

By itself, the concept of using an internal data dictionary to describe the contents of a data file and thereby achieve a data-independent, transportable standard format is not new. The unique contribution made by the CDF Library to go beyond modern business-oriented commercial relational data-management software to support multidimensional, hierarchical data structures, enabling programmers to manage multidimensional data in ways consistent with the geometries of their own scientific organizations. The CDF Library also serves as a software framework that facilitates the creation of generic application programs for typical data-management and data-abstraction functions like visualization, statistical analysis, and browsing. The CDF Library enables programmers to easily create application programs that enable users to slice data across multidimensional subspaces, gain access to entire structures of data, perform subsampling of data, and gain access to one element regardless of its relationship to any other element (see figure).

Both the metadata and the data are accessible via the interface routines, which afford the programmer an abstract view of the contents of the CDF. The programmer need not know the details of (and is isolated from) the CDF physical storage and the underlying software structure. The programmer does not have to perform low-level input/output functions to physically pack or unpack data or metadata into or out of files; the CDF software does this for the programmer. The physical files (CDF files) generated by the CDF Library can be retrieved directly or sequentially and can be stored on disks for access via a FORTRAN or C interface. The isolation of the programmer and user from the physical storage and the underlying software structure also make it possible to enhance the implementation of the CDF as new hardware and software become available.

This work was done by Gregory Gauchers, Jason Mathews, Jeff Love, and Howard Leckners of **Goddard Space Flight Center**. *Further information is contained in a TSP [see page 1].* GSC-13633

Algorithm for Improving a Mathematical Model

Linear least-squares solutions with optimal step sizes are iterated.

Marshall Space Flight Center, Alabama

The Analytical Model Improvement (AMI) computer program implements an iterative algorithm for improving a mathematical model of a physical system. The algorithm adjusts the parameters in the model to obtain a closer match between data on the behavior of the system as calculated by the model and the corresponding data obtained by experiment. The original application for which AMI was developed involves a vibrating structure represented by a finite-element model, the data of interest being the shapes (eigenvectors) and natural frequencies (eigenvalues) of the vibrational modes and the parameters of interest being the design parameters of the structure.

AMI was developed with recognition that in a general case, both the experimental data and the mathematical model can contain errors. AMI seeks a least-squares best fit between the model and experimental data. The process begins with calculation of an error vector, Δ, the elements of which consist of differences between the experimental and model data. Typically, these data are the eigenvalues and the components of the eigenvectors. At first, it is assumed that the following linear approximation applies:

$$\Delta = \mathbf{J}\delta,$$

where δ is a vector of design-parameter changes needed to bring the experimental and model data into agreement and $\mathbf{J}$ is the Jacobian matrix that contains partial derivatives of the model eigenquantities with respect to the design parameters. Singular-value decomposition is used to find a search direction in parameter space, which is identical to the linear least-squares solution δ.

Because significant nonlinearities are often present, the linear least-squares solution can diverge from the true solution, making it necessary to solve the model-improvement problem iteratively, as a sequence of linear least-squares problems. On each iteration, one must find a fraction, α, of the linear least-squares solution that yields an optimal match between the experimental and model data; in other words, on each iteration, the problem becomes one of finding α ($0 \leq \alpha \leq 1$) such that $\bar{\delta} = \alpha\delta$ yields a minimum value of an error measure (called the "residual") given by $r = |\Delta|_2$.

AMI implements two alternative methods for approximating the eigenquantities and finding a value of α that minimizes r. One method involves the use of a variation of the method of moving asymptotes; the other method involves the use of a generalized quadratic equation. In both methods, second-order approximations of the eigenquantities are obtained by use of first and second partial derivatives of the eigenquantities with respect to the design parameters. The first derivatives are determined by a finite-difference technique. After the first update cycle, the first derivatives can then be compared to the first derivatives from the previous cycle to estimate the primary second derivatives, also via a finite-difference technique. However, when a second derivative ≤ 0, a small positive number is substituted; this provides a so-called convex approximation, which yields a unique solution.

The second-order approximations of the eigenquantities provide an estimate of r that depends only on α; that is,

$$r(\alpha) = |\Delta(\alpha)|_2$$

A one-dimensional line-search optimization routine in the International Math and Statistics Library (IMSL) computer program is used to find the value of α that minimizes $r(\alpha)$. Then α is used to update the design variables via $\bar{\delta} = \alpha\delta$. This completes the computational cycle. Then using the updated design variables, a new cycle can be started. The iteration is stopped when sequential vectors of design variables converge.

This work was done by Matthew F. Orr, Jr., of **Marshall Space Flight Center.** *Further information is contained in a TSP [see page 1].*
MFS-31179

Software for Transforming Data Formats

This program features a menu- and table-driven user interface.

Goddard Space Flight Center, Greenbelt, Maryland

The Flight Dynamics Orbital and Mission Aids Transformation System (FORMATS) computer program collects data in the formats in which they are generated and distributes them in the same formats or any of a wide variety of different formats, as specified by users. FORMATS was developed for use in reformatting and distributing data generated during scientific spacecraft missions, but its adaptability to multiple formats may also be useful in terrestrial applications; for example, transforming data generated by laboratory instruments.

Because FORMATS incorporates selectable software components needed to transform data among many different formats, expensive reprogramming is not necessary to satisfy requirements for each new data-distribution task. A menu- and table-driven user interface in FORMATS makes it possible to select the needed data-format-transformation software components quickly and thus at low cost. There is minimal need for intervention by the user during execution of the program. The program also includes fault-tolerant features; for example, it repeats attempts to transmit data until it succeeds.

FORMATS includes the following software subsystems:

- A small executive subsystem to start or stop the execution of other subsystems;
- A poller that finds data products in local or remote sites;
- A transformation subsystem that recognizes data products and performs operations (for example, validation or reformatting) on the data as directed by tables and templates;
- A transmission subsystem that is

responsible for distributing data products to their respective destinations;

- An optional user-interface subsystem for displaying messages associated with the validity of processed data products; and
- A tables subsystem that enables the use of text files to specify the steps to be executed for each data product.

The heart of FORMATS is a generic data-transformation engine that can navigate any data file, regardless of its complexity, under the control of textual description of the file format, written in the Format Template Language (FTL). The sizes of individual data elements in files to be processed can range from one bit to two billion bytes. Formats that can be accommodated include those of American Standard Code for Information Interchange (ASCII), Extended Binary-Coded Decimal Interchange Code (EBCDIC), and special floating-point data types. Moreover, any time format can be accommodated, and data can be nested or structured in any defined way.

FORMATS can reside anywhere on a computer network that operates under the Transmission Control Protocol/Internet Protocol (TCP/IP). FORMATS has been executed on IBM RS6000 and HP 9000 computers under UNIX and is portable to any computer that uses the Microsoft Windows NT operating system. Approximately 1MB of random-access memory and 2MB of disk memory are required.

This work was done by Alan T. Johns, Douglas B. Reingold, and George E. Coon of CSC Communications Industry Services for **Goddard Space Flight Center**. *Further information is contained in a TSP [see page 1].*
GSC-13827

Life Sciences

Hardware, Techniques, and Processes

BLANK PAGE

Instrument Measures Populations of Microbes in Water

Microbes are identified via fluorescence spectra. *John F. Kennedy Space Center, Florida*

An instrument called an "on-line microbiological analyzer" measures the population densities of several species of microbes in flowing water. The instrument was conceived for use in monitoring harmful microbes in hydroponic nutrient solutions; modified versions could be used for similar monitoring of drinking water and treated waste-water. The instrument is based on the observation that microbes contain a variety of complex molecules that fluoresce when exposed to light of certain wavelengths; tryptophan, for example, emits light at a wavelength of 348 nm when it is stimulated by light at 287 nm. A microbe fluoresces in a spectrum that depends on the mix of fluorescent molecules that it contains; this mix is characteristic of its genus and species.

Therefore, the instrument illuminates flowing water with ultraviolet light to excite fluorescence in microbes and measures the fluorescence spectrum, which can comprise the characteristic fluorescence spectrum or spectra of one or more species of microbes. Then, by use of pattern-recognition algorithms, a host computer that controls the instrument analyzes the measured spectrum to identify and quantify the single characteristic spectrum or multiple component characteristic spectra, thereby estimating the population density or densities of the species present.

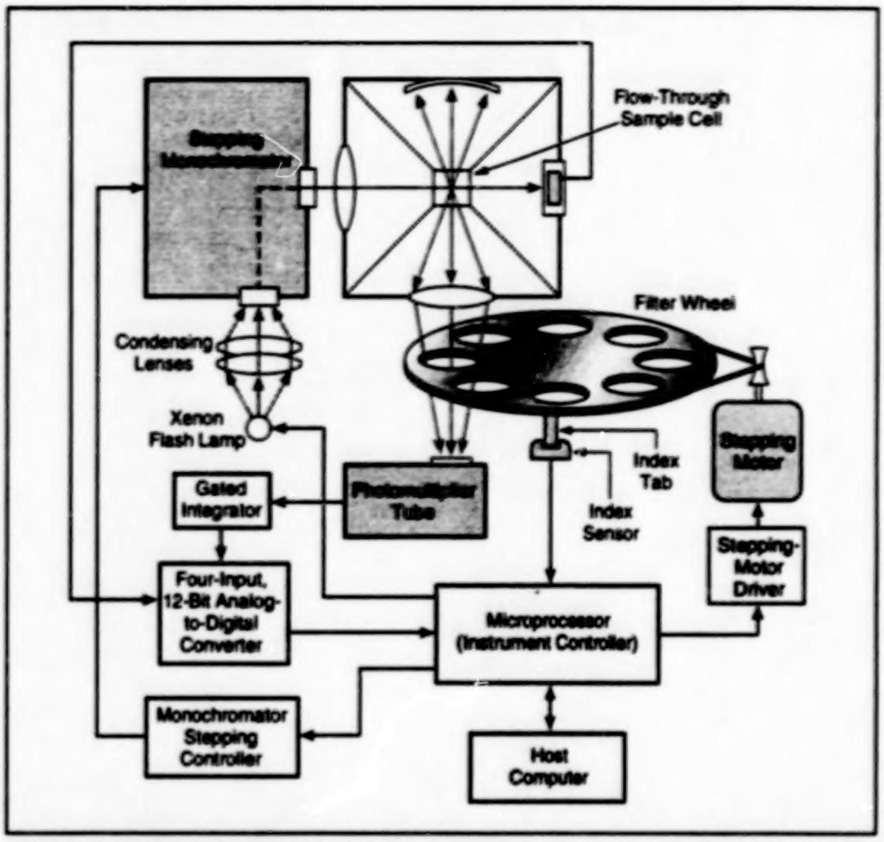

Light From the Monochromator Excites Fluorescence in microbes in water flowing through the cell. The photomultiplier converts filtered fluorescent emissions to signals for processing and analysis. The microprocessor coordinates the operations of the monochromator, the filter wheel, and the circuitry that process the output of the photomultiplier.

The instrument is illustrated schematically in the figure. A xenon flash lamp generates pulses of broad-spectrum light that pass through a monochromator and into a cell, through which flows the water to be monitored. The monochromator includes a plane grating and a moving mirror that operate under stepping control to obtain a sequence of beams of light in different narrow-wavelength bands at the excitation wavelengths of interest. The beam selected at any given instant enters the flowing water through a slit in the cell. Fluorescence emitted by the microbes in a direction perpendicular to the incident beam of light is band-pass filtered at a fluorescence wavelength of interest and measured by use of a photomultiplier. The cell contains a photodiode that measures the intensity of the illumination so that the fluorescence signals can be normalized.

Band-pass filters for the fluorescence wavelengths of interest are mounted on a wheel, which is rotated to place the filter for the desired fluorescence wavelength in front of the photomultiplier. The photomultiplier output is integrated over a series of flashes, then passed to an analog-to-digital converter. A microprocessor selects the monochromator and filter-wheel settings for the excitation and fluorescence wavelengths required in a given measurement, coordinates the operation of the flash lamp with acquisition of data, and communicates with the host computer.

The digitized fluorescence-signal data for all the wavelengths of interest are sent to the host computer for processing by the pattern-recognition algorithms. Of the algorithms tested thus far, one performs a rotated-principal-components regression analysis; it has been found to be suitable for determining total population densities and identifying genera, but does not do as well at identifying species. Another algorithm performs a genetic-neural-network analysis and has been found to perform well at the species level.

This work was done by Kenneth J. Schlager of Biotronics Technologies, Inc., for **Kennedy Space Center**. *Further information is contained in a TSP [see page 1].*

In accordance with Public Law 96-517, the contractor has elected to retain title to this invention. Inquiries concerning rights for its commercial use should be addressed to

Kenneth J. Schlager
Biotronics Technologies, Inc.
W226 N555B Eastmound Dr.
Waukesha, WI 53186

Refer to KSC-11755, volume and number of this NASA Tech Briefs *issue, and the page number.*

National Aeronautics and
Space Administration

NASA

74

END

04\23\99